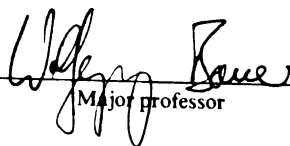




This is to certify that the
dissertation entitled
Equilibrium and Non-Equilibrium
Models for Particle Production
in Heavy-Ion Collisions

presented by
Catherine Marie Mader

has been accepted towards fulfillment
of the requirements for
PhD degree in Physics


Major professor

Date Aug 5, 1993

LIBRARY
Michigan State
University

PLACE IN RETURN BOX to remove this checkout from your record.
 TO AVOID FINES return on or before date due.

DATE DUE	DATE DUE	DATE DUE
_____	_____	_____
_____	_____	_____
_____	_____	_____
_____	_____	_____
_____	_____	_____
_____	_____	_____
_____	_____	_____

EQUILIBRIUM AND NON-EQUILIBRIUM MODELS FOR PARTICLE PRODUCTION IN HEAVY-ION COLLISIONS

By

Catherine Marie Mader

A DISSERTATION

Submitted to
Michigan State University
in partial fulfillment of the requirements
for the Degree of

DOCTOR OF PHILOSOPHY

Department of Physics and Astronomy

1993

ABSTRACT

EQUILIBRIUM AND NON-EQUILIBRIUM MODELS FOR PARTICLE PRODUCTION IN HEAVY-ION COLLISIONS

By

Catherine Marie Mader

In Part I, a non-equilibrium hadronic transport model which numerically solves the Boltzmann-Uehling-Uhlenbeck (BUU) equation, is introduced to probe the space-time evolution of the reaction zone formed in heavy-ion collisions. First, the emission of fragments from a compound nucleus formed during intermediate-energy heavy-ion collisions is explored. A hybrid formalism is introduced in which the transport model is used to study the initial ≈ 50 fm/c of ^{129}Xe -induced reactions at $E/A = 50$ MeV, and then a statistical evaporation model is used to evaluate the light particle and fragment emission from the hot reaction zone. While the model is only qualitative, comparison to data demonstrates the need to include dynamics when studying fragment production in intermediate-energy heavy-ion collisions.

Second, the two-proton correlation function is introduced. Using the proton phase-space predicted by BUU and the folding formalism of Koonin to combine it with the two-proton relative wave function, the size of the emitting source can be studied. Comparison to recent experimental results for $^{36}\text{Ar} + ^{48}\text{Sc}$ at $E/A = 80$ MeV characterizes the reaction zone as a function of impact parameter.

Third, the Koonin formalism is used again to calculate both the $\pi^+ - \pi^+$ and $\pi^+ - \pi^-$ correlation functions at relativistic energies. Both correlation functions are

studied for 1.6 GeV $p + C$ and 1.6 GeV $p + Pb$ reactions. The results for the heavy system are shown to be strongly affected by the absorption and rescattering of pions, while the lighter system is not dramatically affected by this nuclear shadowing.

In Part II, an equilibrium model, the Nuclear Firestreak model (NFS), is introduced, to explore strange particle production in heavy-ion collisions at highly relativistic energies. An increase in strange particle production has been proposed to be an indication of the formation of a quark-gluon plasma at these energies. The experimental observation of such an increase in strange particle production with an increase in the mass of the colliding system at ≈ 15 GeV/nucleon, is compared to predictions from the purely hadronic firestreak model, which assumes the interacting hadrons are in thermal and chemical equilibrium. This model is able to reproduce the experimental results, which indicates that increased strange particle production alone is not an unambiguous signal of a quark-gluon plasma.

To my husband, my best friend and my colleague.

Graham, you make my life complete.

ACKNOWLEDGMENTS

I would like to thank, not only the key players during my time at MSU, but those who have helped spark my interest in physics, as well.

Without a doubt, my advisor, Dr. Wolfgang Bauer has played a substantial role in my career at MSU. Wolfgang has guided me through several successful research projects over the last three years while letting me have a great deal of freedom along the way. In the process, I have learned a great deal of physics and self-reliance. By never demanding anything from me, I felt much more compelled to demand it of myself, and in the end, that is what will help me succeed in future endeavors. In addition, he encouraged me to be active in other activities. I know that many of my fellow graduate students envied the fact that I was encouraged to have a happy, well-balanced life of research, course-work, outreach projects, and a family life and I greatly appreciate the peace of mind this balance gave me over the years.

I'd like to thank my committee members for the time and effort they have put into reading my thesis, as well as attending my defense. Dr. Jules Kovacs was the first faculty member I met at MSU. He immediately proceeded to give me good advice and managed to make me feel less homesick by talking about Colorado and the mountains. Dr. Wayne Repko was a joy to work for as a teaching assistant. I enjoy his sense of humor and value his opinion on my future plans. When I think of Dr. Gary Westfall, "Don't worry, be happy!" immediately comes to mind. I'm extremely fortunate to have worked with him on the firestreak model calculations. Many thanks to Dr. Pawel Danielewicz and Dr. C. P. Yuan for stepping in at the last minute.

Scott Pratt added a breath of fresh sarcasm when he arrived at MSU. I'd like to thank him for all of the informative physics discussions we have had. I really appreciate the addition of another person who adds, not only to the wealth of physics

knowledge in the Nuclear Theory group at MSU, but also to the lighter side of life.

I must also acknowledge several professors from the Colorado School of Mines. Without the persistence of Ed Cecil, Jim McNeil, Bill Law and Art Sakakura, I would never have entered graduate school. During my time at CSM, these gentlemen challenged me at every turn. They knew that it was the challenge that drove me to work harder. Their advice and friendship is valued immensely.

Noone has had a greater impact on my desire to be a physicist than Rod Storr. His love for Physics rubbed off on the girl who thought science was boring. I learned that an instructor's enthusiasm and desire to teach sparks enthusiasm and desire to learn in a student, and hope that I can motivate my students as much as he did his.

Through the years, many friends have helped me to maintain some semblance of sanity. Life in Michigan would have been very lonely without Ninamarie Levinsky. Lilian Hoines, Erik Hendrickson, Rooster McConville, Gary Holmes and George Jeffers made a newcomer feel welcome, and make leaving MSU a little difficult.

Finally, I have to thank my parents, Michael and Juliana, my sisters, Margie and Terry, as well as the rest of my family in Denver. As a child, I continuously pointed at things and asked "What's that?", followed quickly by "But why?" My questions and curiosity were never discouraged. Although what I do for a living is a bit of a mystery, they are always supportive. They taught me that I could do anything I wanted, if I worked hard. They also taught me never to give up and to never be afraid to ask questions. Without their love and support, I would never have succeeded.

My husband, Graham has filled the void I never knew was present in my life. He shares my love of science and my love for solving mysteries. He is my sounding board and devil's advocate. I have always called Colorado home, but now, home is wherever Graham and I live. For everything he has given me, I dedicate this thesis to him.

Contents

LIST OF TABLES	ix
LIST OF FIGURES	x
1 Introduction	1
I Non-equilibrium Model of Heavy-Ion Collisions	7
2 Introduction	8
3 BUU-Hadronic Transport Model	11
3.1 The Model	11
3.2 Single Particle Observables	14
4 Fragment Production in Heavy Ion Collisions	18
4.1 Evaporation Model	19
4.2 EES-BUU Hybridization	23
4.3 Comparison with Experiment	32
5 Evolution of the Reaction Zone	37
5.1 Intensity Interferometry: HBT	37
5.2 The Correlation Function	41
5.3 Comparison with Experiment	47
6 Nuclear Shadowing	57
6.1 Pion Production	61
6.2 Calculation of the Correlation Function	65
6.3 Comparison with Experiment	67
7 Conclusions	76

II	Equilibrium Model of Heavy Ion Collisions	79
8	Introduction	80
9	The Model	84
9.1	Conserved Quantities in the Streaks	84
9.2	Restrictions of Chemical Equilibrium	88
9.3	Boundary Conditions	89
9.4	Particle Production in the Model	93
10	Comparison With Experiment	98
11	Conclusions	104
	LIST OF REFERENCES	106

List of Tables

3.1	Equation of state parameters used in BUU calculations.	14
4.1	Input parameters for EES model predicted by BUU calculations. . . .	35
8.1	Baryons and mesons used in the nuclear firestreak model.	83
9.1	Probability per nucleon in a streak for producing charged pions and kaons in central A+A ($\eta = 0.5$) collisions at 14.6 A GeV/c. The % yields for direct and decay production are also included.	96
10.1	K/ π ratios for central A on B collisions at 14.6 A GeV/c.	103

List of Figures

1.1	The solid lines represent isotherms for an equation of state for nuclear matter derived using Skyrme interactions. The dashed lines represent isotherms of a Van der Waals the equation of state. The temperatures (T), pressure (P) and volume (V) are given in multiples of the critical values.	3
3.1	Transverse energy spectra for 80 MeV/A $^{36}\text{Ar} + ^{45}\text{Sc}$ at $\langle\theta_{lab}\rangle = 38^\circ$. Solid symbols represent data [Lis]. Histograms represent results of BUU calculations, filtered for geometrical acceptance.	16
4.1	Mass, density and radial kinetic energy per particle of the residue in 50 MeV/A $^{129}\text{Xe} + ^{51}\text{V}$. The solid curves represent calculations done using the BUU code with a stiff equation of state. The dotdashed curves represent the soft equation of state results.	25
4.2	The mass, density and radial kinetic energy per particle of the residue in 50 MeV/A $^{129}\text{Xe} + ^{27}\text{Al}$, ^{51}V , ^{89}Y and ^{197}Au , predicted by the BUU code using a stiff EoS.	27
4.3	The mass, density and radial kinetic energy per particle of the residue in 50 MeV/A $^{129}\text{Xe} + ^{27}\text{Al}$, ^{51}V , ^{89}Y and ^{197}Au , predicted by the BUU code using a stiff EoS.	28
4.4	Density profile of residual nucleus from the BUU calculation for a stiff EoS for 50 MeV/A $^{129}\text{Xe} + ^{27}\text{Al}$	30
4.5	Density profile of residual nucleus from the BUU calculation for a soft EoS for 50 MeV/A $^{129}\text{Xe} + ^{89}\text{Y}$	31
4.6	Binding energy and density profile of residual nucleus in the BUU calculation for a soft EoS for 50 MeV/A $^{129}\text{Xe} + ^{27}\text{Al}$, ^{197}Au . The calculations were done with a soft equation of state.	33
4.7	Charged particle multiplicities vs. mean number of IMFs for 50 MeV/A $^{129}\text{Xe} + ^{27}\text{Al}$, ^{51}V , ^{89}Y and ^{197}Au . The points represent the data. The boxed regions represent model predictions for various radius cuts and compressibilities. In each plot, the right set of boxes are unfiltered results and the left set are filtered with experimental efficiency cuts [Bow92].	36

5.1	The relative wave function, $ \phi(q, r, \cos(\theta)) ^2$, for fixed angle $\theta = 60^\circ$ as a function of relative position and momentum [Bau92a].	42
5.2	Source size comparisons	43
5.3	Correlation functions calculated for 75 MeV/A $^{14}\text{N} + ^{27}\text{Al}$ at $\langle\theta_{lab}\rangle = 25^\circ$ for $P = 500$ MeV/c. The different lines represent BUU predictions using different values of σ_{nn} and nuclear EoS [Gon91].	46
5.4	Correlation functions for 75 MeV/A $^{14}\text{N} + ^{27}\text{Al}$ at $\langle\theta_{lab}\rangle = 25^\circ$. Data are given by solid symbols. BUU calculation results are given by the curves [Gon91].	48
5.5	Proton emission points in the reaction plane for 80 MeV/A $^{36}\text{Ar} + ^{45}\text{Sc}$ at $b = 2.5$ fm. The 12 panels show the emission points of protons emitted in 10 fm/c time steps. The upper left panel shows emission points of protons emitted during the earliest time step ($t < 30$ fm/c) while the lower left panel shows the emission points of protons emitted during the latest time step ($130 \text{ fm/c} < t$).	49
5.6	Proton emission points in the reaction plane for 80 MeV/A $^{36}\text{Ar} + ^{45}\text{Sc}$ at $b = 6$ fm. The 12 panels show the emission points of protons emitted in 10 fm/c time steps. The upper left panel shows emission points of protons emitted during the earliest time step ($t < 30$ fm/c) while the lower left panel shows the emission points of protons emitted during the latest time step ($130 \text{ fm/c} < t$).	50
5.7	Correlation functions calculated for 80 MeV/A $^{36}\text{Ar} + ^{45}\text{Sc}$ at $\langle\theta_{lab}\rangle = 38^\circ$. The solid points represent the experimentally measured correlation functions while the histograms represent correlation functions predicted by BUU [Lis93].	53
5.8	Average peak height of the two-proton correlation function as a function of total momentum for 80 MeV/A $^{36}\text{Ar} + ^{45}\text{Sc}$ at $\langle\theta_{lab}\rangle = 38^\circ$. The scale on the right axis is the Gaussian source radius. The solid points represent the experimental correlation functions, open points represent the predictions of BUU [Lis93].	54
6.1	Schematic diagram of the nuclear potential with the possible mediating mesons shown in their region of dominance [Mac86].	58
6.2	Superposition of pion and delta-resonance trajectories (thin-dots and thick-dots respectively) projected onto the reaction plane for 50 1.6 GeV p + Pb events at $b = 5$ fm.	62
6.3	Average number of charged pions per event for 1.6 GeV p + C & Pb collisions. The diamonds represent positive pions, the circles, negative pions and the line represents the total number of charged pions. . . .	64
6.4	Pion kinetic energy spectra for pions emitted in 1.6 GeV p + Pb collisions with impact parameter $b=5$ fm predicted using the transport model. The solid line represents pions produced in single pion events, the symbols represent pions produced in multi-pion events (diamonds for pions emitted first and circles for second).	66

6.5	Two pion correlation function for 1.6 GeV p + C and Pb as a function of the invariant-mass of the $\pi^+\pi^-$ pair. The squares represent the experimental data [Plu92] and the histograms represent the BUU transport model calculations.	68
6.6	Two pion correlation function for 1.6 GeV p + C (left) and Pb (right) as a function of the invariant-mass of the $\pi^+\pi^-$ pair for specific impact parameters. The top row contains results for the most central cases while the bottom row contains results the most peripheral. The solid histograms represent the predictions of the BUU model while the dashed histograms represent the predictions of the BUU model after applying a filter to simulate the geometric and kinematic acceptance of the DIOGENE detector.	70
6.7	The two-pion relative wave function, $ \phi(q, r, \cos(\theta)) ^2$, for fixed angle $\theta = 60^\circ$ as a function of relative position and momentum [Bau93]. . .	72
6.8	The $\pi^+\pi^+$ correlation functions for 1.6 GeV p + C (left), and 1.6 GeV p + Pb (right). The symbols represent the calculations using the Koonin formalism with phase space predictions of BUU. The lines represent fits using Gaussian source parameterizations with radius parameters 1.5 fm (solid) and 0.5 fm (dashed).	73
9.1	Schematic drawing of a collision in the firestreak model in the center of mass frame. The top shows the orientation of nucleus A approaching nucleus B. The bottom figure shows the streaks in the reaction zone as well as the remnants of the original nuclei.	85
9.2	Chemical potential for K^+ in MeV for central A + A collisions at 14.6 A GeV/c. The crosses represent the values calculated using the NFS model. The dotted line is the value obtained by the program when complete stopping is assumed.	97
10.1	Invariant cross sections of p, π^\pm and K^\pm from 14.6 A GeV Si+Au collisions for $1.2 \leq y \leq 1.4$. The data are taken from reference [Mos91]. The lines represent the results of the calculations with the modified firestreak model for p(dashed), π (solid) and K(dot-dashed).	99
10.2	Invariant cross section of p, π^\pm and K^\pm from 14.6 A GeV Si+Al collisions for $y = 1.5$. The data are taken from reference [Cos90]. The lines represent the results of the calculations with the modified firestreak model for p(dashed), π (solid) and K(dot-dashed).	100
10.3	Rapidity distributions per projectile nucleon (28) for π^\pm and K^\pm produced in central 14.6 A GeV Si+Au collisions. The data are taken from reference [Mia90]. The lines represent the results of the calculations with the modified firestreak model for π (solid) and K(dashed).	102

Chapter 1

Introduction

Matter is often described using an equation of state (EoS). A familiar example is the ideal gas equation of state, often displayed as isotherms on a P-V (Pressure-Volume) diagram. Such phase diagrams are important because, by knowing the EoS, predictions can be made about how a system will behave under different conditions.

In the case of an ideal non-interacting gas, the EoS can be derived from thermodynamic principles. The ideal system is, of course, not necessarily realistic. Better understanding of the molecular forces led to a more realistic EoS called the Van der Waals equation:

$$P = \frac{nkT}{V - nb} - \frac{an^2}{V^2}. \quad (1.1)$$

This equation relates the pressure (P) of a system of n molecules to its volume (V), and its temperature (T) (k is the Boltzmann constant). By experimentally varying the pressure, volume or temperature, one can determine the parameters a and b , which are related to the strength of the Van der Waals forces and finite size effects. For example, an experimentalist can measure the change in the pressure of a container of gas while changing the temperature of the container. Measurements of macroscopic systems where one state variable is kept fixed, while another varies, have allowed not only the constants a and b to be determined, but the regions of validity of the Van

der Waals EoS to be understood as well.

Because of the similarities between the general behavior of the nuclear force and the Van der Waals force, analogies are often drawn between the well-known behavior of Van der Waals gases and nuclear matter. Both forces exhibit a strong short-range repulsive force and an intermediate-range attractive force. Thus, similar equations of state relating pressure, volume and temperature have been derived for nuclear matter. Figure 1.1 shows one equation of state for nuclear matter which was derived using Skyrme type interactions [Jaq83]. Also shown on the plot is the equation of state for a Van der Waals gas, where equation 1.1 has been rewritten in a dimensionless form. The two equations of state do, in fact, agree qualitatively.

However, there is a significant difference between them. The EoS of molecular gasses can be studied through direct measurements of macroscopic systems. These experimental results can be compared directly to models, such as the Van der Waals EoS which are derived assuming that the system is large (if it is studied at room temperature and pressure, the system contains $\approx 10^{23}$ molecules). However, a similar direct measurement of nuclear state variables is not possible. There is no way to access a system containing 10^{23} nucleons to perform experiments to determine thermodynamic properties of nuclear matter.

Nature does provide one system of the appropriate size. Neutron stars are expected to have densities ranging from $10^7 - 10^{15} \text{ g/cm}^3$. Cold nuclear matter has a density of $\approx 10^{14} \text{ g/cm}^3$ or $0.168 \text{ nucleons/fm}^3$ ($\approx 10^{39} \text{ nucleons/liter}$). So, while natural macroscopic systems do exist, measurement of the temperature, volume and pressure of these systems with any reasonable degree of accuracy is not possible. However, if the nuclear EoS was well-known, it could be used in various models of stellar evolution to better understand the natural nuclear processes occurring in astrophysical systems.

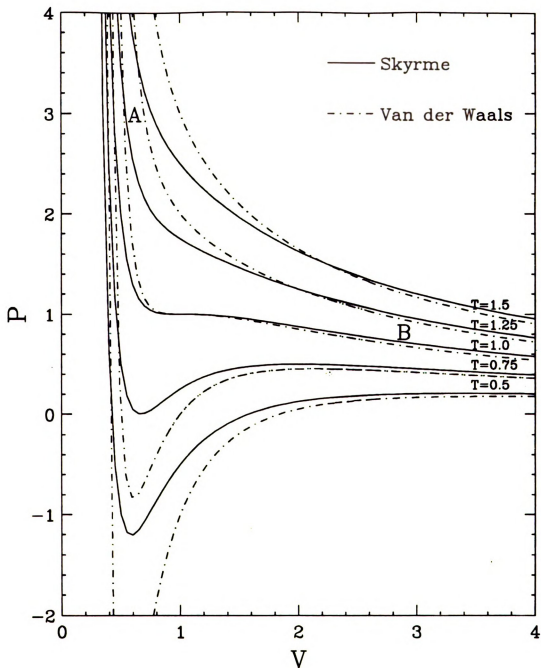


Figure 1.1: The solid lines represent isotherms for an equation of state for nuclear matter derived using Skyrme interactions. The dashed lines represent isotherms of a Van der Waals the equation of state. The temperatures (T), pressure (P) and volume (V) are given in multiples of the critical values.

One way to observe the effects of varying the nuclear EoS state variables is via heavy-ion reactions. During the initial stages of a central heavy-ion collision, the two nuclei can compress. As the collision progresses, the interaction region will then expand and cool. In fact, during the various stages of the collision, the state variables for nuclear matter (pressure, volume, and temperature) will vary, just as for the macroscopic Van der Waals system. However, it is still impossible to make direct measurements of these variables. For this reason, model calculations which include information about the nuclear EoS are introduced. Within each model, predictions about the evolution of the nuclear reaction zone can be obtained for a particular nuclear EoS. Then, the calculated results for various observable quantities can be compared to experimental measurements to try to gain insight into the nuclear EoS, and to quantitatively describe the behavior of nuclear matter.

However, there are many complications in comparing the results deduced from nuclear collision observables with the results observed for macroscopically measurable systems. First and foremost is the finite size of the system. In Van der Waals gas studies, both experimental and theoretical assumptions of infinite size are valid. However, in nuclear experiments, we are limited to particle numbers smaller than ≈ 500 and length scales less than ≈ 100 fm. So, while some information about nuclear interactions in finite systems is available, direct comparisons to infinite nuclear systems are difficult to make.

In addition, heavy-ion collisions are practically never head on collisions. They always occur at a finite impact parameter (which is defined as the projection of the separation of the centers of the nuclei on the beam axis). Since there is no way to measure this distance exactly in a single collision, care must be taken when comparing to theoretical results, since all that is measured is an average property over many possible collisions. Often, some centrality selection can be used to limit the range of

impact parameters observed, but there is always some uncertainty involved.

Also, the orientation of the reaction plane can not be directly measured. The reaction plane is the plane containing the beam axis and the impact parameter vector. Typically, what is measured is the result of heavy-ion collisions where the reaction plane is randomly oriented over 2π possible angles. All of these finite-size effects (both particle number and geometrical) affect the measured quantities, and must be taken into consideration when comparing theoretical results with data.

In the following chapters, two models of heavy-ion collisions will be described. In Part I, the hadronic transport model, BUU will be introduced. This non-equilibrium transport model will be used to study heavy-ion collisions at beam energies from 35 MeV/nucleon to ≈ 1 GeV/nucleon. Several comparisons to experimental observations will be made in order to better understand the evolution of the reaction zone formed in heavy-ion collisions, and to obtain information on the nuclear equation of state.

The second model concerns more exotic regimes of nuclear systems. As experimental technology has improved, nuclear matter can be forced to higher and higher densities, and the theoretical study of the nuclear equation of state at these high densities becomes important. In astrophysical systems, these densities may occur at the centers of neutron stars. However, as beam energies begin to exceed several GeV/nucleon, the equation of state studied in Part I becomes invalid. At the particle and energy densities attained in these collisions, the forces being studied are no longer just the conventional nuclear forces due to meson exchanges.

The fundamental degrees of freedom which need to be considered are those of free quarks and gluons, which may no longer be confined to the color singlet states of nucleons and other hadrons. At sufficiently high densities during a relativistic

heavy-ion collision, a plasma of quarks and gluons may briefly exist. Experimental signatures for a conversion of nuclear matter into a quark-gluon plasma (qgp) have been predicted by theoretical studies, and are currently being sought experimentally. An interesting question arises as to whether these signatures are unique to a nuclear phase transition, such as a qgp. In Part II, a hadronic thermal model is developed which assumes that chemical and thermal equilibrium is attained in the reaction zone. Within the purely hadronic scenario, the production of strange particles for various systems is studied. Strangeness enhancement was proposed as one possible qgp signal [Raf82]. However, it will be shown that the experimental evidence on strangeness enhancement collected at the AGS thus far can still be explained by this hadronic model. Therefore the experimental observations are not a unique signal that a qgp has been created.

Part I

Non-equilibrium Model of Heavy-Ion Collisions

Chapter 2

Introduction

Intermediate-energy heavy-ion reactions (beam energies of 30 - 300 MeV/nucleon) are frequently described as a two-stage process: a compressional phase during which the nuclear matter is heated, followed by an expansion phase during which the nuclear matter cools. On the phase diagram in Figure 1.1, assuming a dense, hot ball of nuclear matter was formed at a given temperature, volume and pressure, the reaction begins at the point labelled A. If the nuclear matter then undergoes an isothermal expansion to point B, the pressure decreases. In fact, at low temperatures, $T < 1$, the pressure becomes negative due to the attractive part of the nuclear force. If the expansion energy is not large enough to overcome this attractive force, the system can hold together and cool by radiating photons, particles and fragments. On the other hand, if the temperature of the nuclear matter is high, $T > 1$, the system will not reach negative pressure, and the system will continue to expand after the initial collision.

While isothermal expansion is useful only as an illustrative example, it does show the challenge faced in modelling heavy-ion collisions. At the extremes of the energy scale (at either very low or high temperatures), different models successfully describe either the formation of a compound nucleus that evaporates light particles, or the complete “explosion” of the system into light particles. For the region in-

between, more complicated studies are necessary. How does the reaction proceed in the intermediate-energy region?

A powerful tool for studying this dynamic evolution of the reaction zone is the hadronic transport model, BUU, a semi-classical model which describes the evolution of a nucleus-nucleus collision at a microscopic level [Bau86, Ber84, Ber88, Dan91, Kru85, Li91a, Li91b, Wan91]. The motion of the constituent nucleons is determined by solving the Boltzmann-Uehling-Uhlenbeck equation. In this way, the nucleons in the heavy-ion reaction are studied from the earliest stages of the collision (before the nuclei even begin to interact) until the collision has ended. In this way, the transient nature of the system created in the heavy-ion reaction can be modelled, and various assumptions about the nuclear EoS can be tested. The model will be described in detail in the following chapter.

In order to verify that the assumptions in the model are valid, the calculated results are compared to several experimental observations. In this way, the parameters of the equation of state as well as other model parameters can be determined. These comparisons will be presented in chapters 4 - 6 of part I.

Specifically, the cooling and expanding phase of the reaction will be explored in chapter 4. During the expansion phase, nuclear matter can emit particles. These particles may be photons, neutrons, protons, deuterons, tritons, alphas or even heavier fragments. Within the BUU formalism, only the emission of single particles (e.g. photons, protons and neutrons) can be studied. In order to study the emission of heavier fragments, a hybrid model is developed in which the early stages of the collision are simulated using the BUU model. Then, as the system expands and cools, a statistical decay model (Expanding Emitting Source) is introduced to study the production of heavier fragments. While this is an inexact method for studying fragment formation, the comparison of the predicted observables with the data does provide insight into

the evolution of the reaction zone.

In chapter 5, the evolution of the reaction zone will be studied further via experimental particle-particle correlation measurements, which directly probe the size of the reaction zone as a function of time. In this instance, proton-proton correlations are measured and direct quantitative comparisons with the single-particle predictions of the BUU model are possible. This comparison shows that the model provides valuable information on the evolution of the reaction zone formed in heavy-ion collisions. In addition, by adjusting parameters in the code, quantitative information about the nuclear EoS and the effect of the nuclear medium on nucleon-nucleon collisions is obtained.

The effects of the finite size of the reacting system in heavy-ion collisions can also be studied in the framework of the BUU transport model. In chapter 6, collisions of relativistic protons with both heavy and light targets will be studied. The measured pion correlation results from the light and heavy targets are dramatically different. Comparison to the predictions of the BUU transport model show that, at least for the systems studied, intriguing aspects of the experimental data can be explained by finite-size geometric effects. Simple, but careful consideration of the geometric orientation of the colliding system, which cannot be determined precisely in the experimental observations, can account for the unusual experimental data. Thus, these data are shown not to require the inclusion of any exotic nuclear matter phenomena, which had been suggested.

Chapter 3

BUU-Hadronic Transport Model

3.1 The Model

The BUU model is a microscopic approach to studying heavy-ion collisions. Formally, it is a numerical solution of the Boltzmann-Uehling-Uhlenbeck equation [Nor28, Ueh33]:

$$\begin{aligned} \frac{\partial f(\vec{r}, \vec{p}, t)}{\partial t} + \vec{v} \cdot \nabla_{\vec{r}} f(\vec{r}, \vec{p}, t) - \vec{\nabla}_{\vec{r}} U(\rho(\vec{r})) \cdot \vec{\nabla}_{\vec{p}} f(\vec{r}, \vec{p}, t) = \\ \frac{4}{(2\pi)^3} \int d^3 k_2 d^3 k_3 d\Omega v_{12} \frac{d\sigma}{d\Omega} \delta^3(\vec{p} + \vec{k}_2 - \vec{k}_3 - \vec{k}_4) \\ \times [f_1 f_2 (1 - f_3)(1 - f_4) - f_3 f_4 (1 - f_1)(1 - f_2)]. \end{aligned} \quad (3.1)$$

The nucleons are represented by a distribution function $f(\vec{r}, \vec{p}, t)$. The left-hand side of equation 3.1, when equal to 0, reduces to the Vlasov equation [Vla38, Vla45]. This represents the time evolution of the distribution function under the influence of the mean field, $U(\rho(\vec{r}))$, due to the nuclear (and Coulomb) interactions. The right-hand side of equation 3.1 determines the effects of the individual hadron-hadron collisions where Pauli-blocking of the final states of nucleon-nucleon collisions is taken into account through the $f_i(1 - f_j)$ terms.

In practice, equation 3.1 is solved numerically using the test-particle method [Won82]. The nucleons are represented as an ensemble of point particles which are

initially uniformly distributed in a sphere representing the nucleus. The number of test particles used to represent each nucleon is usually greater than 100 to reduce the fluctuations due to numerical uncertainties. If the collision is non-central, then the centers of the nuclei are offset by the impact parameter. The particles are randomly assigned momenta so that they are uniformly distributed in a Fermi-sphere. The projectile is then assigned an additional boost, equal to the beam velocity, toward the target. Both projectile and target nucleons are bound by a mean field determined by the distribution of all test particles. This mean field contains the information of the nuclear equation of state. Once the nuclei begin to overlap, nucleon-nucleon collisions begin to occur among nucleons the individual ensembles. The frequency of these collisions is governed by the nucleon-nucleon cross section (σ_{nn}) and by the possible blocking of final states due to the Pauli exclusion principle. In the case of high-energy collisions, particle and resonance production is possible. This, too is governed by the appropriate reaction cross sections.

In particular, the single-particle phase space $f(\vec{r}, \vec{p})$ is written as:

$$f(\vec{r}, \vec{p}) = \sum_i \delta(\vec{r} - \vec{r}_i) \delta(\vec{p} - \vec{p}_i). \quad (3.2)$$

Substituting this into the Vlasov equation allows the equations of motion for the test particles to be written as:

$$\frac{d}{dt} \vec{p}_i = -\vec{\nabla}_r U_{nuc}(\rho(\vec{r}_i)) + \frac{1}{N} \sum_{j \neq i} \frac{q_i q_j}{|\vec{r}_i - \vec{r}_j|^3} (\vec{r}_i - \vec{r}_j), \quad (3.3)$$

$$\frac{d}{dt} \vec{r}_i = \frac{\vec{p}_i}{E_i} = \frac{\vec{p}_i}{\sqrt{m_i^2 + p_i^2}}, \quad (3.4)$$

$$i = 1, \dots, (A_t + A_p)N + N_\pi, \quad (3.5)$$

where A_i is the number of nucleons in the target or projectile, N is the number of parallel ensembles (or test runs), and N_π is the number of pions which are present in

the system. If the particle is not a nucleon, it will not feel the nuclear potential and thus U_{nuc} used in equation 3.3 will equal zero. However, for nucleons, a Skyrme-type interaction is used to represent the nuclear mean field [Sky59, Zam73]:

$$U_{\text{nuc}}(\rho(\vec{r})) = A \left(\frac{\rho(\vec{r})}{\rho_0} \right) + B \left(\frac{\rho(\vec{r})}{\rho_0} \right)^\sigma, \quad (3.6)$$

where A , B and σ are input parameters which describe the nuclear equation of state.

As discussed earlier, the nuclear force has attractive and repulsive components. In equation 3.6, the coefficient A determines the magnitude of the attractive part while the coefficient B determines the repulsive part. After choosing a compressibility, K , which is related to the three parameters through:

$$K = 9 \left(\frac{p_F^2}{3m} + A + \sigma B \right), \quad (3.7)$$

A , B and σ are determined from nuclear saturation properties. The two parameterizations used throughout this work are referred to as the “soft” and “stiff” equations of state. They are frequently compared to the soft and stiff spring constants in harmonic-oscillator type problems. The values of the parameters and their corresponding compressibilities are given in Table 3.1 [Ber89]. In addition, a parameterization for a “medium” EoS is also given [Bau86].

The right-hand side of equation 3.1 is the collision integral. It determines the effects of both elastic and inelastic scattering of the test particles. In the case of nucleon-nucleon collisions, $\frac{d\sigma}{d\Omega}$ is the energy-dependent, experimentally measured nucleon-nucleon cross-section. Initially, there are no resonances or pions present in the system. Resonance production proceeds via the following mechanisms:

$$N + N \leftrightarrow N + N, \quad (3.8)$$

$$N + N \leftrightarrow N + \Delta,$$

$$N + N \leftrightarrow N + N^*.$$

Table 3.1: Equation of state parameters used in BUU calculations.

EoS	K (MeV)	A (MeV)	B (MeV)	σ
Stiff	380	-124	70.5	2
Medium	235	-218	164	$\frac{4}{3}$
Soft	200	-356	303	$\frac{7}{6}$

Where possible, experimentally measured cross sections are used. Detailed balance is used to determine all other cross sections [Dan91, Li93]. In addition, pion production and absorption is possible. This occurs via resonance decay and pion recapture, the mechanisms for which are:

$$\Delta \leftrightarrow \pi + N \quad (3.9)$$

$$N^* \leftrightarrow \pi + N.$$

3.2 Single Particle Observables

BUU calculations have successfully predicted single particle spectra, such as gamma, proton and pion spectra [Aic85, Bau86, Bau87, Li91a]. In most cases, the spectra have been inclusive. New detection devices that have angular coverage of almost 4π have recently been developed. Thus, in some events, they are able to detect more than 80% of the charge of the initial system. One of the benefits of having 4π detector coverage is that the events can now be classified as central or peripheral based on the multiplicity of observed particles, the measured transverse energy or the mid-rapidity charge of the event.

Central collisions are more violent. The complete overlap of the projectile and target allows most of the beam energy to be shared among the nucleons of both heavy ions. In addition, the compressional energy from the initial compressed stage of the collision converts to kinetic energy away from the reaction zone, and leads to a large number of detected particles with a large amount of energy perpendicular to the beam direction. This transverse kinetic energy is given by:

$$E_t = \frac{p_x^2 + p_y^2}{2m} = \frac{p^2 \sin^2(\theta)}{2m}, \quad (3.10)$$

where θ is the angle between the particle's momentum and the beam axis (z-axis) and non-relativistic kinematics are assumed. In peripheral collisions, the amount of overlap between the target and projectile nuclei is significantly less. This leads to less energy transferred to the target nucleons by the projectile, and less compression. Thus, the central events will have not only more detected particles, but more transverse kinetic energy than peripheral events.

The ability to select event classes with centrality allows for more detailed comparisons between BUU and experiment. Figure 3.1 shows both the experimentally measured and calculated proton transverse energy (E_t) spectra from 80 MeV/A $^{36}\text{Ar} + ^{45}\text{Sc}$ collisions, where the results of the numerical calculations have been passed through a detector filter[Lis]. In these calculations, a stiff EoS has been used. For central events, the BUU results are in good agreement with the data. As expected, the kinetic energy spectrum of the central events does extend out to higher energies than the peripheral events. For the peripheral events the BUU results slightly underpredict the low E_t portion of the spectra. Since the spectra are nearly linear on the semi-log plot, a fit with an exponential in kinetic energy can be made:

$$\frac{dN}{dE_t} \approx N_0 \exp\left(\frac{-E_t}{A}\right). \quad (3.11)$$

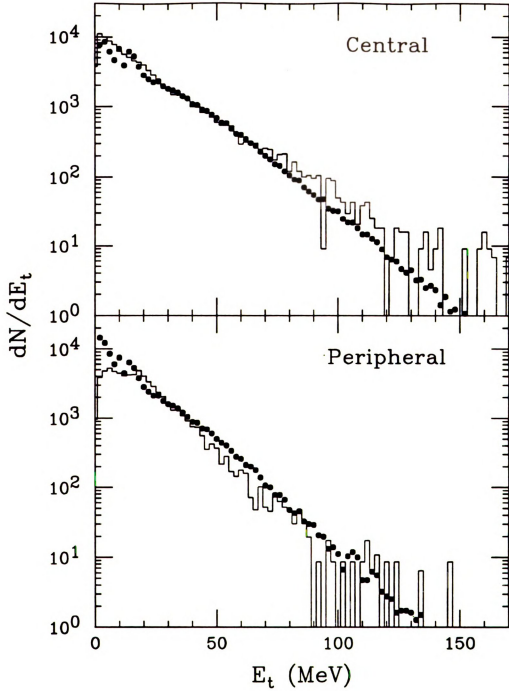


Figure 3.1: Transverse energy spectra for 80 MeV/A $^{36}\text{Ar} + ^{45}\text{Sc}$ at $\langle\theta_{lab}\rangle = 38^\circ$. Solid symbols represent data [Lis]. Histograms represent results of BUU calculations, filtered for geometrical acceptance.

The slope parameter (A) for the experimentally observed central events is ≈ 16.5 MeV, while the slope of the calculated spectrum is ≈ 17.9 MeV. For the peripheral events, the experimental and theoretical slope parameters are more similar, ≈ 13.9 MeV and ≈ 13.5 MeV respectively. In the peripheral case, however, the calculated spectrum at low transverse energy falls far below the straight line fit assumed for extracting the slope parameters. If one were to equate this slope parameter to a temperature of the emitting source, these spectra would imply that the protons emitted in the central events are coming from a hotter source than the protons emitted in the peripheral events.

The differences in the slope parameter for the calculated and measured spectra could be due to several factors. First, the experimental centrality selection is not exact. Thus, the selection of impact parameters to include in the comparison with theory is also inexact. In addition, the equation of state chosen in this comparison was a stiff equation of state. A medium or soft equation of state would produce slightly less transverse momentum, thus reducing the central slope slightly and possibly filling in the low-energy part of the peripheral spectrum.

Adjusting these two assumptions to provide better agreement is possible, but not reasonable. One limitation of BUU is that it is a semi-classical, single-particle model. Thus, fragment production cannot be directly studied. Previous studies have shown discrepancies between the predicted proton spectra of BUU and experimental measurement, which are most likely due to the inclusion of protons which should be bound in fragments in the BUU predictions. However, the purpose of this work is not to study the single particle observables predicted by BUU, but to build on the previous successes of BUU and to provide a better picture of the evolution of the reaction zone formed in heavy-ion collisions.

Chapter 4

Fragment Production in Heavy Ion Collisions

As experiments have increased in sophistication, theoretical models have improved in order to provide useful information about the new aspects of reaction dynamics being experimentally probed. For example, new detection devices are able to detect charged fragments emitted in heavy-ion collisions with energies as low as a few MeV in virtually any direction. One recent result from of a 4π detection system was the observation of a large number of intermediate-mass fragments (IMFs) in heavy-ion collisions of 50 MeV/A $^{129}\text{Xe} + \text{Au}$ [Bow91], where IMFs are defined as all particles with charge greater than 2. In fact, as many as 14 IMFs were detected in a single central event. Comparisons with several models showed that most models significantly underpredicted the observed results. However, the expanding emitting source (EES) model [Fri90] was able to reproduce the experimental results [Bow91]. In this statistical model, the hot compound nucleus formed during the collision is allowed to expand while emitting fragments and particles from its surface.

However, this model (and all statistical decay models) requires information about the initial conditions of the compound nucleus. These conditions are determined by the early stage of the collision prior to the formation of the compound nucleus. The

model requires 5 input parameters: mass (A), charge (Z), temperature (T), radial expansion energy (E_r), and compressibility (K_{EES}). In the comparisons of reference [Bow91], these values were varied in order to obtain reasonable agreement with the data.

Are the chosen values reasonable?

In order to address this question, the BUU model described in chapter 3 is used to characterize the initial stages of the collision. Although this is a single particle model and IMF production cannot be directly predicted by BUU, the input parameters of the EES model can be determined from the BUU results. This is a “hybrid” model approach. Several assumptions must be made when using this hybrid approach in which a microscopic model is combined with an evaporation model. In sections 4.1 and 4.2, both the EES model and the assumptions needed to perform the calculations are described. Of course, the final goal is to compare the results with data to see if this hybrid model is, in fact, a reasonable one. This comparison will be done in section 4.3.

4.1 Evaporation Model

There are several statistical models of the decay process. The principle assumption of these models is that the mechanism by which the hot drop of nuclear matter, a compound nucleus, was formed is unimportant. All that is necessary is that by the end of the initial phase of the collision a compound nucleus is present [Boh36]. Once this hot system is formed, it can decay via two modes: fission and evaporation. In 1937, Weisskopf developed an evaporation model which described the statistical decay of a compound nucleus [Wei37]. In this model, the compound nucleus cooled by evaporating smaller droplets of nuclear matter. Only the information which affected

the decay modes (such as size, energy, rotational energy, and parity) were important, how the system reached this state was not. It should be pointed out that this formalism was developed for light-ion reactions where the total energy of the compound nucleus was less than 50 MeV.

The method proposed by Weisskopf predicts the emission of light particles (p , n , and α) by assuming the hot compound nucleus cools by sequentially emitting particles until it no longer has enough energy to continue. This principle is the basis of many models and can be expanded to include IMF production [Bon82, Bon85, Cha88, Fai82, Fai83, Fri83, Lop84, Mek77, Mek78, Mor75, Ran81, Rop82a, Rop82b]. The probability for emitting a particle or fragment is determined from the principle of detailed balance.

This concept of statistical emission from a single hot source is used in many models. Its success at predicting light particle emission has been demonstrated [Dau68, Flu69, Ree69]. With the inclusion of IMF emission, some models have had great success with heavy-ion reactions for beam energies below 20 MeV/nucleon [Cha88, Fri83, Fri83a]. However, when applied to collisions at 50 MeV/nucleon, these models fail to produce enough fragments when compared to data. At these energies, the assumption that a single, well-defined compound nucleus is formed is no longer valid. In central collisions, the beam energy is high enough that initially, the central overlap region is compressed. The energy deposited by the projectile in the reaction zone is comparable to the binding-energy, and thus the expansion of the residual nucleus is significant. A model that takes into account the dynamical expansion of the hot reaction zone is necessary.

The expanding-evaporating source (EES) model is, as implied by the name, a model in which the hot reaction zone evaporates particles while it is allowed to expand. The evaporation process is calculated in the standard Weisskopf formalism.

The expansion is assumed to be an isotropic radial expansion of a uniform distribution of nucleons. Thus, in addition to the size (A_{res}) and thermal energy (E^*) needed in standard evaporation models, these residual nucleons are described by a collective radial expansion energy (E_r) and a collective compressional energy (E_c). Since the phenomenon being studied occurs in central events, the rotational energy of the compound nucleus is neglected in the evaporation process.

The total energy of the system is conserved, thus:

$$\frac{\partial E_{total}}{\partial t} = 0 = \frac{\partial E_c}{\partial t} + \frac{\partial E_r}{\partial t} + \frac{\partial E^*}{\partial t} + \frac{\partial E_{kin}^{emit}}{\partial t} + \frac{\partial E_{sep}}{\partial t}, \quad (4.1)$$

where E_{sep} is the separation energy of the fragments emitted, and E_{kin}^{emit} is the kinetic energy of the emitted particles. The separation energy of the nucleus is determined by total energy conservation. In a case where parent nucleus (P) decays to daughter nucleus (D) and fragment (f), total energy conservation requires:

$$M_P(\rho(t)) + E_P^* = M_D(\rho(t)) + E_D^* + M_f + E_f^{kin}, \quad (4.2)$$

where $M_i(\rho)$ is the mass of a given nucleus with density ρ , and M_i is the mass of the ground state nucleus. E_i^* is the excitation energy of nucleus i , and E_i^{kin} is the kinetic energy of the emitted particle. In this model, the recoil energy of the daughter nucleus is neglected. The emitted fragment is assumed to be at normal nuclear matter density, thus its mass is simply the measured mass. The parent and daughter nuclei, however, are not at normal nuclear matter density. The model then assumes that the total mass difference between the initial and final state is just the mass for nuclei at normal nuclear matter density plus the collective compressional energy released by creating the fragment:

$$M_P(\rho(t)) - M_D(\rho(t)) = M_P(\rho_0) - M_D(\rho_0) + E_c(A_f, \rho(t)). \quad (4.3)$$

The separation energy is then:

$$E_{sep} = E_D^* - E_P^* = -E_{kin}^f + M_P(\rho_o) - M_D(\rho_o) - M_f + E_c(A_f, \rho(t)). \quad (4.4)$$

The compressional energy is, in effect, the energy due to the nuclear forces. In the EES model, it is expressed as:

$$E_c(\rho(t), A(t)) = A(t) \frac{K_{EES}}{18} \left(1 - \frac{\rho(t)}{\rho_o} \right)^2 (MeV). \quad (4.5)$$

The constant K_{EES} is a compressibility constant. It is labelled with the subscript EES in order to distinguish it from the the compressibility of infinite nuclear matter as discussed in regard to the BUU model. K_{EES} represents the compressibility of finite nuclei, and is an input parameter of the EES model.

Finally, the radial expansion energy is:

$$E_r(\rho(t), A(t)) = \frac{1}{2} m \dot{R}_{rms}^2 = \frac{1}{18} m R_{rms}^2 \left(\frac{\dot{A}(t)}{A(t)} - \frac{\dot{\rho}(t)}{\rho(t)} \right)^2, \quad (4.6)$$

where the density is given by:

$$\rho(t) = \frac{A(t)}{\frac{4}{3} \pi R^3}. \quad (4.7)$$

Now that all energies have been expressed in terms of ρ and A , equation 4.1 can be expressed in terms of $\rho, \dot{\rho}, A, \dot{A}$ and the compressibility K_{EES} . Given the initial conditions of the system, the residue is allowed to evaporate particles as it expands isotropically under the constraint of total energy conservation. This model is, of course, a gross oversimplification of the nuclear fragmentation process, in particular in the presence of true multifragmentation. However, some limited insight into the influence of collective expansion on nuclear fragmentation can be obtained with its aid.

4.2 EES-BUU Hybridization

The initial conditions of the residue are inputs to the statistical model, EES. So while it may be useful to describe the fragment-production stage of the reaction, EES contains no information about the initial conditions. On the other hand, the BUU transport model contains information about the single-particle aspects of the collision and can be used to model the first few hundred fm/c of the collision during which the hot residual nucleus is formed. Due to its single-particle formalism, the BUU model is unable to predict IMF production, however, the BUU transport model can be used to simulate the initial stages of the collision and to determine the input parameters for the EES model.

In particular, the necessary quantities are:

$$A_{res} = \frac{1}{N} \sum_i 1 \quad (4.8)$$

$$Z_{res} = \frac{1}{N} \sum_i q_i \quad (4.9)$$

$$R = R_{rms} = \sqrt{\frac{\sum_i r_i^2}{N A_{res}}} \quad (4.10)$$

$$E_r = \frac{1}{2} m \dot{R}_{rms}^2 = \frac{(\sum_i \vec{r}_i \cdot \vec{p})^2}{2m(N R_{rms})^2} \quad (4.11)$$

$$T = \frac{2k}{\pi} \left(\frac{E_f E^*}{A_{res}} \right)^{0.5} = \frac{2k}{\pi} \left(\frac{E_f \left(\frac{1}{N} \sum_i \left(\frac{p_i^2}{2m} + U_i \right) - E_{bind}^o \right)}{A_{res}} \right)^{0.5}, \quad (4.12)$$

where the sums are over all particles in the residue, N is the number of test particles per nucleon, k is the Boltzmann constant and E_f is the Fermi-energy of the nucleus.

U is the potential energy (both nuclear and Coulomb), and E_{bind}^o is the binding energy of the ground state nucleus. E_{bind}^o is determined using the Weizäcker mass formula for a nucleus of mass A_{res} and charge Z_{res} . The EES model is initialized with these input parameters and used to calculate the statistical decay of the residue while allowing it to expand.

Figure 4.1 shows the values of these input parameters as a function of time, as predicted by BUU calculations for central collisions of 50 MeV/A ^{129}Xe on ^{51}V for both stiff and soft equations of state. As the reaction proceeds, a density cut is used to determine whether a nucleon is part of the residue. If the local density is greater than $\frac{1}{8}\rho_o$, the test particles are considered to be part of the residue. If not, the test particles are considered to be free.

The surfaces of the two nuclei are initially separated by 4 fm. For this system, the surfaces begin to touch at ≈ 12 fm/c. The nuclei then begin to overlap, however, until this time the two nuclei are completely separate entities. Since radius of the system is defined relative to the center of mass of the colliding system, the radius (and in turn E_r) does not reflect an expansion or compression of the residue during the initial stage of the reaction, but rather the motion of the two nuclei toward each other. At ≈ 20 fm/c, the nuclei now overlap, compression occurs, and the average density starts to increase. After the initial compression, the compound nucleus expands, particles begin to leave the residue, and A_{res} decreases slowly. At some point the nuclear attraction takes over, and the residue begins to compress again. This is analogous to the situation discussed in chapter 2 where, for sufficiently low temperatures, the pressure remains negative and thus the system holds together and cools by radiating particles. In fact, for the stiff EoS, several oscillations are seen during the first several 100 fm/c.

Another interesting feature of this figure is the change in the calculated mass

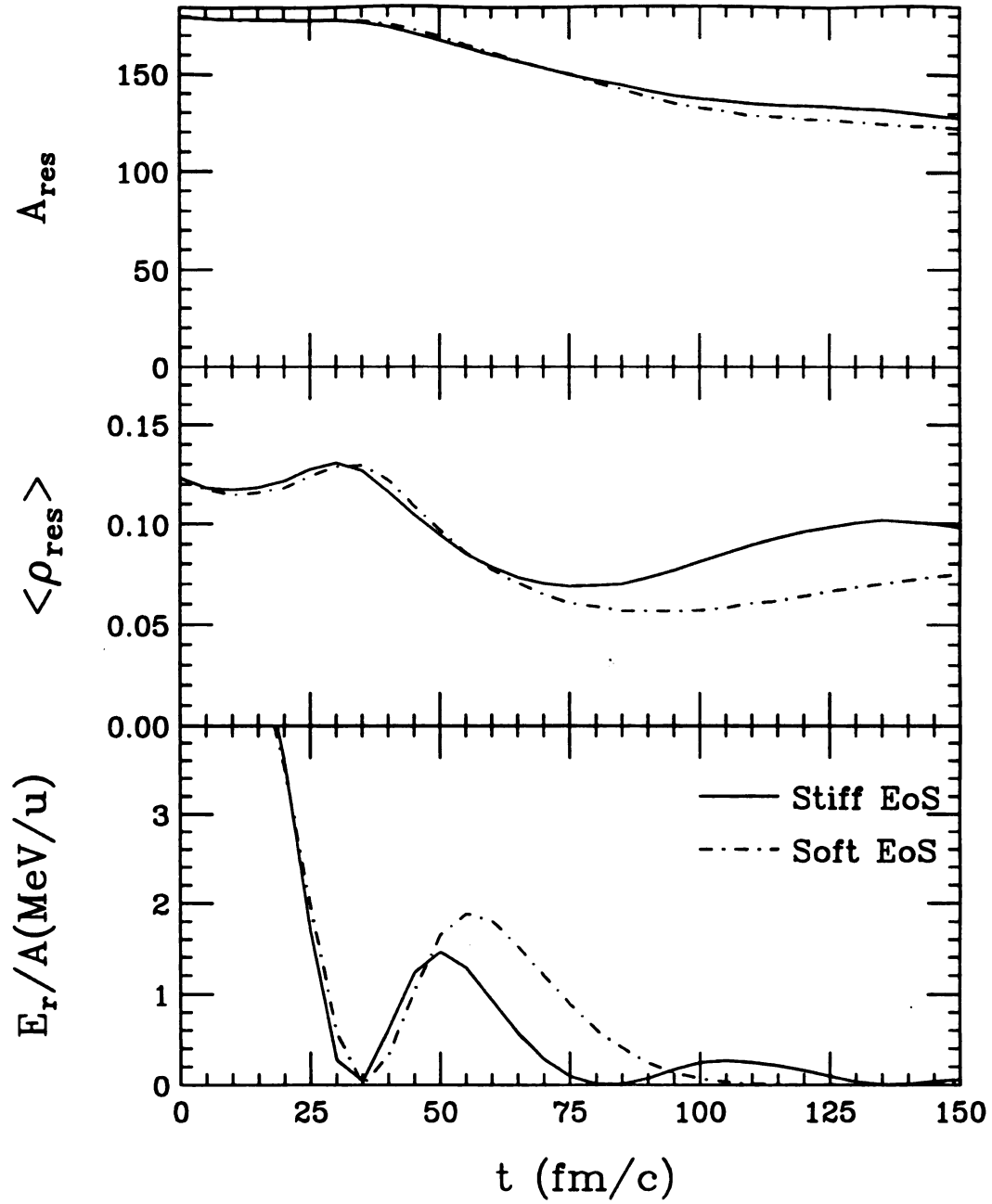


Figure 4.1: Mass, density and radial kinetic energy per particle of the residue in $50 \text{ MeV}/A$ $^{129}\text{Xe} + ^{51}\text{V}$. The solid curves represent calculations done using the BUU code with a stiff equation of state. The dotdashed curves represent the soft equation of state results.

and density of the residue. When the stiff equation of state is used, the magnitudes and variations of these quantities are approximately the same as those using the soft equation of state, except that they occur on a slightly faster time scale. However, the radial kinetic energy is much greater for the soft equation of state than for the stiff equation of state. This can be understood in the following way: the nuclei initially compress to a maximum density of ≈ 1.1 times normal density as the kinetic energy of the projectile gets randomized and transferred to target nucleons through individual nucleon-nucleon collisions. At this point, the short-range repulsive force stops the compression ($E_{rad} = 0$), and the residue begins to expand again. As the system expands, the mean density falls below the nuclear matter saturation value, and the intermediate-range attractive force tries to hold the residue together. In the stiff EoS parameterization, this attractive force is stronger than in the soft EoS, so the radial expansion slows down more quickly. Thus, the soft EoS system oscillates more slowly than the stiff, and also has larger radial kinetic energy maxima.

In figures 4.2 and 4.3, the same quantities are plotted for four different targets. In Figure 4.2, the stiff equation of state is used for central collisions of 50 MeV/A ^{129}Xe on ^{27}Al , ^{51}V , ^{89}Y and ^{197}Au . In Figure 4.3 a soft EoS is used for the same systems. For both equations of state, a systematic increase in the time at which maximum compression occurs with the size of the target is seen. In addition, for the three lightest targets, a similar systematic trend in maximum radial kinetic energy is seen. However, for the gold system, the radial kinetic energy curve appears to be shifted ≈ 5 fm/c to the right of the other curves and does not reach a higher maximum than the yttrium target. This is the only system in which the target is larger than the projectile. In this system, the kinetic energy of the projectile gets randomized and shared with more than twice as many nucleons as in the lighter system, thus less energy (per nucleon) is available for radial expansion.

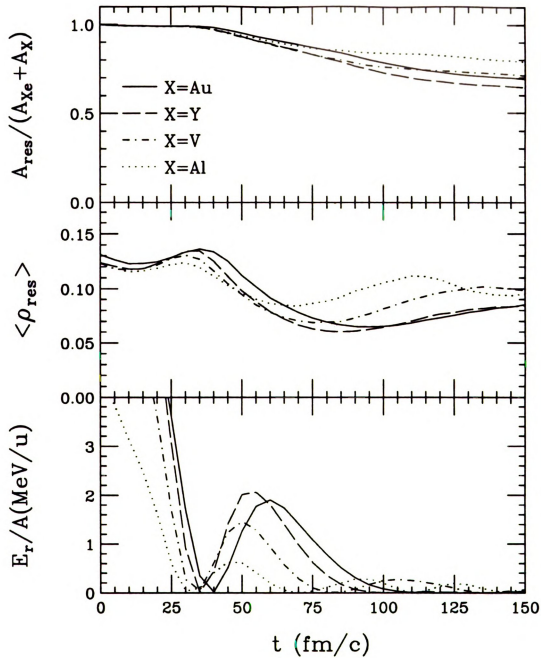


Figure 4.2: The mass, density and radial kinetic energy per particle of the residue in 50 MeV/A $^{129}\text{Xe} + ^{27}\text{Al}$, ^{51}V , ^{89}Y and ^{197}Au , predicted by the BUU code using a stiff EoS.

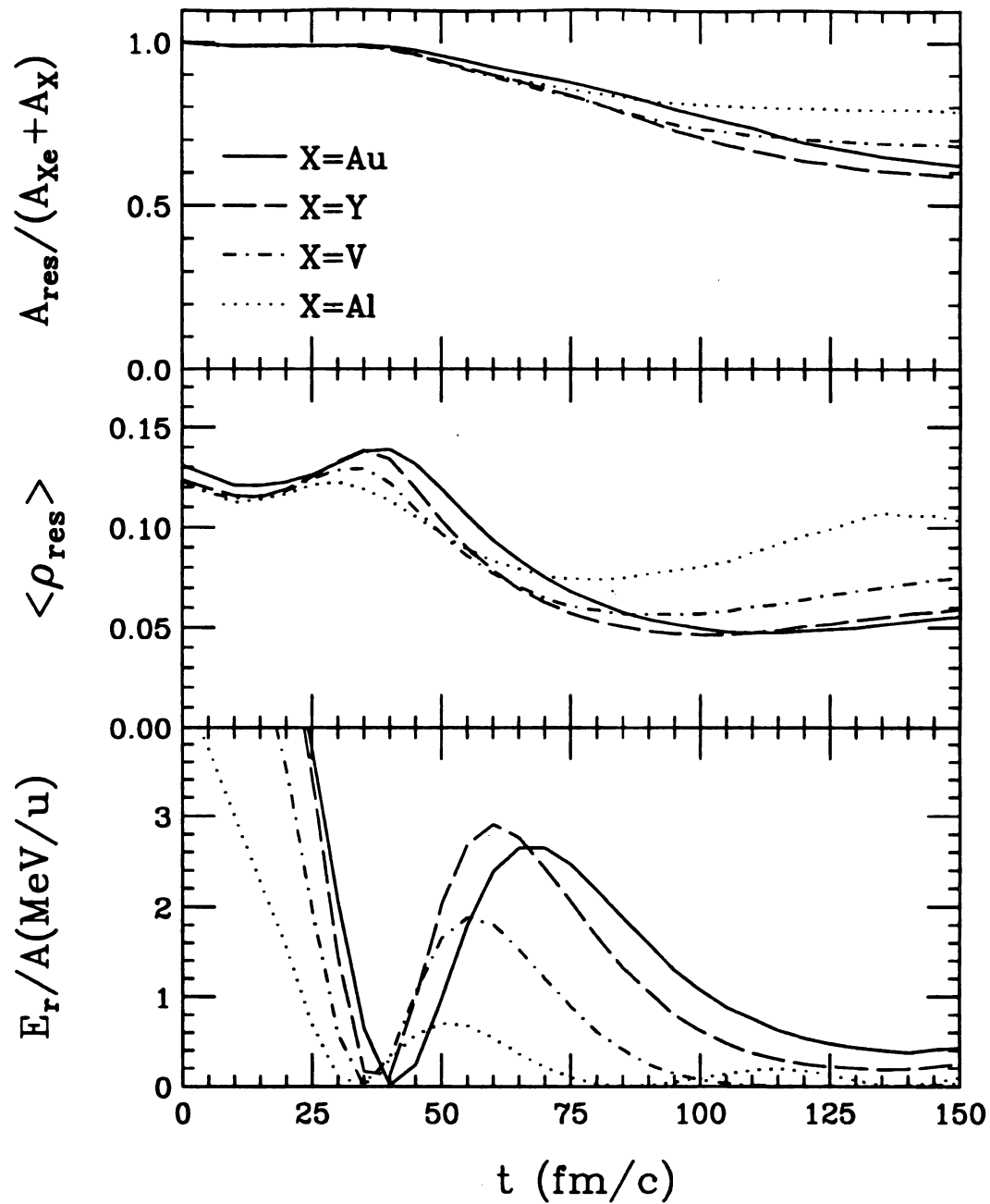


Figure 4.3: The mass, density and radial kinetic energy per particle of the residue in 50 MeV/A $^{129}\text{Xe} + ^{27}\text{Al}$, ^{51}V , ^{89}Y and ^{197}Au , predicted by the BUU code using a stiff EoS.

Another point to notice in Figure 4.3 is that the radial kinetic energy of the heavier systems (in particular the ^{89}Y and ^{197}Au systems) never returns to zero after the initial expansion begins. In these systems, the nuclear force for a soft EoS is not sufficiently strong to completely stop the expansion and hold the residual nucleus together. This will be shown more clearly in Figure 4.5.

While these figures provide insight into the behavior of the reaction zone, they do not provide the exact quantities needed in the EES calculations. The EES model assumes a uniform density distribution at normal nuclear matter density for the residue. However, the density distributions predicted by the BUU vary as a function of time. In order to best match the conditions assumed in the EES model, a time must be chosen when the BUU density distribution most resembles the assumptions of the EES model. This time is determined as the point when the central density of the BUU density distributions most resembles a uniform distribution with a central density equal to normal nuclear matter. From figures 4.1, 4.2 and 4.3, it appears that this instant in time will occur between the first maximum and minimum in the density of the residue.

To determine the transition point between the two models more precisely, the density profiles ($\rho(R)$) of the BUU calculation were plotted as a function of time. Two of these plots are shown in figures 4.4 and 4.5. A dashed line representing a constant density equal to normal nuclear matter density is drawn for reference. As seen in Figure 4.4, for the stiff equation of state, the nuclei are compressed at $t \approx 30$ fm/c to about 15% above normal nuclear matter density. However, as time progresses, the central region becomes more uniform, and at $t = 45$ fm/c, the central density is a uniform distribution at normal nuclear matter density. Another interesting feature is that, for this particular system ($^{129}\text{Xe} + ^{27}\text{Al}$), after expanding for an additional ≈ 40 fm/c, the attractive part of the nuclear force overcomes the expansion energy

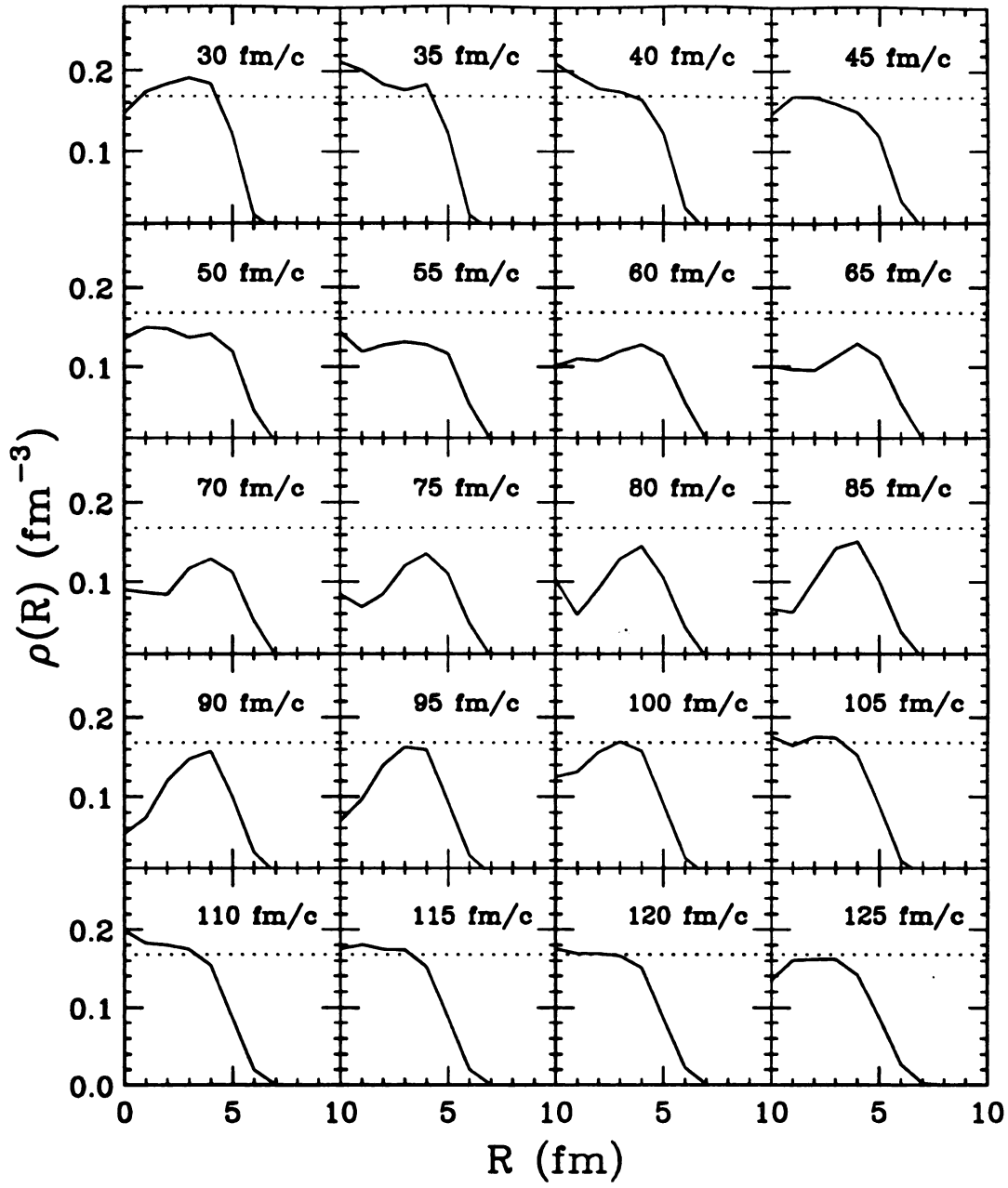


Figure 4.4: Density profile of residual nucleus from the BUU calculation for a stiff EoS for 50 MeV/A $^{129}\text{Xe} + ^{27}\text{Al}$.

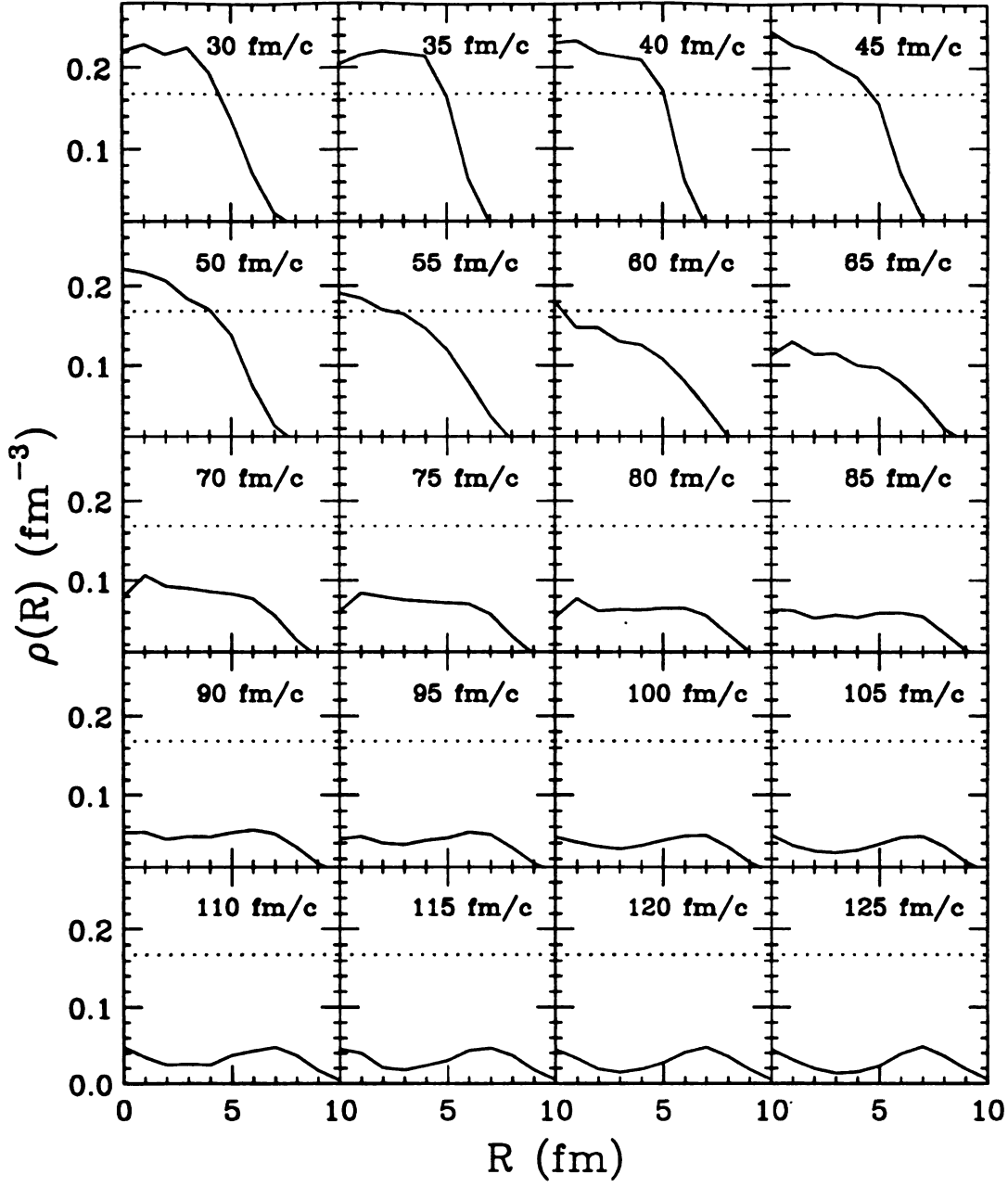


Figure 4.5: Density profile of residual nucleus from the BUU calculation for a soft EoS for 50 MeV/A $^{129}\text{Xe} + ^{89}\text{Y}$.

and the residue begins to recompress. In fact, by $t \approx 120$ fm/c, the system is once again a uniform distribution at normal nuclear matter density.

In Figure 4.5, an example of a system with a soft EoS that does not overcome the expansion energy is shown. In this $^{129}\text{Xe} + ^{89}\text{Y}$ system, the initial compression at $t \approx 30$ fm/c gives a central density almost 30% greater than that of normal nuclear matter. By $t \approx 55$ fm/c, the central density is as close to a uniform nuclear matter density distribution as possible. As time progress, the system continues to expand, and the nuclear force is never able to overcome the expansion energy.

As these figures show, the BUU density distributions never have a sharp surface. In fact, for the system shown in Figure 4.5, the distribution falls from nuclear matter density to zero over ≈ 5 fm. Some of the particles at these large radii may in fact be unbound, even though the local density can be greater than $\frac{1}{8}\rho_0$. These particles are at larger radius, which may have outward velocities high enough for them to be unbound, and should not be considered part of the residual nucleus. To determine the radius of the BUU residue to consider as A_{res} in the EES model, the average binding energy per nucleon as a function of radius is calculated. This is shown in Figure 4.6 along with the density profile at the transition time. In this calculation a soft EoS is used. A line has been drawn at $E_{bind} = 0$ to guide the eye. In the gold system, on average, the particles inside 8 fm have negative total energy and are considered bound. For the aluminum case, the cutoff radius is 6 fm. The arrows indicate the cutoff radii chosen for the two cases.

4.3 Comparison with Experiment

All of the necessary information now exists for combining the two model calculations. Both stiff and soft equations of state will be used in the BUU calculations to see how

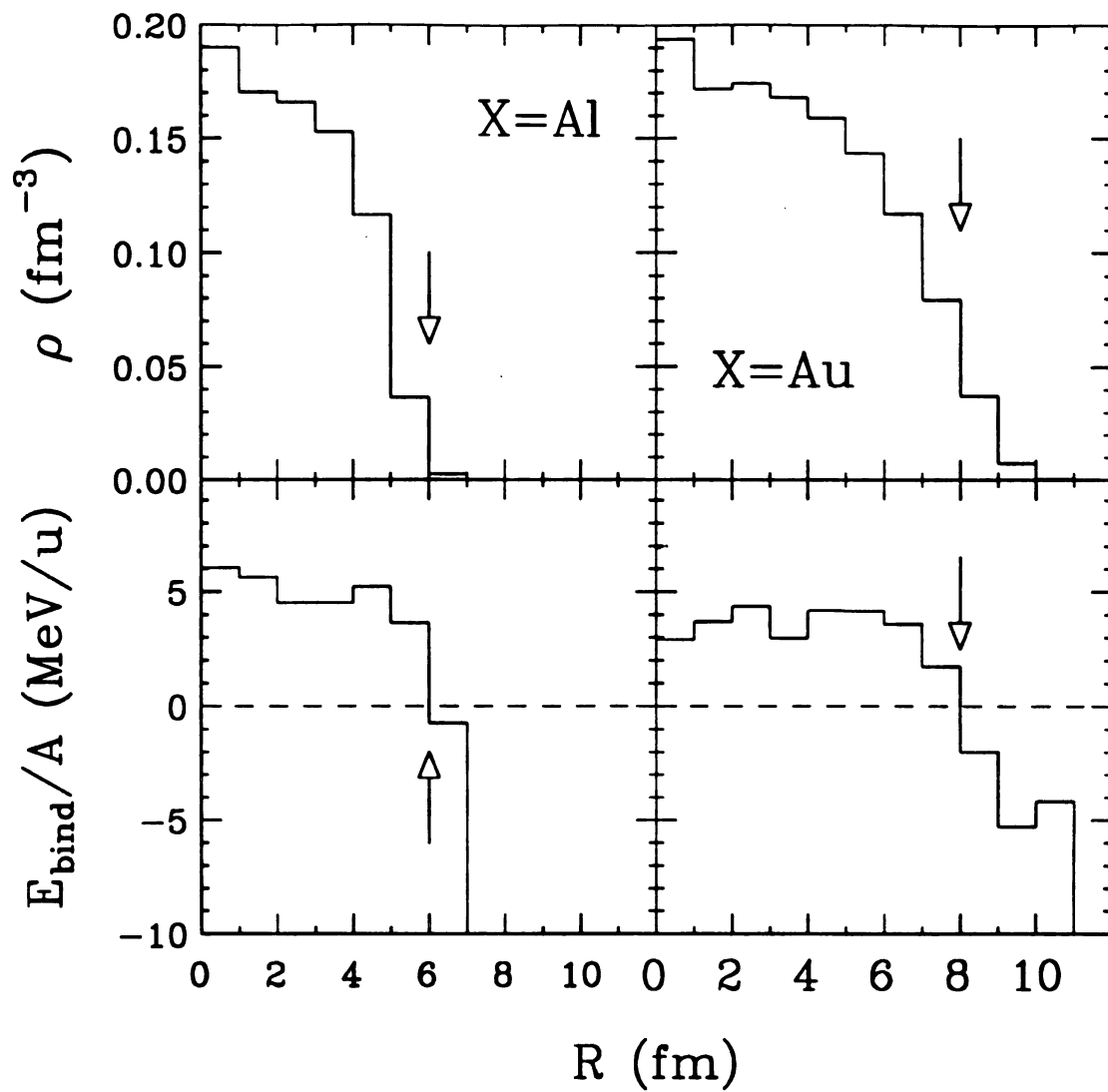


Figure 4.6: Binding energy and density profile of residual nucleus in the BUU calculation for a soft EoS for 50 MeV/A $^{129}\text{Xe} + ^{27}\text{Al}$, ^{197}Au . The calculations were done with a soft equation of state.

the EoS affects the final results. Table 4.1 shows the input values determined by BUU to be used in the statistical evaporation code EES for all of the experimental systems studied. In addition, the cutoff radius is not well defined. For this reason, the value described in the previous section is used as well as a cutoff radius 1 fm larger.

In addition to these four possible input sets from BUU for each reaction, there is one adjustable parameter (K_{EES}) in the EES model. The EES model is run for each parameter set in Table 4.1, with several values of K_{EES} . Figure 4.7 shows the data for four target-projectile combinations, each at a bombarding energy of $E/A = 50$ MeV. The enclosed regions with single-hatched lines are the unfiltered results of the hybrid model for various cutoff radii and compressibilities. The enclosed regions with double-hatched lines are the results filtered for geometrical acceptance of the detector. The two different regions on each plot are the result of increasing the radius cut by 1 fm. This has the effect of increasing the mass and excitation energy of the residue, thus increasing the number of IMFs produced in the EES model. The results are seen to be very sensitive to this radius parameter choice. Varying the compressibility parameter in the BUU calculation, creates the horizontal widths of the regions (the lower compressibility corresponds to the left side of the region), while the vertical spread is a result of changing the compressibility parameter in the EES code (the lower compressibility corresponds to the top of the region). The sensitivity of the model calculations to the various radius cutoffs and compressibilities will not allow precise determination of these parameters. However, the fact that the EES model is able to produce enough IMFs with reasonable input variables as determined by the BUU model, suggests that expansion of the residue is necessary to explain the observed IMF multiplicities.

Table 4.1: Input parameters for EES model predicted by BUU calculations.

Target	EoS	t (fm/c)	R _{cut} (fm)	Z	A	E [*] /A (MeV)	T (MeV)	E _{rad} (MeV)
²⁷ Al	stiff	45	6	54	127	2.5	5.7	62
		45	7	63	147	3.5	6.9	89
	soft	45	6	54	129	2.4	5.6	54
		45	7	63	148	3.1	6.5	80
⁵¹ V	stiff	45	6	56	137	5.0	8.4	110
		45	7	69	165	5.8	9.2	180
	soft	50	6	54	130	3.2	6.6	130
		50	7	67	159	4.2	7.6	230
⁸⁹ Y	stiff	50	7	75	180	6.1	9.5	290
		50	8	84	200	6.8	10.2	390
	soft	55	7	70	170	4.4	7.9	380
		55	8	82	196	5.2	8.6	510
¹⁹⁷ Au	stiff	55	8	108	271	6.2	9.6	390
		55	9	120	300	6.9	10.2	510
	soft	60	8	103	260	4.7	8.1	490
		60	9	118	293	5.3	8.7	660

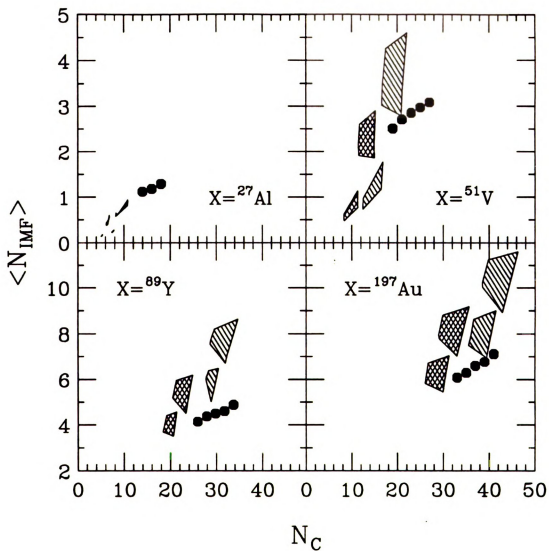


Figure 4.7: Charged particle multiplicities vs. mean number of IMFs for 50 MeV/A $^{129}\text{Xe} + ^{27}\text{Al}$, ^{51}V , ^{89}Y and ^{197}Au . The points represent the data. The boxed regions represent model predictions for various radius cuts and compressibilities. In each plot, the right set of boxes are unfiltered results and the left set are filtered with experimental efficiency cuts [Bow92].

Chapter 5

Evolution of the Reaction Zone

Through microscopic models, such as BUU, direct study of the evolution of the reaction zone is possible. By observing the single-particle phase space distribution as a function of time, features such as expansion, particle production and emission can be theoretically studied. However, experimentally measured single-particle observables, such as proton and pion spectra, probe only the final state momentum of the single-particle phase space distribution. Neither the mechanism which led to the final state nor any spatial information is directly studied, and information on how the system evolved is lost. However, certain two-particle observables, such as two-proton correlation functions, retain the space-time information on the evolution of the reaction zone. By comparing experimentally measured two-particle observables with results from microscopic models, more stringent restrictions can be placed on the models and better insight into the space-time evolution of heavy-ion reactions can be obtained.

5.1 Intensity Interferometry: HBT

The use of two-particle observables to study the size of the emitting source began a century ago. In 1890, A. A. Michelson proposed to measure the angular size of distant stellar objects using amplitude interferometry. His first measurements involved

observing the interference pattern from light emitted from the moons of Jupiter. Michelson performed a Young's double slit experiment by observing the light emitted from stellar objects after placing slits at the front of a telescope. By varying the slit separation the fringes of the interference pattern varied. By measuring the separation of the slits when the fringes disappeared, he was able to determine the angular sizes of these objects within 1 second of arc. Using mirrors to extend the acceptance of the telescope, he was able to extend this method to objects subtending even smaller angles, and in 1920 was able to determine the size of Arcturus. Increasing the separation of the mirrors to 121 in, Michelson was able to measure the size of Betelgeuse (determined to be 0.047 seconds of arc) and combined with distance measurements, determine a radius of more than 270 times that of the sun [Mic27].

The limitation of amplitude interferometer is that the separation of the mirrors is inversely related to the angular size of the object. In order to measure stellar objects with smaller angular sizes, the mirror separation must increase and accurate placement of the mirrors over long baselines is difficult. In addition, the measurement of first-order interference patterns assumes that light of both paths experienced the same distortions as they travelled to the detector. It is impossible to verify that atmospheric distortions were identical for both paths. These problems can be overcome by looking at second-order interference patterns using intensity interferometry.

In 1956, R. Hanbury-Brown and R. Q. Twiss proposed to use intensity interferometry to study stellar objects [Han54, Han56a, Han56b]. The use of intensity interferometry is often referred to as the Hanbury-Brown–Twiss (HBT) method. The principle is similar to that of the Michelson interferometer: light from a single stellar object which follows two different paths is observed on earth. However, instead of recombining the paths at the telescope and studying the interference patterns, the intensity of the photons from each path is recorded simultaneously. Any fluctuation

in the intensity which is due to the source will be present in both signals. Thus, observing the fluctuations in the signal relative to the constant background provides information on the size of the emitting source. Using this method they were able to measure the angular size of Sirius to be 0.0069 seconds of arc [Han56b]. New correlation interferometers are more than 10 times more sensitive than the original HBT interferometer.

The measured intensity fluctuations can be caused by many things. For instance, the effect of Bose-Einstein statistics is to enhance the number of photons with the same momentum emitted from the same source. The actual astronomical measurement consisted of measuring the coincidence yield photons emitted by the stars. The correlation function was defined as:

$$R(\vec{k}_1, \vec{k}_2) = \frac{\Pi_{12}(\vec{k}_1, \vec{k}_2)}{\Pi_1(\vec{k}_1)\Pi_1(\vec{k}_2)} - 1, \quad (5.1)$$

where Π_{12} is the probability of observing two photons, one with momentum \vec{k}_1 and the other with momentum \vec{k}_2 , and Π_1 is the probability of measuring a single photon with momentum \vec{k}_i . With this definition, the correlation function would go to unity for photon pairs with identical momentum.

The methods developed by Hanbury-Brown and Twiss can be applied to all type of particles. Particle physicists realized that similar measurements can be performed for pion sources and in 1959, Goldhaber *et. al.* showed that the Bose-Einstein enhancement of pion production in $p\bar{p}$ annihilation experiments was observable [Gol59, Gol60]. Since then, a large number of pion correlation experiments have been done [Bau92, Bau93].

In 1977, Koonin suggested that this method could also be applied to fermionic systems [Koo77]. Unlike the enhancement seen in bosonic systems due to their Bose-Einstein statistics, identical fermions should show a decreased correlation due to

the Pauli exclusion principle. In addition, other types of interactions, such as the Coulomb interaction for charged particles, will also affect the correlation function. In the case of protons, the most striking features of the correlation function are due to the nuclear and Coulomb interaction of the protons.

Since that time, two-particle intensity interferometry has been successfully used to study the evolution of the hot reaction zone formed in heavy-ion collisions [Bau92, Bau93]. In particular, two-proton interferometry measurements at small relative angles have been able to give information on the size of the emitting source by comparing the measured correlation functions with calculations using zero-lifetime Gaussian sources. However, this is only a parameterization of an average source size and provides limited information on the space-time evolution of the collision zone.

More detailed calculations using the BUU hadronic transport model are in good agreement not only with single-particle observables, such as proton energy spectra, but also the two-particle correlation functions [Gon91, Bau93]. However, these measurements are impact parameter averaged, so while detailed information on the reaction zone can be extracted from model calculations as a function of impact parameter, experimental observation of these effects did not exist. More recently, measurements were performed with a 4π detection device allowing centrality selected single-particle and two-particle observables to be determined. The proton transverse energy spectra predicted by BUU were already shown to be in good agreement with the data in Figure 3.1. In section 5.3, comparison of measured correlation functions with the theoretical calculations will be made. First, however, the Koonin formalism for calculation of the correlation function and the role of BUU will be described.

5.2 The Correlation Function

What is commonly referred to as the two-particle correlation function is related to the quantity measured by Hanbury-Brown and Twiss $R(\vec{k}_1, \vec{k}_2)$ through:

$$C(\vec{P}, \vec{q}) = R(\vec{P}, \vec{q}) + 1 = \frac{\Pi_{12}(\vec{p}_1, \vec{p}_2)}{\Pi_1(\vec{p}_1)\Pi_1(\vec{p}_2)}, \quad (5.2)$$

where $\vec{P} = \vec{p}_1 + \vec{p}_2$ and $\vec{q} = \frac{1}{2}(\vec{p}_1 - \vec{p}_2)$.

Just as in the HBT analysis, the correlation function is defined as the ratio of the probability of observing a pair of particles (Π_{12}), one with momentum \vec{p}_1 and the other with momentum \vec{p}_2 , relative to the probability of observing two single particles (Π_i) with momentum \vec{p}_i , where $i = 1, 2$. Early comparisons with data assumed the correlation function could be expressed as:

$$C(\vec{P}, \vec{q}) = \int d^3r F_{\vec{P}}(\vec{r}) \left| \phi(\vec{q}, \vec{r}_1 - \vec{r}_2 + \frac{\vec{P}(t_2 - t_1)}{2m}) \right|^2, \quad (5.3)$$

where $F_{\vec{P}}(\vec{r})$ is a source function which describes the size and lifetime of the source and $\phi(\vec{q}, \vec{r}_1 - \vec{r}_2 + \frac{\vec{P}(t_2 - t_1)}{2m})$ is the relative wave function of the particles. The relative wave function for two protons at a relative angle of 60° between \vec{q} and \vec{r} is shown in Figure 5.1. The wave function vanishes at $r = 0$ due to the Coulomb repulsion of the protons. The strong peak at $q \approx 20$ MeV/c is often referred to as the ^2He resonance and is due to the strong nuclear interaction between the protons. By assuming Gaussian parameterizations of the source, it was shown that this ^2He resonance in the relative wave function showed up as a strong enhancement in the correlation function at $q \approx 20$ MeV/c. In addition, this enhancement was stronger for sources of smaller spatial and temporal extent. The reason for this is shown schematically in Figure 5.2. If two protons are emitted close together in space and time (5.2(a)), they will interact very strongly. However, if they are emitted from either a long-lived source (5.2(b)), or a large source (5.2(c)), they will interact less strongly.

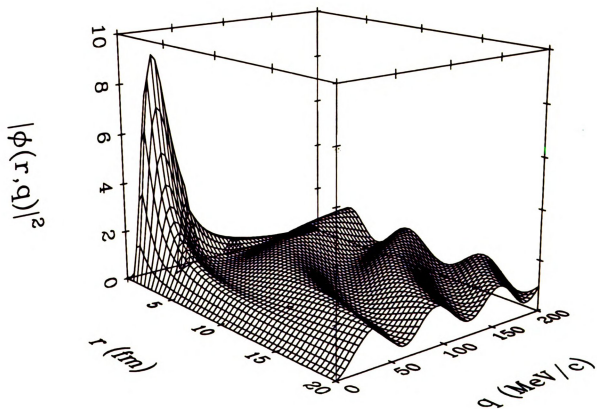
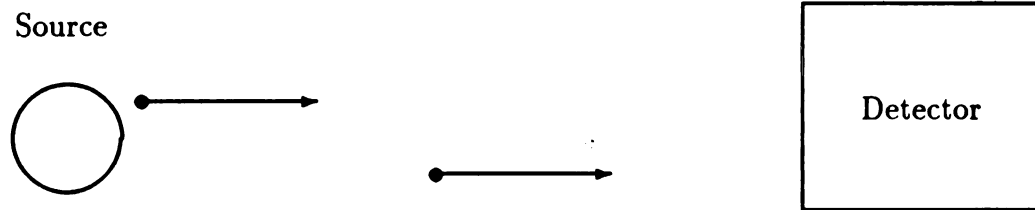


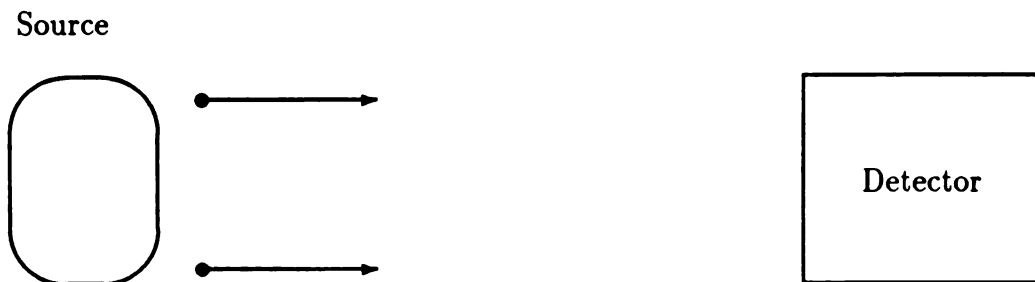
Figure 5.1: The relative wave function, $|\phi(q, r, \cos(\theta))|^2$, for fixed angle $\theta = 60^\circ$ as a function of relative position and momentum [Bau92a].



(a)



(b)



(c)

Figure 5.2: Schematic representation of two particles emitted from a source. In (a) the two particles are emitted from a small, short-lived source. In (b) the particles are emitted from a small, long-lived source. In (c), the particles are emitted from a large, short-lived source.

The original formalism proposed by Koonin suggested that the source function could be calculated in a microscopic model, for example in BUU. By assuming that final-state interactions between the particles and their source are negligible and that the two-particle interactions dominate, detailed calculation of the correlation function was possible[Gon91]. Under these conditions, the correlation function can be written in terms of the relative wave function and the single particle emission probability ($g(\frac{1}{2}\vec{P}, x_2)$):

$$C(\vec{P}, \vec{q}) = \frac{\int d^4x_1 d^4x_2 g(\frac{1}{2}\vec{P}, x_1) g(\frac{1}{2}\vec{P}, x_2) |\phi(\vec{q}, \vec{r}_1 - \vec{r}_2 + \frac{\vec{P}_1(t_2 - t_1)}{2m})|^2}{\int d^4x_1 g(\frac{1}{2}\vec{P}, x_1) \int d^4x_2 g(\frac{1}{2}\vec{P}, x_2)}, \quad (5.4)$$

where x_i is the space-time emission point of the particles.

This can be reduced to the form given in equation 5.3 by defining the source function in terms of the probability of emission:

$$F_P(\vec{r}) = \frac{\int d^3R f(\frac{\vec{P}}{2}, \vec{R} + \frac{\vec{r}}{2}, t_>) f(\frac{\vec{P}}{2}, \vec{R} - \frac{\vec{r}}{2}, t_>)}{|\int d^3r' f(\frac{\vec{P}}{2}, \vec{r}', t_>)|^2}, \quad (5.5)$$

where $\vec{R} = \frac{1}{2}(\vec{r}_1 + \vec{r}_2)$ is the center of mass coordinate of the two particles and $t_>$ is some time after both particles are emitted. The single-particle phase distribution, $f(\vec{p}, \vec{r}, t)$, predicted by the BUU transport model is related to the emission probability through:

$$f(\vec{p}, \vec{r}, t_>) = \int_{-\infty}^{t_>} dt g(\vec{p}, \vec{r} - \vec{p}(t_> - t)/m, t). \quad (5.6)$$

Although equations 5.3 and 5.4 express the correlation function in terms of six variables, no experiment has sufficient statistics or detector resolution to measure the full 6-dimensional correlation function. Thus, 4-dimensions are usually integrated

over, and the correlation function is plotted as a function of $|\vec{P}|$ and $|\vec{q}|$. In Figure 5.3 the calculated two-proton correlation function is shown for 75 MeV/A $^{14}\text{N} + ^{27}\text{Al}$ at $\langle\theta_{lab}\rangle = 25^\circ$ for $P = 500$ MeV/c [Gon91]. The dominant feature of the proton correlation function is a strong peak at $q \approx 20$ MeV/c, just as expected from the ^2He resonance of the relative wave function. In addition, the correlation function goes to zero as $q \rightarrow 0$, due to the Coulomb repulsion of the proton pair. For large q , where correlations between proton pairs are expected to be unimportant, the correlation function is ≈ 1 .

In these calculations, the in-medium nucleon-nucleon cross section was varied between 0 and the free value (σ_{nn}). It might be possible that σ_{nn} is modified in nuclear matter, and as the figure shows, the height of the correlation function peak is sensitive to this effect as it increases for higher values of σ_{nn} . This is because increasing σ_{nn} increases the number of nucleon-nucleon collisions and since rescattering after hard collisions can only serve to increase the effective size of the system, the peak at $q \approx 20$ MeV/c decreases.

In addition, for σ_{nn} equal to the free value, the correlation functions for two different equations of state are shown in Figure 5.3. While there is only a small difference between the two curves, the soft EoS result has a slightly lower peak value. It is not surprising that the difference between using a soft and a stiff nuclear equation of state is much less pronounced. For the beam energy and system size considered here, the maximum densities reached are not much above nuclear matter density, and compressional effects should play only a minor role.

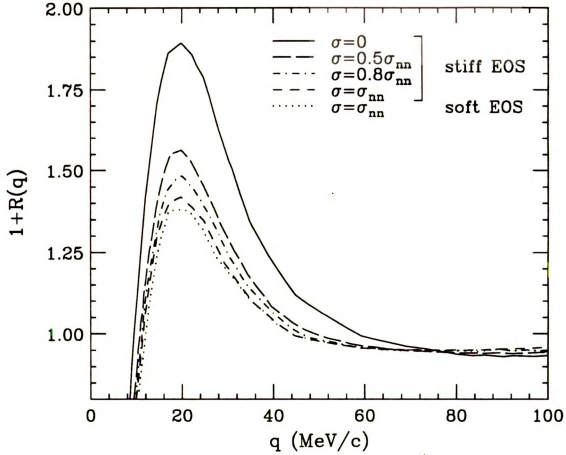


Figure 5.3: Correlation functions calculated for 75 MeV/A $^{14}\text{N} + ^{27}\text{Al}$ at $\langle\theta_{lab}\rangle = 25^\circ$ for $P = 500$ MeV/c. The different lines represent BUU predictions using different values of σ_{nn} and nuclear EoS [Gon91].

5.3 Comparison with Experiment

To compare the results of the BUU calculations to the data, both σ_{nn} and the EoS are varied to find the best agreement. Figure 5.4 shows a comparison of the experimentally measured correlation functions with the results of the BUU calculations. The reaction is the same as in Figure 5.3, 75 MeV/A $^{14}\text{N} + ^{27}\text{Al}$ at $\langle\theta_{lab}\rangle = 25^\circ$. The calculations shown are done with the in-medium σ_{nn} set to the free value and a stiff EoS, and are in good agreement with the data. As the figure shows, the peak height of the correlation function increases with the total momentum of the proton pairs. In terms of source sizes, this means the fastest pairs of protons are being emitted from a smaller source (or closer in time) than the slowest pairs of protons. Since the reaction zone is continuously evolving, the different momentum bins are representative of the different stages of this evolution. In particular, the fastest pairs are being emitted in the early stages of the collision, when the compression is the largest. As the source expands and cools, the emitted protons are less energetic and thus the slower pairs are emitted during the later stage of the reaction.

While this appears to be a logical explanation of the observed results, the correlation functions discussed here are the result of impact-parameter-averaged calculations. The reaction zone formed during peripheral events is expected to be much different than the source formed in a more central event. For example, in figures 5.5 and 5.6 the emission points of protons from 80 MeV/A $^{36}\text{Ar} + ^{45}\text{Sc}$ collisions at impact parameters of 2.5 fm and 6 fm, respectively, are shown as a function of time. The emission points for protons emitted in the reaction plane are shown for time bins of 10 fm/c width. To do this, the x and z emission points for all protons with y-coordinates given by $-1 \text{ fm} < y < 1 \text{ fm}$ are plotted. The upper left panel of both figures shows the protons which are emitted before 30 fm/c. The bottom right panel shows all

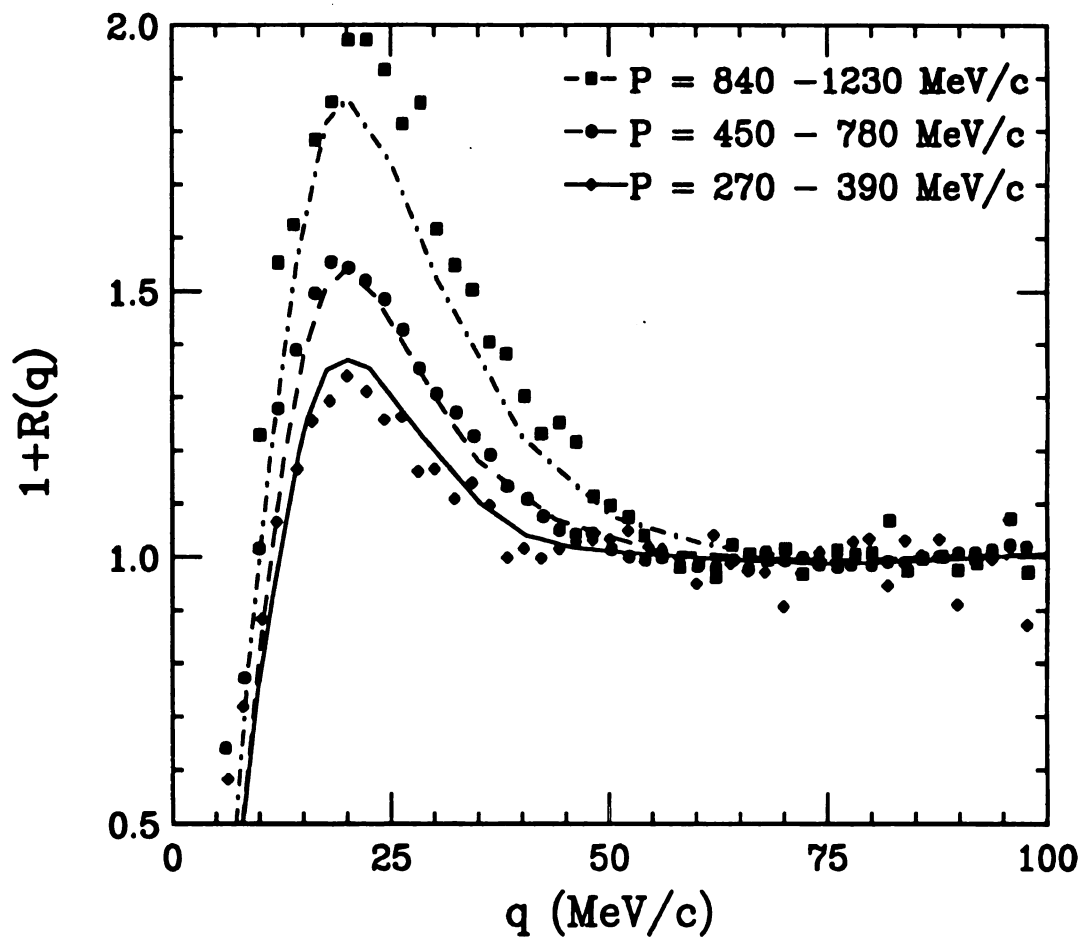


Figure 5.4: Correlation functions for 75 MeV/A $^{14}\text{N} + ^{27}\text{Al}$ at $\langle\theta_{lab}\rangle = 25^\circ$. Data are given by solid symbols. BUU calculation results are given by the curves [Gon91].

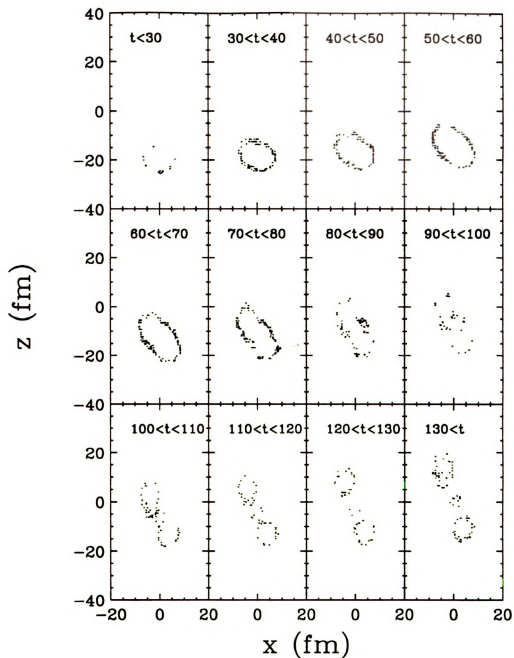


Figure 5.5: Proton emission points in the reaction plane for 80 MeV/A $^{36}\text{Ar} + ^{45}\text{Sc}$ at $b = 2.5$ fm. The 12 panels show the emission points of protons emitted in 10 fm/c time steps. The upper left panel shows emission points of protons emitted during the earliest time step ($t < 30$ fm/c) while the lower left panel shows the emission points of protons emitted during the latest time step ($130 \text{ fm/c} < t$).

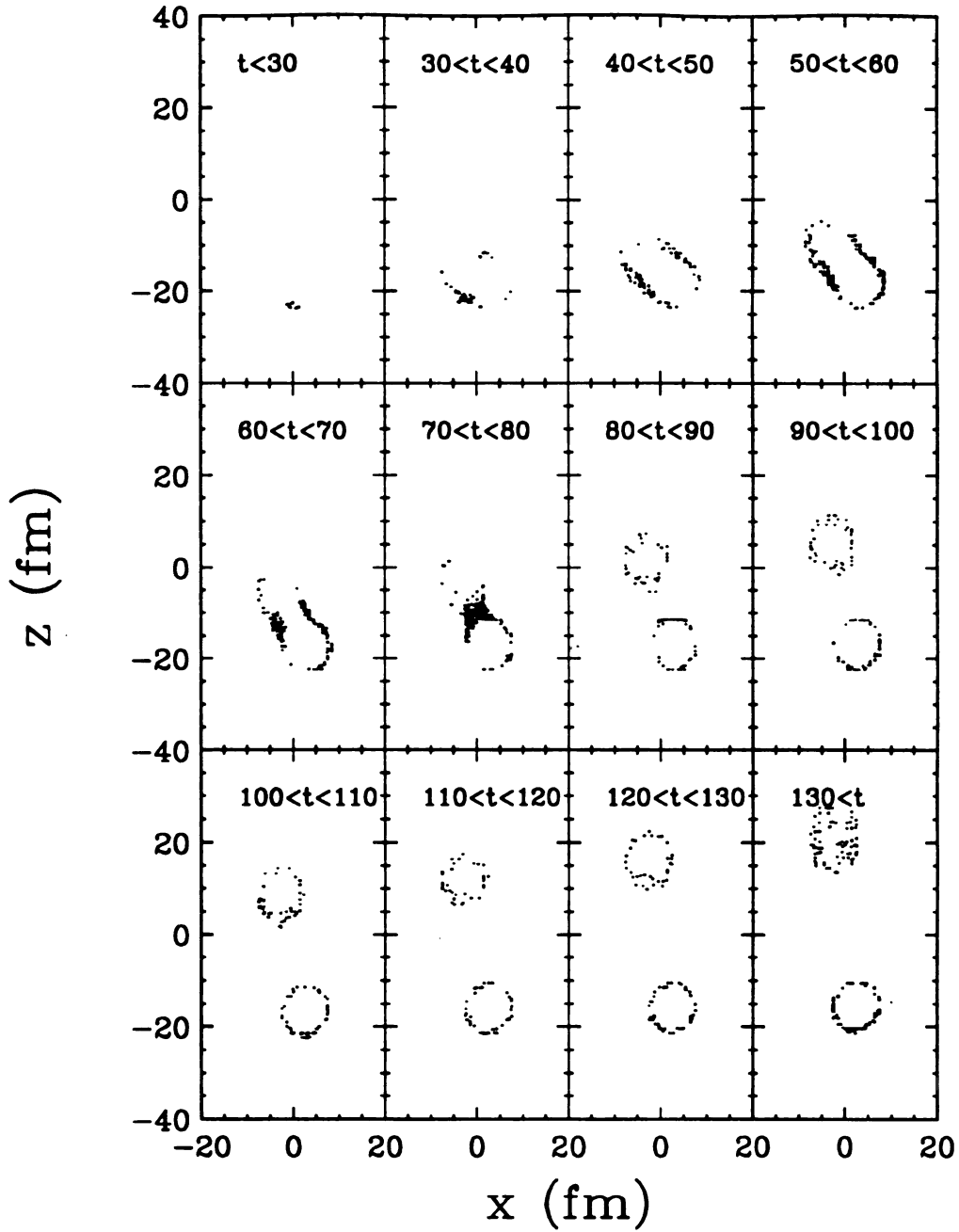


Figure 5.6: Proton emission points in the reaction plane for 80 MeV/A $^{36}\text{Ar} + ^{45}\text{Sc}$ at $b = 6$ fm. The 12 panels show the emission points of protons emitted in 10 fm/c time steps. The upper left panel shows emission points of protons emitted during the earliest time step ($t < 30$ fm/c) while the lower left panel shows the emission points of protons emitted during the latest time step ($130 \text{ fm/c} < t$).

protons emitted after 130 fm/c. These calculations are performed in the laboratory frame with the scandium nucleus initially at rest with its center at $(x, z) = (1.25 \text{ fm}, -19 \text{ fm})$ for the $b = 2.5 \text{ fm}$ case and $(3 \text{ fm}, -19 \text{ fm})$ for the $b = 6 \text{ fm}$ case. The argon nucleus is moving at a speed of approximately $0.38 c$ in the positive z -direction, with its center at $x = -1.25 \text{ fm}$ for the first figure and -3 fm for the second.

As the nuclei begin to touch around $\approx 10 \text{ fm/c}$, the nuclei compress. Around $\approx 25 \text{ fm/c}$ the nuclei overlap is nearly complete in the central region and protons are emitted from this hot reaction zone. As the reaction proceeds, the reaction zone expands and moves in the beam direction while protons are emitted from the surface. Since these are non-central collisions, the reaction zone begins to stretch: the nucleons on the negative x plane continue in the positive z direction, while the nucleons on the positive x plane, although they have gained some of the beam momentum, move much more slowly in the positive z direction. For the more central collision, the source becomes very elongated in the z direction and at the latest time steps begins to show 3 separate emission zones: the projectile-like and target-like remnants as well as a central fireball region. The peripheral reaction never develops a third region.

Central collisions are expected to reach higher densities and temperatures than peripheral collisions. This is due to the larger number of participant nucleons in the overlap region for central events. Initially, protons are emitted from this compressed overlap region, which is larger for the central collisions. Then, as the reaction progresses, protons are emitted from the expanding source and cooling should occur. Also, since the reaction zone formed in a peripheral collision is not as hot as in a central event, fewer protons should be emitted.

Can these differences in source evolution be observed? In order to answer this question, another experiment was performed where gating on centrality was possible. In the second experiment, $80 \text{ MeV/A } ^{36}\text{Ar} + ^{45}\text{Sc}$ collisions were studied at a lab angle

of $\langle \theta_{lab} \rangle = 38^\circ$. In Figure 3.1, the proton transverse energy spectra were shown for both the experimental results and the BUU calculations. In Figure 5.7, the correlation functions for central and peripheral collisions are shown. Once again, the agreement is good, although the peak heights are slightly underpredicted for the peripheral gates. The proton transverse energy spectrum also showed a similar underprediction by the BUU results. In Figure 5.8 the peak height at $q \approx 20$ MeV/c as a function of total momentum for both central and peripheral collisions is presented. On the right axis, the apparent source size for a zero-lifetime Gaussian source which gives a peak height corresponding to the left axis is shown. In both theory and experiment, the source for the peripheral events is smaller than the source for the central events for the slow momentum pairs ($P \leq 700$ MeV/c). For the high momentum pairs, experimentally, the central source is of comparable size, while the central events are smaller than the peripheral events for the BUU predictions. In the theoretical calculations, the high momentum protons are produced in the early, compressed stage of the collisions. The central collisions reach higher central densities, and thus a smaller, more compact source is formed than in the peripheral events.

In both central and peripheral events, the BUU predictions reproduce the trend of the data: the peak height increases with increasing total momentum. However, the BUU results slightly underpredict the peak height, especially for the peripheral events. This underprediction corresponds to a difference in source radii of about 0.5 fm between theory and experiment. The correlation functions for peripheral collisions are most sensitive to the exact definition of centrality and the differences between the experimental and theoretical curves shown in figures 5.7 and 5.8 could be due to the difference in the range of impact parameters chosen in the theoretical calculations as compared to the experimental impact parameter averages.

Once again, it must be emphasized that the BUU results are only a description

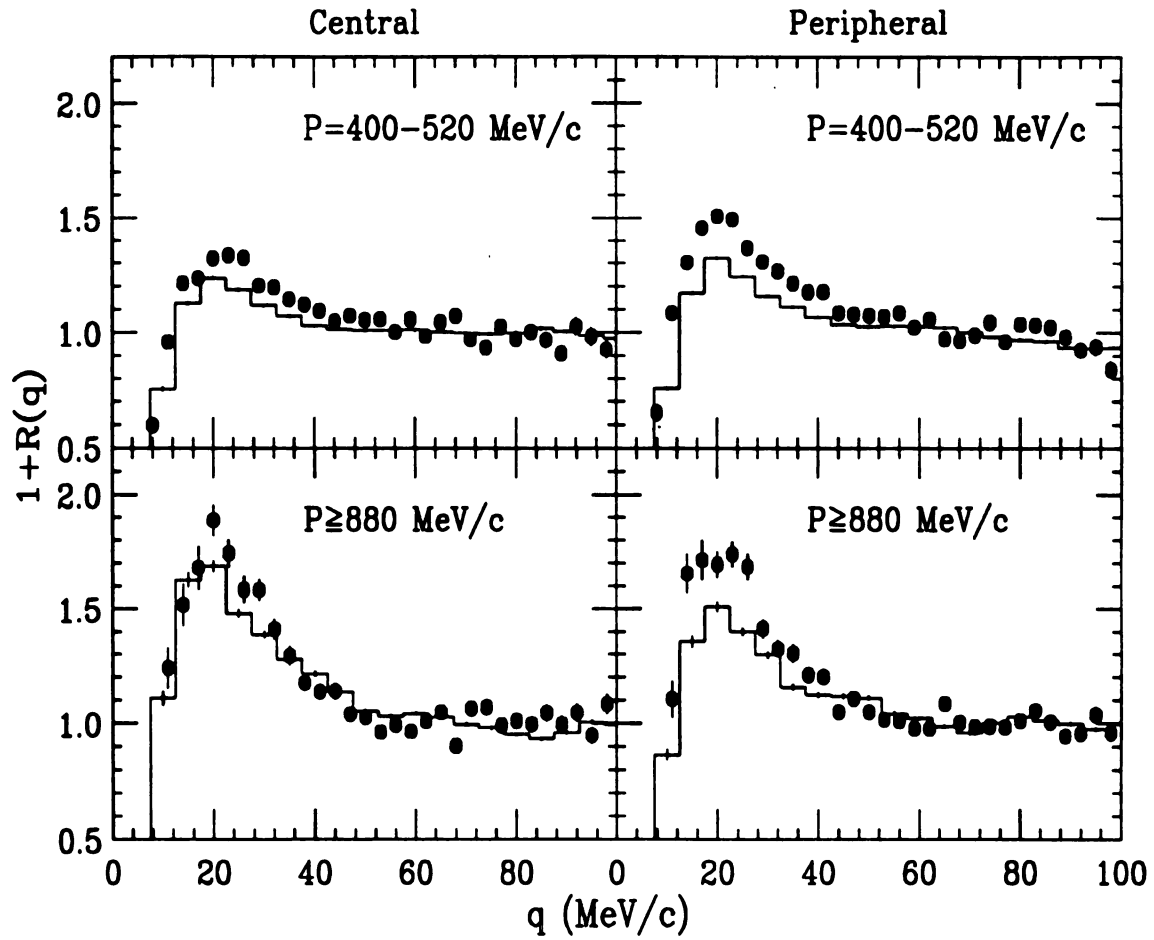


Figure 5.7: Correlation functions calculated for 80 MeV/A $^{36}\text{Ar} + ^{45}\text{Sc}$ at $\langle \theta_{lab} \rangle = 38^\circ$. The solid points represent the experimentally measured correlation functions while the histograms represent correlation functions predicted by BUU [Lis93].

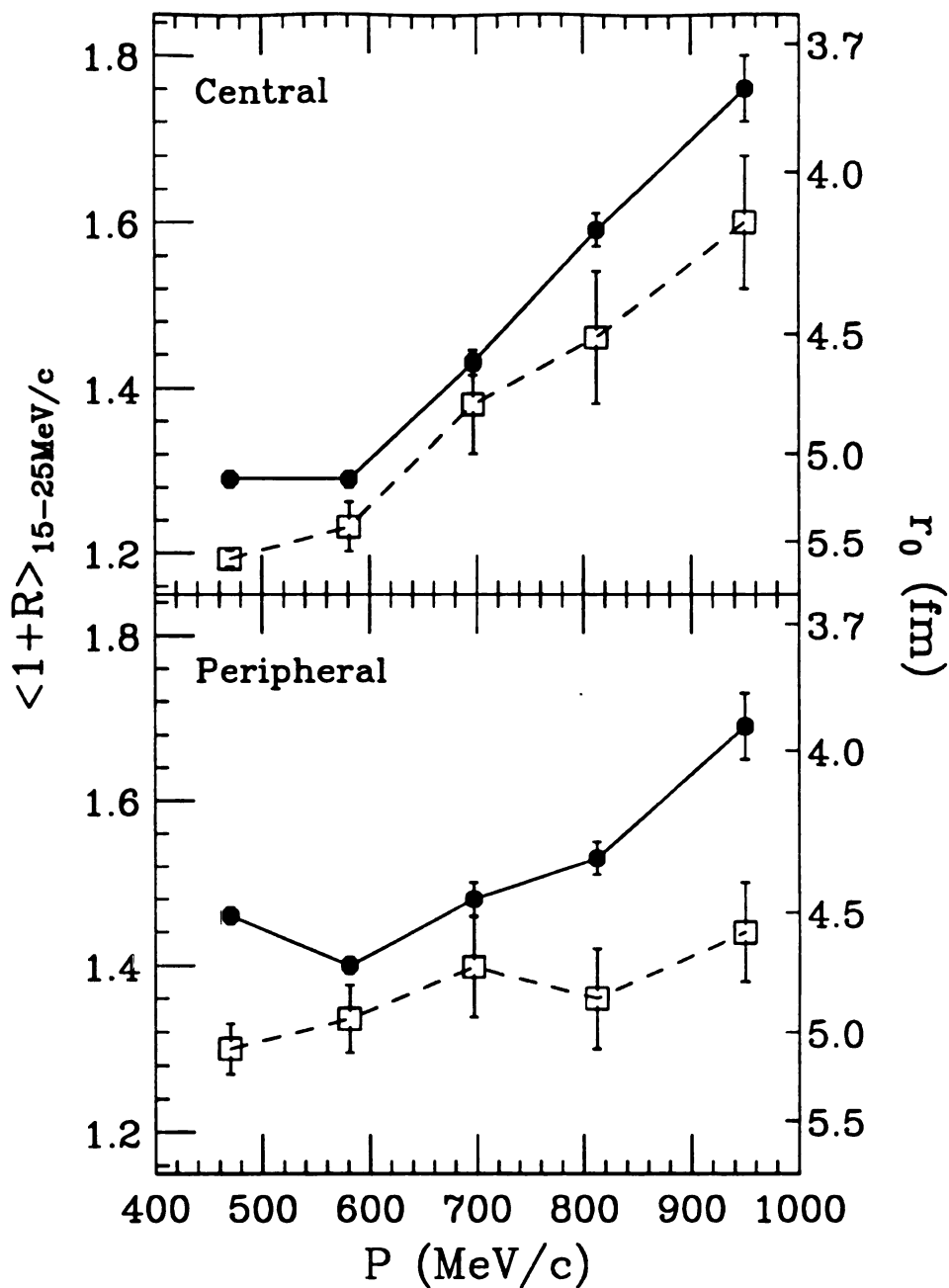


Figure 5.8: Average peak height of the two-proton correlation function as a function of total momentum for 80 MeV/A $^{36}\text{Ar} + ^{45}\text{Sc}$ at $\langle\theta_{lab}\rangle = 38^\circ$. The scale on the right axis is the Gaussian source radius. The solid points represent the experimental correlation functions, open points represent the predictions of BUU [Lis93].

of the average properties of single-particle observables. Fragment production is not considered in the calculations and exact agreement is not to be expected. However, the good agreement obtained between the experimental results and the theoretical calculations implies that fragment production does not significantly affect the two-proton correlation function. This could be due to two reasons. First, the fast protons are emitted early in the collisions, before heavier fragments are expected to be formed. At this stage in the collision, most of the emitted particles should have charge less than two, and thus, the high momentum pairs should not be affected greatly. Second, experimental studies have shown that most fragment spectra are forward peaked. Thus, fragments are emitted in the direction of the beam. If a coalescence-type model for fragment production is assumed, then the protons “close” in phase space with low transverse momentum would be removed from the sample of free protons and bound into fragments. However, the detector for the correlation function measurement is located at 45° , thus these protons are not being considered in the correlation function calculation, anyway.

The current studies have shown that using the single-particle phase space predicted by BUU in the Koonin formalism to calculate two-particle correlation functions provides insight into the space-time evolution of the reaction zone. Further studies at higher beam energies would be useful to confirm the assumption that fragment production does not significantly affect the correlation function at 45° . As the beam energy increases, the system expands much more quickly and fragment production decreases. Thus comparable agreement at higher beam energies would serve as a confirmation of the conclusions of this work.

In addition, as beam energies increase to around 1 GeV/nucleon, the compression reached in the early stages of the reaction should be several times greater than those reached in the current studies. Thus, the compressibility of nuclear matter should

play a more active part in these comparisons. Perhaps the compressibility constant of the nuclear matter EoS can be “pinned” down at relativistic beam energies more so than at the current beam energies.

Chapter 6

Nuclear Shadowing

All of the previous chapters have dealt with a mean-field approach to studying the nuclear interaction. However, the derivation of the correct form of the mean field from nuclear forces is difficult, at best. At a fundamental level, it is known that quarks and gluons are the building blocks of nucleons. Thus, QCD should be used as a basis for deriving the nuclear forces. However, QCD is only tractable at high energies, where perturbative calculations are possible. At the energies considered here, perturbation theory is not valid. One other possibility is to derive the nuclear force from field theory. In this picture, nuclear forces are mediated by particles, just as the photon mediates the electric force in QED, and similar formalisms can be used.

It has been proposed that the long- and short-range parts of the nuclear force can be described by several mediating particles or fields. Figure 6.1 shows a schematic of the nuclear potential and the possible mediating particles [Mac86]. The one-pion-exchange model (OPE) was proposed to describe the nuclear interaction for separations above a few fermi [Tak51]. The early success of this model was demonstrated by its ability to reproduce measured results between 1958-1965 [Bre60, Czi59, Gle62, Iwa56, Iwa56a, Won59].

The observation of the ω particle in 1961 provided a possible mediator for the

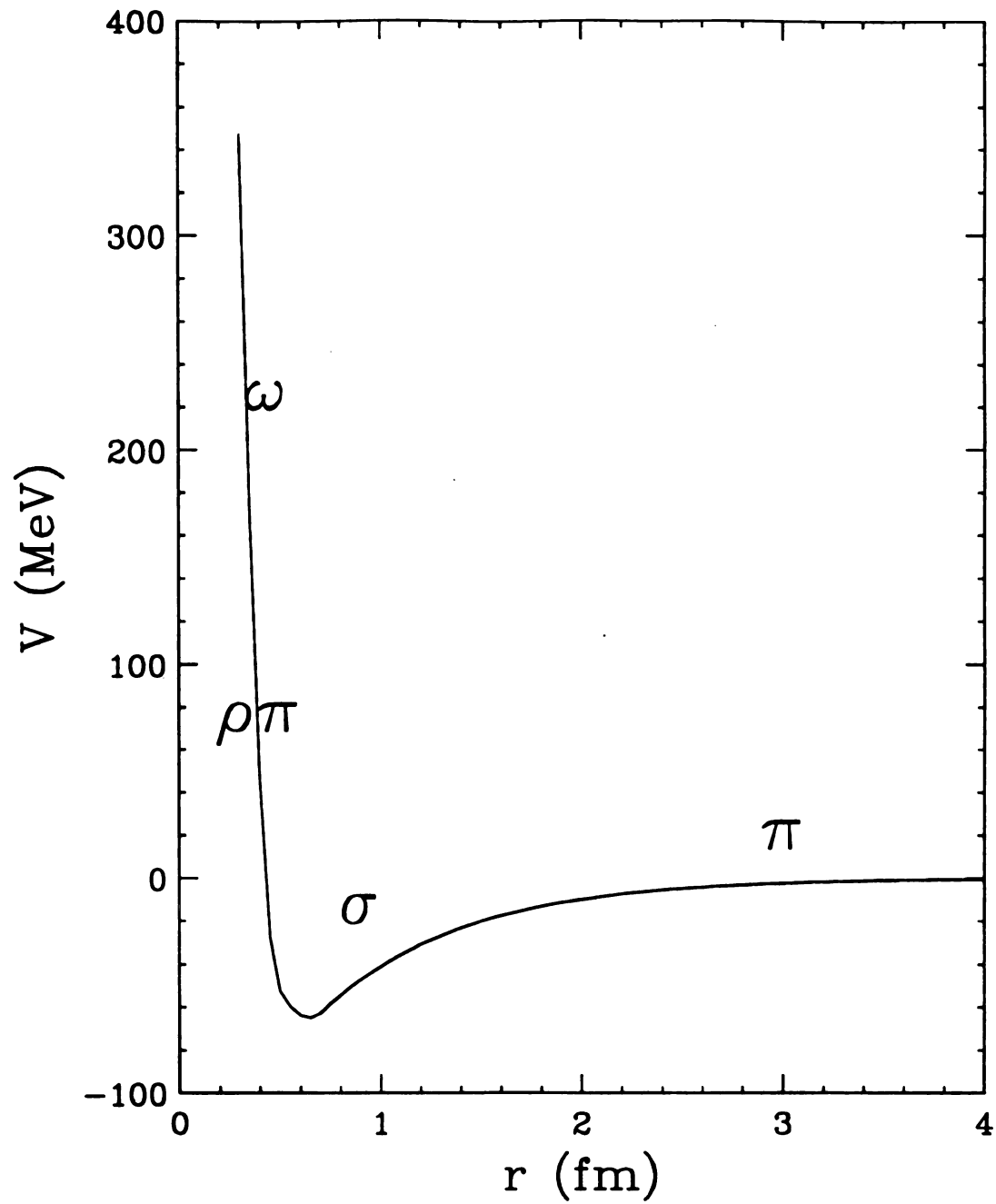


Figure 6.1: Schematic diagram of the nuclear potential with the possible mediating mesons shown in their region of dominance [Mac86].

short-range repulsive force. This particle is a $3\text{-}\pi$ resonant state with a mass of 783 MeV. It is also a spin one (vector) boson, and it can be shown from field theoretical calculations that vector bosons lead to a strong repulsive central force as well as a spin-orbit force [Mac86]. Thus, two observed particles can “fit the bill” for mediating the shortest- and longest-range parts of the nuclear force. However, the intermediate-range force is still a mystery.

Several models, including the two-pion-exchange model (TPE) [Tak51], the one-boson-exchange model (OBE) [Hos61, Gre67] and the σ model [Sch57, Pol58, Pol58, Gel60], were proposed in the 1950’s and 1960’s, to explain the intermediate-range attractive force. All of these models rely on a two-pion exchange, however the latter two assume it is a scalar meson, $2\text{-}\pi$ -S-wave resonance rather than two uncorrelated pions. This mediating particle was called the σ , and it was assumed to have a mass between 400 and 800 MeV. It was hoped that the ϵ resonance, which was observed in this mass range, was the σ particle. However, although the ϵ was listed in the particle data tables until 1976 [PDG74, PDG76], its width was too large (several hundred MeV) to consider it an elementary particle, and so it was removed from the tables. The confirmation of the existence of the σ particle has not yet been found from results of elementary reactions. Perhaps heavy-ion reactions can provide more information on the existence of the σ particle.

It has been suggested that the pion dispersion relation is modified in nuclear matter [Ber87, Cha91, Her92, Sch88]. This modification leads to a change in the effective mass of the pion and possibly other mesons as well. Thus, by measuring pions produced in nuclear reactions, where this medium effect may be observable, the existence of the σ particle can be studied from a new direction. Since the effect is dependent upon the density of the nuclear matter in which the σ is formed, a comparison between light and heavy nuclear systems should show the effects of

the effective mass modifications. The observable which shows greatest promise for detecting the σ particle is the $\pi^+\pi^-$ correlation function. Since this proposed scalar meson is expected to be a 2π -S-wave resonance, if it exists, it should show up as an enhancement in the 2-pion correlation function, just as the ${}^2\text{He}$ resonance does in the 2-proton correlation function. The experimental search for this particle using nuclei must be performed at relativistic beam energies, since single-pion production is possible only if a nucleon-nucleon collision has at least 130 MeV available in the center of mass.

To study this possibility, the DIOGENE collaboration measured the 2-pion correlation function for 1.6 GeV p + C and 1.6 GeV p + Pb collisions [Plu92]. They constructed the $\pi^+\pi^-$ invariant-mass correlation function as:

$$R_{\pi^+\pi^-}(M_{inv}) = \frac{\Pi_2(\pi^+\pi^-)}{\Pi_1(\pi^+)\Pi_1(\pi^-)}, \quad (6.1)$$

where Π_2 is the probability of observing a pair of pions in a single event, and Π_1 is the probability of observing a single pion. They observed an enhancement in the correlation function at $M_{inv}(\pi^+\pi^-) \approx 2M_\pi$ in p + Pb collisions, however for the carbon target, there is no observed enhancement. Did they observe the σ particle, at last?

When studying the evolution of the reaction zone, experimental measurements are forced to look at average properties of reaction zone, since there is no microscopic way to determine the exact impact parameter and reaction-plane orientation. In proton observables, such as the correlation function, this uncertainty in determination of impact parameter and source size leads to difficulties in describing the source of the protons (see Section 5.3). In the case of pion observables, the uncertainties involved with reaction-plane orientation and impact-parameter determination are even more confounding. Since pions can be absorbed and rescattered once they are produced,

the pions which are finally observed by the detection systems are not necessarily the particles which are produced in the earliest stages of the reaction. However, two-pion correlation functions can provide a great deal of insight into these effects.

The BUU hadronic transport model described in chapter 3 can be used to study the one- and two-particle observables in these relativistic heavy-ion collisions. While pion production is included in the model, the σ particle is not. Thus, if this enhancement of the 2-pion correlation function can be reproduced by the BUU model, it is most likely due to some less exotic mechanism than the production of σ particles in nuclear matter.

6.1 Pion Production

Previous studies have shown that the predictions for single-particle observables, such as pion kinetic energy spectra and flow, agree reasonably well with the experimental data [Li91a, Li91b]. For example, in studying pion collective flow, it was shown that absorption and re-scattering of pions in asymmetric nucleus-nucleus collisions at $E/A \approx 1$ GeV can account for the observed collective pion flow [Li91a, Li93]. The pion production and absorption processes included in BUU are:

$$N + N \leftrightarrow N + \Delta \leftrightarrow N + N + \pi. \quad (6.2)$$

Through this process, pions are absorbed and rescattered in the spectator matter and, in non-central collisions they are focussed into one hemisphere. In Figure 6.2 this effect is demonstrated by showing a superposition of 50 non-central p + Pb collisions. The trajectories of pions (thin dots) and resonances (thick dots) are projected onto the reaction plane. For those tracks which scatter toward the center of the target nucleus, most of these pions and resonances rescatter. Eventually all of the resonances decay and most of the pions are absorbed. However, the pions and resonances which scatter

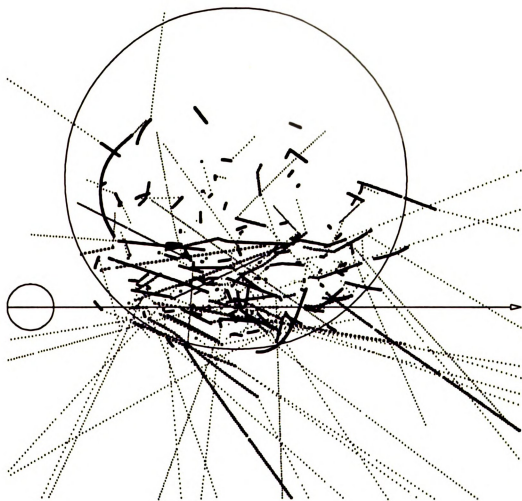


Figure 6.2: Superposition of pion and delta-resonance trajectories (thin-dots and thick-dots respectively) projected onto the reaction plane for 50 1.6 GeV p + Pb events at $b = 5\text{fm}$.

away from the center of the target eventually escape, and thus the majority of pions are emitted away from the center of the nucleus. Similar scenarios have been proposed by the WA-80 collaboration to explain observed angular correlations of pion pairs for $p + \text{Au}$ collisions at beam energies of 4.9, 60 and 200 GeV [Sch92].

Production of pion pairs with opposite signs is not an easy task for a proton-nucleus collision. Figure 6.3, shows the number of charged pions per event as a function of impact parameter predicted by BUU for two targets. Even for the most central collisions, fewer than 50% of the events produce any charged pions, and much fewer produce a pair of pions. This is due to several conditions. First, since a large amount of energy is needed to produce pions and there is only one incoming nucleon, two hard collisions with enough energy to produce pions is unusual. In addition, these two pions must then try to escape the cold spectator matter around them as they traverse the nucleus without being reabsorbed.

In addition, for both the light and heavy targets, there are many more positive pions than negative. This is due to the isospin of the projectile. Since the projectile is a proton, there will be more energetic proton-nucleon collisions than neutron-neutron collisions. From isospin considerations, there will be more positive pions produced than negative. This can be understood by looking at the pion production mechanisms. The following reactions are all possible:

$$p + n \rightarrow \begin{cases} \Delta^+ + n \rightarrow n + n + \pi^+ \\ \Delta^+ + n \rightarrow n + n + \pi^0 \\ \Delta^0 + p \rightarrow n + n + \pi^+ \\ \Delta^0 + p \rightarrow n + p + \pi^0 \\ \Delta^0 + p \rightarrow p + p + \pi^- \end{cases} \quad (6.3)$$

$$p + p \rightarrow \begin{cases} \Delta^{++} + n \rightarrow p + n + \pi^+ \\ \Delta^+ + p \rightarrow n + p + \pi^+ \\ \Delta^+ + p \rightarrow p + p + \pi^0 \end{cases} \quad (6.4)$$

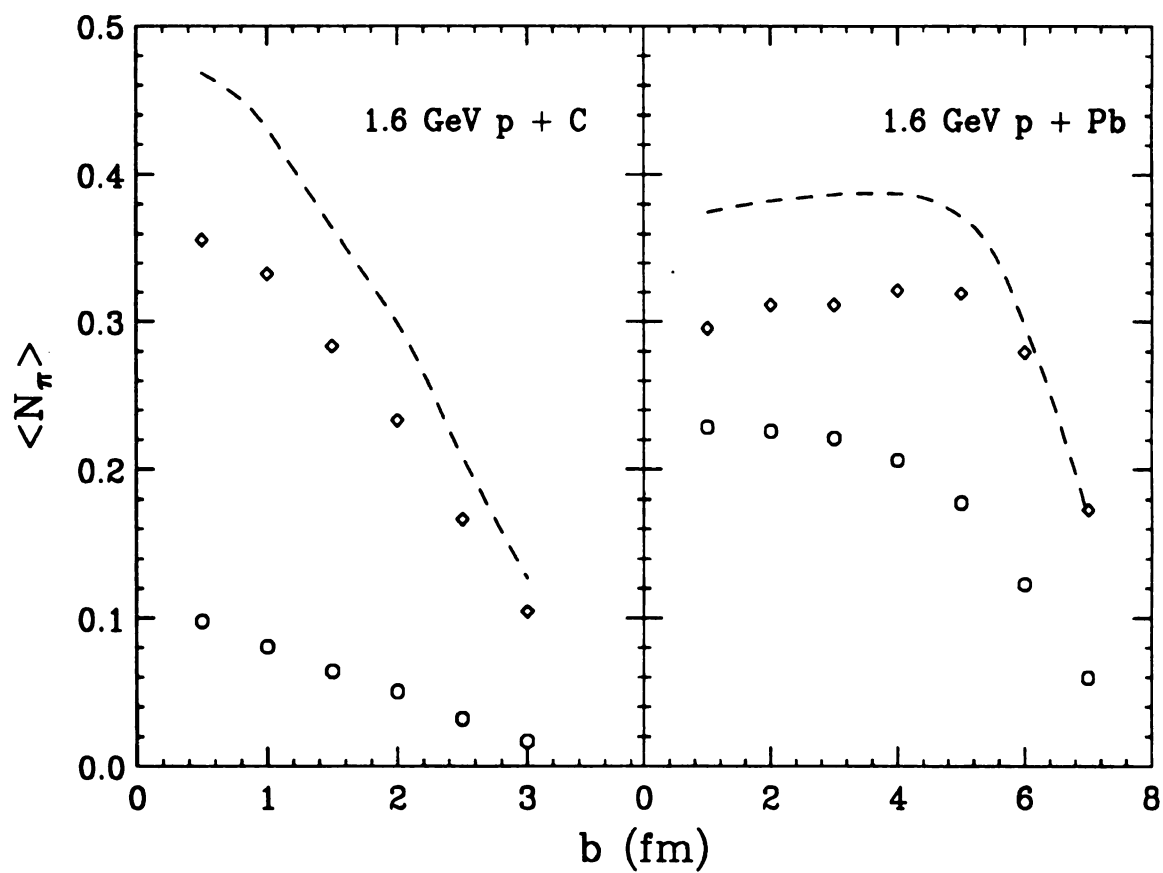


Figure 6.3: Average number of charged pions per event for 1.6 GeV p + C & Pb collisions. The diamonds represent positive pions, the circles, negative pions and the line represents the total number of charged pions.

While the total cross section for π^+ production in the np channel is equal that for π^- [Wol90], the additional pp channels allows for more positive pions to be produced. Thus, not only are there very few negative pion events (less than 10% for the carbon target and 25% for the lead), there are even fewer $\pi^+\pi^-$ events. At the beam energy of 1.6 GeV, the BUU model predictions indicate that two pions are produced in less than 5% of the events, and fewer still produce $\pi^+\pi^-$ pairs.

6.2 Calculation of the Correlation Function

As in the identical particle correlation functions discussed in chapter 5, the measured correlation function for $\pi^+\pi^-$ pairs is simply the ratio of the number of oppositely-charged pion pairs produced in the same event to the number of oppositely-charged pairs produced in different events. Due to the limited number of $\pi^+\pi^-$ pairs produced in the proton-induced reactions studied, the calculations were performed by taking the ratio of pion pairs produced in events with the same reaction plane and impact parameter to pion pairs produced in events with different reaction planes and impact parameters. This is possible in the theoretical calculations due to the ability to know precisely both the impact parameter and the reaction plane.

In addition, one other physical constraint must be taken into account. In two-pion events, the pions emitted first (π_1) have more kinetic energy available than the pions which are produced second (π_2). Pion kinetic energy spectra for three different classes of pions are shown in Figure 6.4. As seen in the figure, the kinetic energy spectrum for pions from single-pion events (represented by the histogram) extends to energies above 800 MeV. Also, the kinetic energy spectrum for pions which are emitted first in two-pion events (represented by diamonds) extends to higher energies than the spectrum for those which are produced second (represented by circles). Thus, in

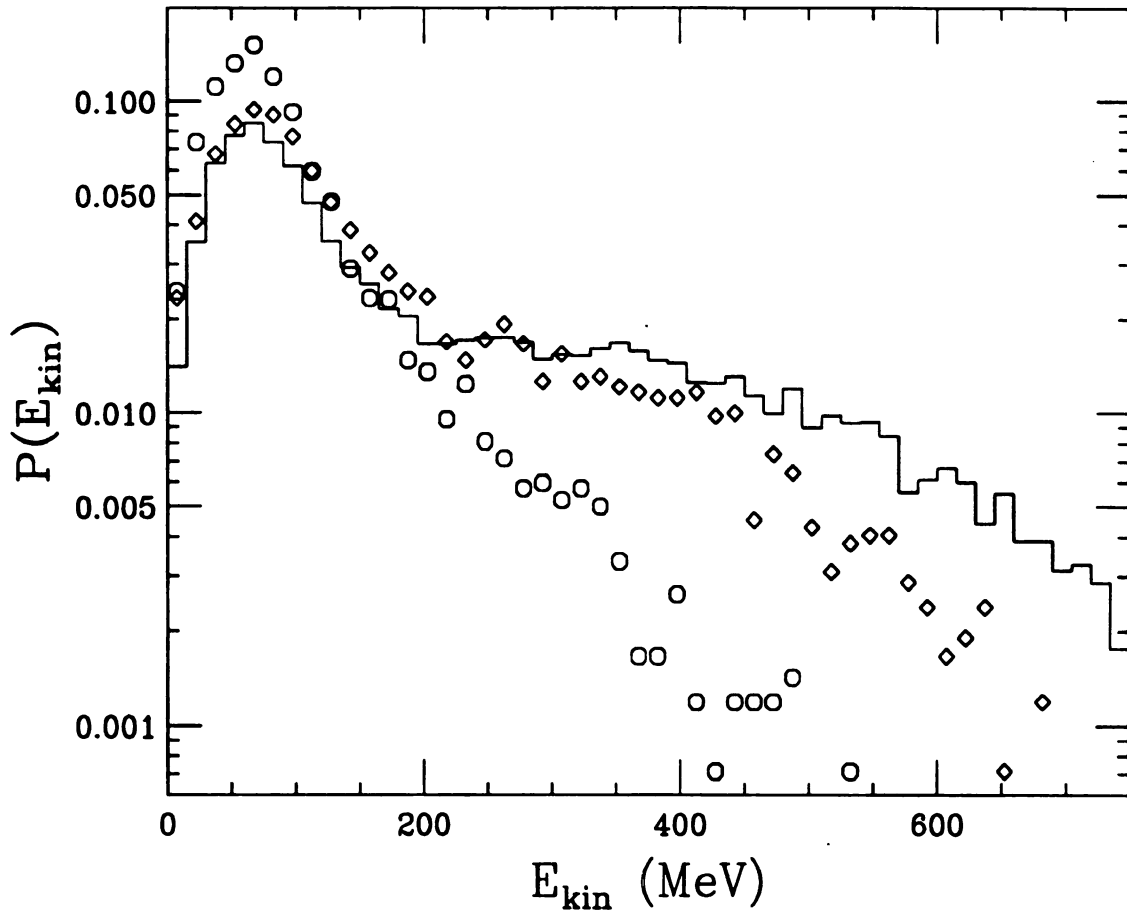


Figure 6.4: Pion kinetic energy spectra for pions emitted in 1.6 GeV p + Pb collisions with impact parameter $b=5\text{fm}$ predicted using the transport model. The solid line represents pions produced in single pion events, the symbols represent pions produced in multi-pion events (diamonds for pions emitted first and circles for second).

order to increase statistics in the numerator, but retain the kinematic constraints while mixing over all events, all possible $\pi_1^\pm \pi_2^\mp$ pairs ($N(M_{inv})$) are constructed from pions created in two-pion events with the same impact parameter and reaction plane.

6.3 Comparison with Experiment

In order to generate background events in a manner corresponding to the experimentally observed background, all possible $\pi^+ \pi^-$ pairs ($N(M_{inv,\phi})$) are constructed with random reaction plane orientation and from any impact parameter. The correlation function is then given by:

$$R_{\pi^+ \pi^-}(M_{inv}) = \frac{\int db w(b) N(M_{inv}, b)}{\int db_1 db_2 w(b_1, b_2) N(M_{inv,\phi}, b_1, b_2)}, \quad (6.5)$$

where the weighting functions ($w(b), w(b_1, b_2)$) take into account the number of real pairs relative to the number of pairs used in the calculations. In Figure 6.5, the calculated correlation functions for the reactions 1.6 GeV p + C and 1.6 GeV p + Pb are shown together with the experimental results. The theoretical curves have been normalized such that $R_{\pi^+ \pi^-}(0.5 \text{ GeV}) = 1.0$, and the pions used in the calculation have been filtered to account for geometrical and energy cuts of the DIOGENE detector. For both targets, the theoretical results reproduce the trends of the measured results. No enhancement is seen in the carbon system. However, for the lead system there is an enhancement at $M_{inv}(\pi^+ \pi^-) = 2M_\pi$, which is also predicted by the BUU calculations, however, the measured enhancement is slightly higher than the calculated result. The different shapes for the carbon and lead target is due primarily to the mean absorption length of a pion, which is much shorter than the size of the lead nucleus but comparable to the size of the carbon nucleus. This leads to a focussing of the emitted pions to one side of the reaction plane for a heavy nucleus, as can be seen in figure 6.1. This focussing effect creates more true pairs with low invariant-mass,

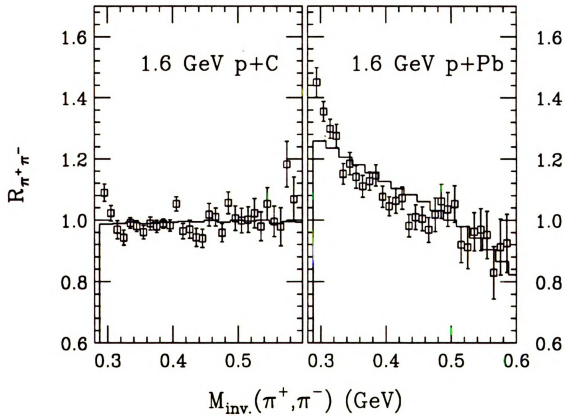


Figure 6.5: Two pion correlation function for 1.6 GeV p + C and Pb as a function of the invariant-mass of the $\pi^+\pi^-$ pair. The squares represent the experimental data [Plu92] and the histograms represent the BUU transport model calculations.

while the background pairs (due to randomization of the reaction plane) show no such focussing effect and therefore have no bias toward low mass pairs.

To show how this focussing affects the correlation function, the calculated correlation function for impact parameters of 2, 4 and 6 fm are shown for the lead target, and impact parameters of 1, 2 and 3 fm are shown for the carbon target in Figure 6.6. Both the filtered and unfiltered results are shown. For the most central case, the unfiltered lead and carbon results look similar: both are flat, because the focussing is insignificant at this impact parameter. As the impact parameter increases, the lead results begin to develop a slightly negative slope while the carbon results remain flat. The filtered results are even more dramatic. This is mainly due the high-momentum cuts. Experimentally, positive pions with momenta above 500 MeV/c cannot be distinguished from protons, therefore a similar momentum cut for both positive and negative pions was employed. This serves only to enhance the effect of the focussing by not counting pairs where one pion is very energetic, thus reducing the number of detected high invariant-mass pairs.

Similar effects due to nuclear shadowing are also observed in the identical particle correlation function. The identical-pion correlation function calculated using the Koonin formalism described in chapter 5 has also been calculated using event mixing as in the $\pi^+\pi^-$ correlation function study described above. The relative wave function for two like signed pions, $\phi_{\pi\pi}$, is the symmetrized Coulomb wave function, ϕ_c , given by [Bau93]:

$$|\phi_{\pi\pi}(\vec{q}, \vec{r})|^2 = \frac{1}{2} |\phi_c(\vec{q}, \vec{r}) + \phi_c(\vec{q}, -\vec{r})|^2, \quad (6.6)$$

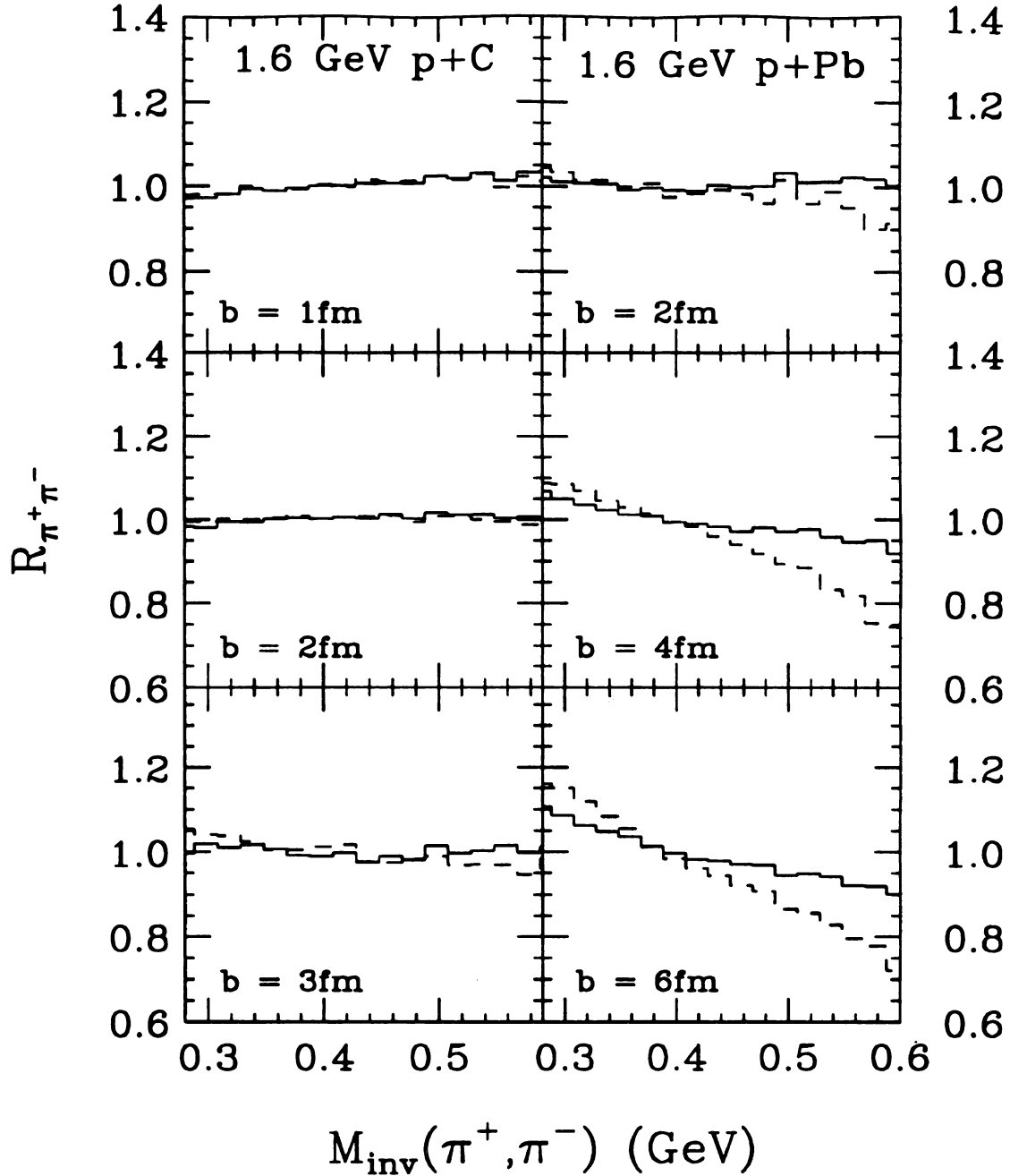


Figure 6.6: Two pion correlation function for 1.6 GeV p + C (left) and Pb (right) as a function of the invariant-mass of the $\pi^+\pi^-$ pair for specific impact parameters. The top row contains results for the most central cases while the bottom row contains results the most peripheral. The solid histograms represent the predictions of the BUU model while the dashed histograms represent the predictions of the BUU model after applying a filter to simulate the geometric and kinematic acceptance of the DIOGENE detector.

where the Coulomb scattering wave function is defined in terms of the confluent hypergeometric series (${}_1F_1$):

$$\phi_c(\vec{q}, \vec{r}) = \exp(-\frac{1}{2}\pi\eta)\Gamma(1+i\eta)\exp(iqz){}_1F_1(-i\eta|1|iq(r-z)), \quad (6.7)$$

and $\eta = \alpha Z_1 Z_2 m_r / q$. This wave function is shown in Figure 6.7 for a relative angle between \vec{q} and \vec{r} of 60° . Unlike the proton wave function, the symmetrized Coulomb wave function has no resonance structure, however, the Coulomb repulsion still causes the wave function to be zero for $q = r = 0$.

The $\pi^+\pi^+$ correlation functions for both the carbon and lead targets calculated using the BUU phase-space distributions are shown in Figure 6.8. In this case, the correlation function is expressed in terms of the invariant mass (as was the $\pi^+\pi^-$ correlation function). The invariant mass can be related to q through:

$$M_{inv}^2 = 4m_\pi^2 + 4q^2. \quad (6.8)$$

Also, for historical reasons, the Gamow corrected correlation function is shown. This formalism was introduced to facilitate comparison of measured pion correlation functions with Gaussian source parameterizations. In the case of pion correlations, Gyulassy, *et al* [Gyu79] showed that the relative wave function could be factorized into a symmetrized plane-wave (ϕ_{plane}) times the Gamow penetration factor, thus reducing equation 5.3 to:

$$C(\vec{P}, \vec{q}) = |\phi_{\pi\pi}(\vec{q}, 0)|^2 \int d^3r F_{\vec{P}}(\vec{r}) |\phi_{plane}\vec{q}, \vec{r})|^2. \quad (6.9)$$

This factorization is valid when the Bohr radius is much larger than the size of the emitting source. For pions the Bohr radius is ≈ 390 fm which is much larger than any source which would be created in these proton included reactions. The Gamow-corrected correlation function ($C_G(\vec{P}, \vec{q})$) is then just the full correlation function

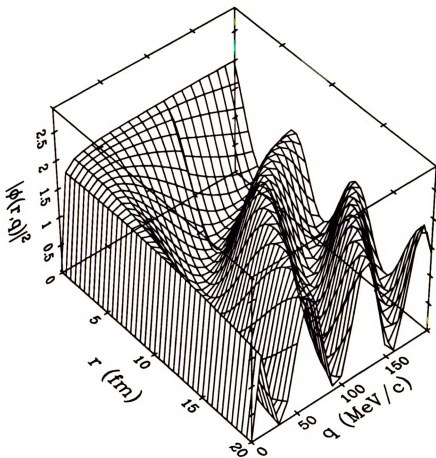


Figure 6.7: The two-pion relative wave function, $|\phi(q, r, \cos(\theta))|^2$, for fixed angle $\theta = 60^\circ$ as a function of relative position and momentum [Bau93].

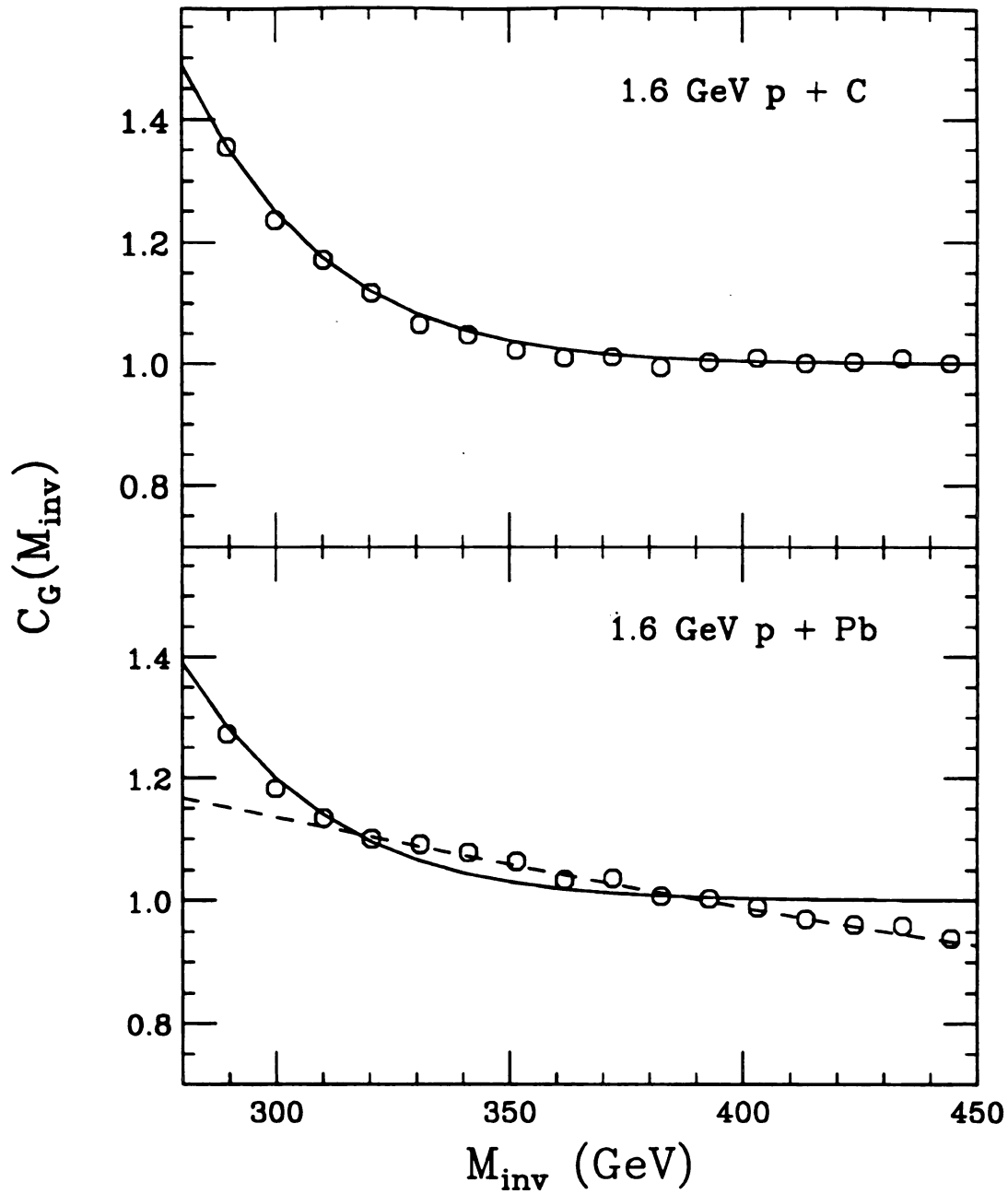


Figure 6.8: The $\pi^+\pi^+$ correlation functions for 1.6 GeV p + C (left), and 1.6 GeV p + Pb (right). The symbols represent the calculations using the Koonin formalism with phase space predictions of BUU. The lines represent fits using Gaussian source parameterizations with radius parameters 1.5 fm (solid) and 0.5 fm (dashed).

divided by the Gamow factor. In this form, the dominant feature of the correlation function is an enhancement at $q = 0$ due to the bosonic nature of the pions, as shown in the figure.

As in the $\pi^+\pi^-$ correlation function, the $\pi^+\pi^+$ correlation function also has a non-zero slope for high invariant mass for proton on lead collisions, while the results for proton on carbon collisions is flat for high invariant mass. The solid lines in Figure 6.8 represent fits to the calculated correlation functions using the zero-lifetime Gaussian source parameterization:

$$C_G(q) = 1 + \lambda \exp\left(\frac{-q^2 R^2}{2}\right). \quad (6.10)$$

The correlation function for the carbon target can be well fit by a single Gaussian source with $\lambda \approx 0.5$ and $R \approx 1.5$ fm (solid lines). This radius reflects the size of the cylindrical cut through the carbon target by the proton. In the lead system, a similar parameterization, $\lambda \approx 0.4$ and $R \approx 1.5$ fm, provides reasonable agreement with the correlation function for $M_{inv} \leq 400$ GeV, where the value of the correlation function is greater than one. This is shown in the figure as a solid line. However, for $M_{inv} > 400$ GeV, the nuclear shadowing effects begin to dominate. Thus, no simple fit will work due to the continuously decreasing correlation function for high invariant-mass. If a Gaussian source fit is used to describe the high invariant mass part of the correlation function (the dashed line in Figure 6.8), values of $\lambda \approx 0.6$ and $R \approx 0.5$ fm are obtained, with an overall normalization factor of 0.73 for the Gaussian source parameterization. This fit, however, does not reproduce the low invariant-mass part of the correlation function. The small source size, as well as the fact that the value of correlation function is less than one indicates that the simple Gaussian parameterizations are not valid in this case.

Direct comparison with experimental observations is not possible at the present time due to the lack of data in this energy region for proton-nucleus collisions. However, the WA-80 Collaboration has observed similar results in collisions of 200 GeV protons on various targets [Kam92]. Since these beam energies are beyond the scope of the current transport model calculation, additional experimental measurements with ≈ 1 GeV protons are necessary for direct comparison. However, this study does show that pion correlation functions calculated using the single-particle phase space predictions of BUU, can be used to study pion production in heavy-ion collisions. Valuable information on the behavior of pions in nuclear matter and the effects of pion rescattering and reabsorption on the correlation function have been obtained. In addition, detector cuts are shown to play an important part in the shape of the correlation function. However, the current correlation calculations show that the observed signal does not confirm the existence of the σ particle.

Future experiments plan to use correlation techniques to search for the formation of the quark-gluon plasma in ultra-relativistic heavy-ion collisions. However, if these studies are to provide useful information, continued work at relativistic energies is necessary to better understand the behavior of hadronic matter formed during heavy-ion collisions. While waiting for the new ultra-relativistic heavy-ion colliders to come on line, much more work can proceed in currently accessible energy regimes.

Chapter 7

Conclusions

The behavior of nuclear systems under extreme conditions has been studied using the BUU hadronic transport model. This single-particle model for heavy-ion collisions has been shown to be in agreement with single-particle observables, such as kinetic energy spectra of protons, photons and pions. In Part I, it has also been shown to provide useful information which is necessary to study fragment production in intermediate-energy heavy-ion collisions. The formation of intermediate mass fragments cannot be studied directly in the current BUU formalism. However, the hybrid model presented in Chapter 4 does provide useful information on possible mechanisms for the evolution of the reaction zone. Previous studies assuming the surface or volume emission of fragments from spherical sources at normal nuclear matter density failed to reproduce experimental observations. The current study shows that more information on the dynamics of the system (for example, expansion) must be included.

However, this formalism is qualitative at best. It can only be used to show that the global properties, such as total number of intermediate mass fragments produced in a collision, are in the correct range when compared to experiment. A complete model which takes into account the full dynamics of the collision as well as the formation of composite particles does not yet exist. This next generation of models will also be needed to analyze more complicated variables which can be experimen-

tally observed at intermediate bombarding energies, for example, fragment-fragment correlation functions.

Additional evidence concerning the expansion and evolution of the reaction zone formed in heavy-ion collisions is obtained from the two-proton correlation function. Using the Koonin-formalism, the single-particle phase space distributions predicted by BUU can be used to calculate the two-proton correlation function for heavy-ion reactions. Previous work has shown that this method does provide useful information on the evolution of the reaction zone. The current study has shown that impact-parameter-selected events are also in agreement with calculated correlation functions. The correlation function is sensitive to the in-medium nucleon-nucleon cross section and previous studies have shown best agreement is obtained with values close to the free value. However, the correlation function is not sensitive to the equation of state of nuclear matter at these beam energies. Studies are already underway to study two-proton correlation functions at beam energies around 1 GeV/nucleon, where the compressional effects of the nuclear equation of state should be observable through correlation measurements.

At these relativistic energies, pion production introduces one more class of observables that can be used to study the reaction zone. Since these particles are created during the collision, they should reflect the collision process itself, and not any residual memory of the incoming particles. However, their behavior in the nuclear matter they must traverse in order to be observed must be understood as well. Due to their reabsorption and rescattering during the heavy-ion collision, the impact-parameter-averaged correlation function may show unexpected results. Since hadron correlation functions are expected to play a significant role in studying the possible formation of a quark-gluon plasma in ultrarelativistic heavy-ion collisions, these medium effects must be understood before definitive statements can be made at higher energies.

Thus, a systematic study of pion correlations function at relativistic energies for a variety of heavy-ion systems should be made. The experimental measurements have already been performed. Data should be available in the next year for comparison with detailed transport-model calculations, such as those discussed in this work.

Part II

Equilibrium Model of Heavy Ion Collisions

Chapter 8

Introduction

As discussed in Part I, it is possible to study the nuclear equation of state using heavy-ion collisions by observing the effects of compression, expansion and cooling on the nuclear system formed during the collision. However, in relativistic heavy-ion collisions (RHIC) at energies around 15 GeV/nucleon, the energy and matter densities reached during the initial compression stage are expected to be many times greater than that of normal nuclear matter. If this occurs, it may be possible to observe a new type of phase transition, from a phase where quarks and gluons are confined to baryons and mesons to a phase where they are free to move at large spatial separations. This deconfined phase is referred to as a quark-gluon plasma (qgp).

The qgp has been discussed for many years. However, the only particles which can be experimentally observed are the conventional color-singlet bound states of quarks and gluons, or the hadrons which are actually formed after the qgp converts to a hadronic phase. How the formation of a qgp in the early stages of the reaction might affect the final observed particles has been predicted by several groups. The goal of these studies has been to determine the differences in the observed particle production in a hadronic versus qgp scenario. One proposed signal of the qgp is an increase in strange particle production [Raf82, Egg91, Han91]. This enhancement is due to the fact that less energy is needed to produce strange quark pairs in a

quark-gluon plasma than strange hadrons in a hadronic gas. In the plasma stage, the minimum center-of-mass energy, \sqrt{S} needed to create an $s\bar{s}$ pair is just the rest mass of the strange quarks ($\sqrt{S_{s\bar{s}}} \approx 2M_s \approx 300$ MeV). In a hadronic environment $\sqrt{S_{min}}$ for a collision of two particles to result in the production of strange particles is in the ΛK channel where ≈ 0.7 GeV is necessary to produce the strange meson and baryon. In the purely mesonic channel, ≈ 1 GeV is necessary to produce a $K\bar{K}$ pair.

Since strange particle production is energetically more favorable in a qgp than a hadronic gas, it was suggested that the ratio of strange particle production to non-strange particle production (or K/π ratio) would provide insight into whether a plasma had been formed in the early stages of a nuclear collision [Koc86, Mat86a, Mat86b, Bar88]. The predictions were that this ratio would be larger if a qgp was formed in the early phases of a collision than if the reaction proceeded via purely hadronic mechanisms.

Experimentally, a similar comparison was sought. However, there is no direct method by which to look at two systems with identical initial conditions and just “turn off” or “turn on” the qgp phase of the reaction, as is possible in model simulations. Instead, what is measured is the K/π ratio for various systems. By comparing the ratio for $p + A$ collisions, where it is unlikely that the energy density reached in the collision is sufficient to form a qgp, with the results from $A + A'$ collisions, an increase in the ratio would be seen as a signal of plasma formation. Experiments have, in fact, measured pion and kaon spectra in central 14.6 A GeV Si + Au collisions at the Alternating Gradient Synchrotron (AGS) at Brookhaven National Laboratory (BNL). The E802 collaboration observed that the K/π ratios at mid-rapidity are substantially greater than those measured in $p+A$ reactions [Mia90, Tan88].

However, this enhancement may not be due to the formation of a quark-gluon plasma. Detailed studies of hadronic gases need to be done. Perhaps this increase

could be due to differences in the systematics of $p+A$ and $A+A'$ collisions. To study this possibility, several thermal models of hadronic gases were introduced, including fireball models [Lee88, Cle90], expanding fireball models [Bro91, Ko90, Ko91, Xia89, Ko89, Ko88, Fri89], multi-component firestreak models [Cha91] and Landau fireball models [Sta90, Sta89]. Several hadronic transport model calculations have also been applied to the problem of strangeness production in high-energy heavy-ion collisions [Mat89, Cha90, Gyu90, Ame91]. These transport models are quite successful in reproducing the experimental data [Mat89, Wer89a, Wer89b, Sor89], but have to rely on elementary interaction cross sections between the constituents (baryons and mesons or partons or quarks and gluons) of their models, which are unknown in some cases.

Rather than relying on model calculations to provide input to a transport model, a thermal model is used here. In particular, the nuclear firestreak model (NFS) [Gos78, Mye78]. While the original model calculations successfully predicted the shape of pion, nucleon and light fragment spectra for relativistic heavy-ion collisions with beam energies between 0.4 - 2.1 A GeV, it over predicted the absolute normalization of the pions. However, once partial transparency of the target nucleus was taken into account, this over-prediction was accounted for [Dan81].

At beam energies around 2.1 A GeV, strange particle production is possible. This has been addressed in the firestreak model by Gudima and Toneev [Gud85]. By taking into account the associative nature of strange particle production, prediction of pion, nucleon and light fragment spectra was possible. Once again, the absolute normalization of the pions was over predicted. These calculations did not include the possibility of the target nucleus being partially transparent to the projectile nucleus. A complete treatment of transparency would have reduced the absolute normalization.

Experimental data collected at AGS indicate close to full stopping of the heavy ions in 15 A GeV heavy-ion collisions [Abb87, Bra88, Tan88]. Thus, the assumption

Table 8.1: Baryons and mesons used in the nuclear firestreak model.

Baryons		Mesons	
Non-strange	Strange	Non-strange	Strange
p	Λ	π	$\phi(1020)$
n	Σ	η	$h_1(1170)$
Δ	Ξ	$\rho(770)$	$b_1(1235)$
		$\omega(783)$	$a_1(1260)$
		$\eta'(958)$	$f_2(1270)$
		$f_0(975)$	$f_1(1285)$
		$a_0(980)$	$\eta(1295)$
			K
			$K^*(892)$
			$K_1(1270)$

of thermal equilibration needed for the model is not unreasonable at these energies. At the beam energies available at the AGS, a firestreak model which includes effects of incomplete stopping and particle production is necessary. In fact, it is necessary to include the possible production of all mesons and strange baryons with masses below 1.3 GeV. In the following chapters, a modified nuclear firestreak model which takes into account incomplete stopping, and includes all particles listed in Table 8.1, will be described.

Chapter 9

The Model

The major assumption of the nuclear firestreak model [Gos78, Mye78] is that chemical and thermal equilibrium is attained in the reaction zone of a heavy-ion collision. In fact, these assumptions are also true in the nuclear fireball model [Wes76, Gos77, Kap77, Mek77]. The difference between the two models is that the collision zone is divided into parallel streaks containing a mixture of light fragments, mesons and baryons in the firestreak model (see Figure 9.1). Each streak is then treated as a gas using a multicomponent grand canonical ensemble formalism, and thus the temperature and chemical potentials of the various types of particles are introduced. These are determined iteratively by conserving the average energy, charge, baryon number and strangeness of the streak.

9.1 Conserved Quantities in the Streaks

By assuming the reaction zone initially consists of nucleons uniformly distributed over the spheres representing the target and projectile, the initial values of the energy, charge, baryon number and strangeness of the streak can be determined using geometrical considerations. Given that only the overlap region is of interest, only streaks that contain nucleons from both the projectile and target are used. Thus, the

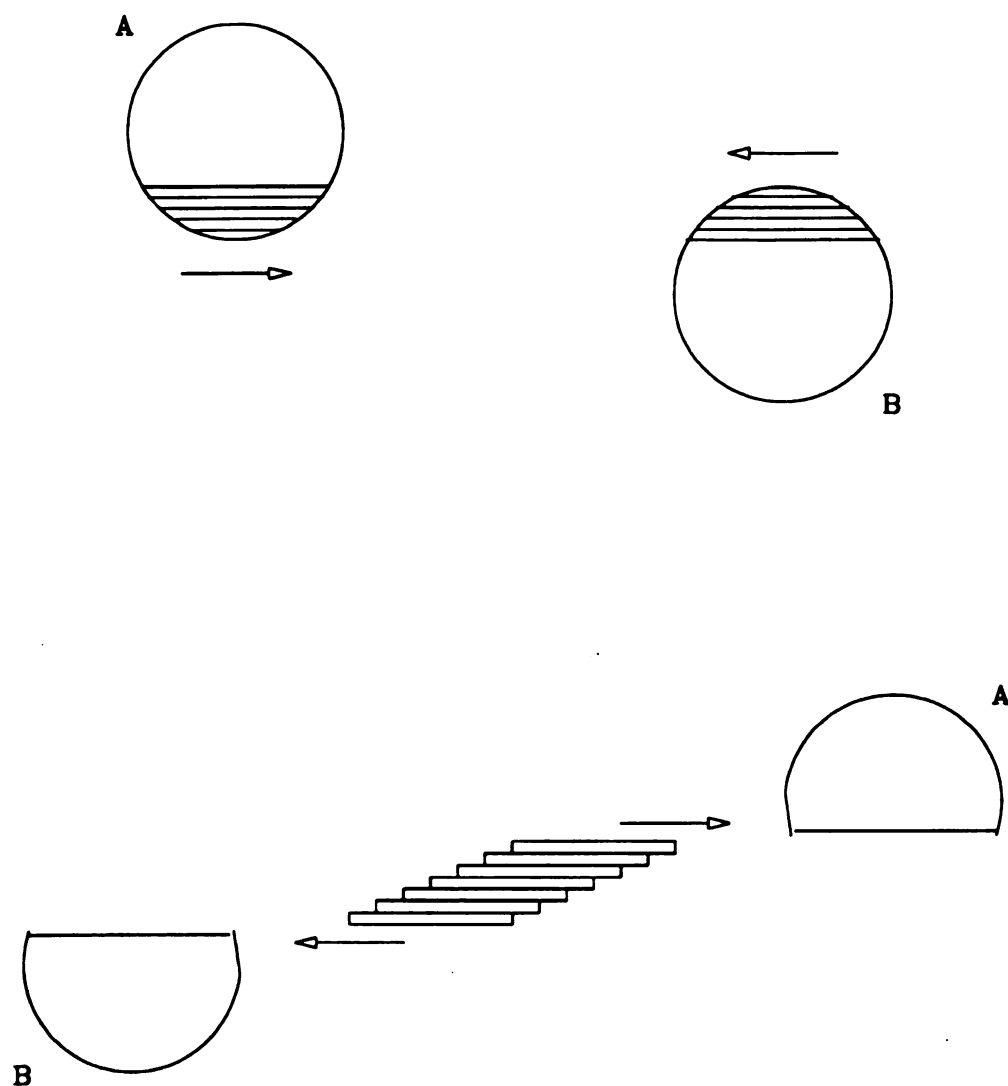


Figure 9.1: Schematic drawing of a collision in the firestreak model in the center of mass frame. The top shows the orientation of nucleus A approaching nucleus B. The bottom figure shows the streaks in the reaction zone as well as the remnants of the original nuclei.

projectile fraction,

$$\eta = \frac{N_p}{N_p + N_t}, \quad (9.1)$$

where N_p and N_t are the number of projectile and target nucleons in the streak, must lie between 0 and 1. N is determined geometrically. For example, the number of nucleons in a streak containing the center of the nucleus is given by:

$$N = \rho(2R\sigma_\eta) = 0.378A^{1/3}\sigma_\eta \text{ fm}^2, \quad (9.2)$$

where the radius of the nucleus is given by $R = 1.12A^{1/3}$ fm, ρ is the density of the nucleus and σ_η is the cross sectional area of the streak.

The conserved quantity which is most easily determined is the strangeness of the streak. Since the streaks are initially composed of nucleons, the strangeness (S) of each streak must be zero. The baryon number is found by:

$$B = N_p + N_t, \quad (9.3)$$

using equation 9.2. In a similar manner, the charge of the streak can be determined from:

$$\frac{Q}{B} = Z_p \frac{N_p}{A_p} + Z_t \frac{N_t}{A_t} = \eta \frac{Z_p}{A_p} + (1 - \eta) \frac{Z_t}{A_t}, \quad (9.4)$$

where A and Z are the atomic number and charge of the respective nuclei.

If complete stopping is assumed, similar methods can be used to determine the energy of the streak. All of the the kinetic energy of the streak is converted to thermal energy through successive nucleon-nucleon collisions, if complete stopping occurs. However, some nucleons are not completely stopped in the center of mass frame and thus they retain some of their kinetic energy. In order to determine the

thermal energy of the streak, the fraction of momentum retained by a nucleon (the transparency) is needed.

When a nucleon experiences two-body collisions, most of its kinetic energy is converted into thermal energy. The average number of nucleon-nucleon collisions a projectile nucleon experiences while traversing the target nucleus is [Bau88]:

$$\overline{N}(b) = 2\lambda_P \sigma_{NN} \frac{\int_O dx dy \int dz_1 dz_2 \rho_p(x, y + b, z_1) \rho_t(x, y, z_2)}{\int_O dx dy \int dz (\rho_p(x, y + b, z) + \rho_t(x, y, z))}, \quad (9.5)$$

where σ_{NN} is the energy-averaged total nucleon-nucleon cross section. In practice, the value of $\sigma_{NN} = 40\text{mb}$ was used for the calculations at $E = 15 \text{ A GeV}$. The xy integration extends over the geometrical overlap O of the two nuclei perpendicular to the beam direction. The factor λ_P is due to Pauli blocking in the final-state phase space of the scattered nucleons. By approximating the initial momentum distributions as Fermi spheres and assuming isotropic angular distribution of the scattering cross section, the fraction of the phase space into which scattering is allowed is:

$$\lambda_P = \left(1 - \frac{2p_f^3 - \frac{1}{2}k^2(3p_f - k)}{(p_f + p_b)^3} \right)^2, \quad (9.6)$$

where p_f is the Fermi momentum of normal nuclear matter, p_b is the beam momentum per nucleon and

$$k = (p_f - p_b)\theta(p_f - p_b). \quad (9.7)$$

For the energies considered here, k is always zero and equation 9.6 reduces to:

$$\lambda_P = \left(1 - \frac{2p_f^3}{(p_f + p_b)^3} \right)^2. \quad (9.8)$$

Using Poisson statistics, probability that a nucleon from one nucleus will traverse the other nucleus without suffering any collisions is:

$$\mathcal{T}(b) = \exp(-\overline{N}(b)). \quad (9.9)$$

Thus, in the center of mass frame, the fraction of the momentum which is not available for thermalization is:

$$p_i = \pm N_i T(b) p_{cm}. \quad (9.10)$$

The projectile and target streaks each retain this center of mass momentum which, when is converted to a lab momentum, so that a lab kinetic energy for the center of mass of each streak can be determined. The remainder of the initial lab kinetic energy is assumed to be converted to thermal energy and divided equally among the nucleons in the streak.

9.2 Restrictions of Chemical Equilibrium

Since the model assumes each streak is in chemical equilibrium, the chemical potentials can all be related to a linear combination of three chemical potentials. When a streak is in chemical equilibrium, reactions such as:



are as likely to occur as their reverse processes. Then

$$\mu_p + \mu_{\pi^-} = \mu_n. \quad (9.12)$$

For neutral pions, one equilibrium reaction is



therefore,

$$\mu_{\pi^0} = 0. \quad (9.14)$$

In fact, for all nonstrange meson types, M, similar equilibrium conditions apply, yielding:

$$\mu_p \pm \mu_{M^\mp} = \mu_n \quad (9.15)$$

and

$$\mu_{M^0} = 0. \quad (9.16)$$

The strange mesons and baryons are dealt with in a similar way. The kaons, for example, must be in equilibrium in the following reactions:

$$p + p \leftrightarrow K^0 + K^+ + p + n \quad (9.17)$$

and

$$p + n \leftrightarrow \bar{K}^0 + K^0 + p + n. \quad (9.18)$$

These lead to

$$\mu_{K^0} = -\mu_{\bar{K}^0} \quad (9.19)$$

and

$$\mu_{K^\pm} = \pm(\mu_p - \mu_n + \mu_{\bar{K}^0}). \quad (9.20)$$

In this manner, all chemical potentials can be expressed in terms of the neutron, proton and \bar{K}^0 chemical potentials.

9.3 Boundary Conditions

In the rest frame of the streak, the initial charge, strangeness, baryon number and energy determined from geometrical considerations must be conserved when the system is in thermal and chemical equilibrium. In a grand canonical ensemble, the momentum distribution for particles with spin S_j , energy E_j and chemical potential μ_j , in a streak of volume V and temperature T_s is:

$$f_j(\vec{p}, \eta, b) = E_j \frac{d^3 N_j}{dp^3} = E_j \frac{(2S_j + 1)V}{(2\pi)^3} \frac{1}{\exp\left(\frac{E_j - \mu_j}{T_s}\right) (\pm 1)}, \quad (9.21)$$

where the $+/-$ signs stand for fermions/bosons, respectively. Integrating this yields:

$$N_j = \frac{(2S_j + 1)Vm_j^2 T_s}{2\pi^2} \sum_{n=1}^{\infty} \frac{(\mp)^{n+1}}{n} \exp\left(\frac{n\mu_j}{T_s}\right) K_2\left(\frac{nm_j}{T_s}\right) \quad (9.22)$$

and

$$\begin{aligned} N_j E_j &= \frac{(2S_j + 1)Vm_j^3 T_s}{2\pi^2} \sum_{n=1}^{\infty} \frac{(\mp)^{n+1}}{n} \exp\left(\frac{n\mu_j}{T_s}\right) \\ &\times \left(K_1\left(\frac{nm_j}{T_s}\right) + \left(\frac{3T_s}{nm_j}\right) K_2\left(\frac{nm_j}{T_s}\right) \right), \end{aligned} \quad (9.23)$$

in the rest frame of the streak, where K_i , ($i = 1, 2$) is the i^{th} -order modified Bessel function of the second kind. In the thermal model, the energy, charge, strangeness and baryon number densities of the streak are then:

$$\begin{aligned} e &= \sum_i \frac{N_i E_i}{V}, \\ q &= \sum_i \frac{N_i Q_i}{V}, \\ s &= \sum_i \frac{N_i S_i}{V}, \\ b &= \sum_i \frac{N_i B_i}{V}. \end{aligned} \quad (9.24)$$

These are related to the quantities defined in section 9.1 through:

$$\begin{aligned} e &= E/V, \\ q &= Q/V, \\ b &= B/V, \\ s &= 0. \end{aligned} \quad (9.25)$$

These equations, when combined with the chemical potential relations determined in the previous section, reduce the number of unknown thermal quantities to five:

neutron, proton and \bar{K}^0 chemical potentials, temperature, and streak volume. Conservation of energy, charge, strangeness and baryon number will fix four of these values. By adding the constraint that the hadron density must equal the freezeout density, which is the density at which equilibrium ceases, the last quantity is fixed through:

$$h = \sum_i \frac{N_i H_i}{V} = \rho_c. \quad (9.26)$$

The quantities T_s , μ_p , μ_n , $\mu_{\bar{K}^0}$ and V are found by minimizing the function:

$$\chi(T_s, \mu_p, \mu_n, \mu_{\bar{K}^0}) = \left(\frac{h}{\rho_c} - 1 \right)^2 + \left(\frac{e/b}{E/B} - 1 \right)^2 + \left(\frac{q/b}{Q/B} - 1 \right)^2 + \left(\frac{s}{b} \right)^2. \quad (9.27)$$

Once a thermodynamic description for the streak is known, the invariant cross section for the emitted particles is given by:

$$F_j(\vec{p}) = \sum_{\eta=0}^1 \int 2\pi b db Y(b, \eta) J_{p' \rightarrow p}(\beta(\eta)) f_j(\vec{p}, \eta, b), \quad (9.28)$$

where $J_{p' \rightarrow p}(\beta(\eta))$ is the Jacobian which transforms from the rest frame of the fire-streak with center of mass velocity β , to the frame of interest. The value of the projectile fraction will range from 0 ($\beta(\eta) = \beta_t$), where there are only target nucleons in the streak, to 1 ($\beta(\eta) = \beta_p$), where there are only projectile nucleons in the streak. f_j is the invariant momentum distribution of a particle of type j and momentum \vec{p} , produced in a streak with energy E , and projectile fraction η . For particles produced in the streak, f_j is given by equation 9.22. For particles which are products of the decay of resonances created in the streak,

$$f_j(\vec{p}, \eta, b) = \sum_R \frac{W_D(2S_R + 1)V m_R T_s^2}{(2\pi)^3 p p_D} \left[\frac{\mu_R}{T_s} \ln \left(\frac{1 + e^{x_-}}{1 + e^{x_+}} \right) + \sum_{n=1}^{\infty} \frac{(\mp)^{n+1}}{n^2} \left(e^{-nx_-} (nx_- + 1) - e^{-nx_+} (nx_+ + 1) \right) \right], \quad (9.29)$$

where

$$x_{\pm} = \frac{m_R}{m_j^2 T_s} (E E_D \pm p p_D) - \frac{\mu_R}{T_s}. \quad (9.30)$$

W_D is the branching ratio for the decay of a resonance of type R into a particle of type j . The energy and momentum of the decay product in the rest frame of the resonance are E_D and p_D , respectively. The yield function $Y(b, \eta)$ is given by:

$$Y(b, \eta) = \int_{\eta - \frac{1}{2}\delta\eta}^{\eta + \frac{1}{2}\delta\eta} d\eta' \int dx dy dz \delta(\eta' - \eta_b(x, y)) [\rho_p(x, y + b, z) + \rho_t(x, y, z)], \quad (9.31)$$

where $\rho(r)$ is the diffuse radial density distribution [Mye78]

$$\rho(r) = \begin{cases} \rho_o \left[1 - \left(1 + \frac{R}{a} \right) \exp\left(-\frac{R}{a} \frac{\sinh(r/a)}{r/a}\right) \right], & r \leq R \\ \rho_o \left[\frac{R}{a} \cosh\left(\frac{R}{a}\right) - \sinh\left(\frac{R}{a}\right) \right] \frac{\exp(-r/a)}{r/a}, & r \geq R \end{cases} \quad (9.32)$$

with R and a given by $1.2A^{1/3}$ and $\sqrt{\frac{1}{2}}$, respectively.

In the original model f_j was independent of b , allowing equation 9.29 to be rewritten as:

$$F_j(\vec{p})|_{orig} = \sum_{\eta=0}^1 Y_{\eta} J_{p' \rightarrow p}(\beta(\eta)) f_j(\vec{p}, \eta), \quad (9.33)$$

where Y_{η} is the impact parameter integrated yield function

$$Y_{\eta} = \int 2\pi b db Y(b, \eta). \quad (9.34)$$

In the present model, equation 9.29 is solved numerically, using equations 9.22, 9.30 and 9.31. The temperature, volume, and chemical potentials are found by minimizing equation 9.27. The result is the prediction of the triple-differential invariant cross sections for the particle species considered.

9.4 Particle Production in the Model

Experimental measurements have shown the K/π ratios increase with the mass of the colliding system [Abb91]. In addition, the ratio of positive mesons is always higher than the ratio of negative mesons. While the first observation may be explained within the framework of a quark-gluon plasma, it may be possible to explain both trends by looking into the production of particles in the NFS model.

In models that assume chemical equilibrium, the chemical potential of a particle is equal and opposite to the chemical potential of its anti-particle. In addition, the yield of particles with positive chemical potentials is larger than for negative chemical potential particles. In practice, the NFS model predicts that positive kaons will always have positive chemical potentials. For this reason, the K^- (which is the anti-particle of the K^+) will always have a negative chemical potential, and thus a lower yield than the K^+ . Why is this?

The non-zero chemical potential is due to the different production mechanisms for particles and anti-particles. If strange mesons were only produced in pairs (eg. K^+K^- , $K^+\bar{K}^0$, $K^0\bar{K}^0$), then $\mu_{K^+} = 0$. However, there are also associative production processes. For the mesons with strangeness +1 (for example positive kaons), there are processes involving hyperons of strangeness -1 and -2 . For example:

$$p + p \leftrightarrow \begin{cases} K^+ + \Lambda + p \\ K^0 + \Sigma^+ + p \\ K^+ + K^+ + \Xi^- + p \end{cases} . \quad (9.35)$$

Because the energy required for strangeness production through the $K\Lambda$ channel is less than that required for $K\bar{K}$ ($\sqrt{s} \approx 0.7$ GeV and 1 GeV, respectively) the associative process for positive kaons occurs more frequently than the pair production process. In addition, associative production of mesons of strangeness -1 involves anti-baryons.

For the negative kaon,

$$\bar{p} + n \leftrightarrow K^- + \bar{\Lambda} + n \quad (9.36)$$

is a possible process. However, this reaction has a threshold of $\sqrt{s} \approx 2.5$ GeV, thus it occurs much less frequently than the previously-mentioned process. In fact, since the chemical potential of a nucleon is on the order of the mass of a nucleon, the chemical potential of its anti-particle is ≈ -1 GeV. This leads to a suppression in the anti-baryon cross sections of about 2 orders of magnitude, so particles with positive strangeness are more abundant than their anti-particles and $\mu_{K^+} > 0$.

If full stopping is assumed, the temperature and chemical potentials in the streaks depend only on the N/Z of the system, and the beam energy per nucleon. For $N=Z$ nuclei, in central 14.6 A GeV symmetric collisions, $T_s = 127.4$ MeV, $\mu_{\pi^+} = -0.3$ MeV and $\mu_{K^+} = 46.5$ MeV. The pion chemical potential is non-zero due to the difference in the neutron and proton masses. If $N > Z$, as in Au + Au collisions, the temperature is unchanged, however, μ_{π^+} and μ_{K^+} both decrease. This leads to $\pi^+/\pi^- < 1$. Similarly, in p+p reactions, $N < Z$, thus $\mu_{\pi^+} > 0$ and $\pi^+/\pi^- > 1$. While the assumption of equilibrium in such a small system is unrealistic, the comparison is made to show the isospin effect. Direct comparison to data would be unwise.

As in the case of kaon production, this can be explained by looking at the possible reaction channels available for pion production through both n+n and p+p collisions. The contributions of the following reactions are the most significant in pion

production:

$$\begin{aligned}
 n + n &\leftrightarrow \left\{ \begin{array}{l} \pi^- + n + p \\ \pi^0 + n + n \\ \pi^- + \Delta^0 + p \\ \pi^- + \Delta^+ + n \\ \pi^0 + \Delta^0 + n \\ \pi^0 + \Delta^- + p \\ \pi^+ + \Delta^- + n \end{array} \right. & p + p &\leftrightarrow \left\{ \begin{array}{l} \pi^+ + n + p \\ \pi^0 + p + p \\ \pi^+ + \Delta^0 + p \\ \pi^+ + \Delta^+ + n \\ \pi^0 + \Delta^+ + p \\ \pi^0 + \Delta^{++} + n \\ \pi^- + \Delta^{++} + n \end{array} \right. \quad (9.37)
 \end{aligned}$$

There are three times as many direct production mechanisms for π^- as π^+ in neutron collisions. The opposite is true for proton reactions. In Table 9.1, the yields of charged kaons and pions are shown for several central 14.6 A GeV symmetric collisions. For all of these reactions, $\approx 60\%$ of the pions are produced in direct reactions and in fact, $\pi^-/\pi^+ > 3$ in neutron and proton systems, respectively, where in larger systems, $\pi^+/ \pi^- \approx 1$. The Δ resonances in the reactions listed above subsequently decay into pions and nucleons. Their contribution is also listed in Table 9.1. There are heavier mesons which can also be produced through similar reactions. Many of these mesons also decay into pions. It should be stressed at this point that the $p + p$ and $n + n$ reactions in Table 9.1 do not deliver results for the K/π ratios which could be compared to experimental data. This is because these very small systems with baryon number = 2 are very far from chemical equilibrium which is assumed in a fireball model. They are only included here to illustrate the isospin effect.

When transparency is taken into consideration, the temperature and chemical potential are no longer independent of A. For light nuclei, like helium, the nucleons retain 20% of their center of mass momentum. While the transparency has little effect on the pion chemical potential, it does affect both the temperature and kaon chemical potential. While the temperature increases by 0.9% from d + d reactions to Si + Si, the kaon chemical potential decreases by 9.4%, as can be seen in Figure 9.2.

Table 9.1: Probability per nucleon in a streak for producing charged pions and kaons in central A+A ($\eta = 0.5$) collisions at 14.6 A GeV/c. The % yields for direct and decay production are also included.

	n+n	p+p	He+He	Au+Au
K^+	.112	.145	.151	.158
% thermal	87.20	90.77	88.44	87.87
% K res	9.38	6.59	8.19	8.55
% ϕ	3.42	2.64	3.37	3.58
K^-	.063	.049	.072	.082
% thermal	87.50	83.20	85.06	85.32
% K res	6.37	8.96	7.89	7.79
% ϕ	6.13	7.84	7.05	6.89
π^+	.493	.868	.769	.787
% thermal	63.03	68.36	66.08	65.78
% Δ	12.67	15.04	12.26	11.32
% ρ	14.36	10.96	13.55	14.20
% other	9.94	5.64	8.12	8.69
π^-	.872	.494	.772	.866
% thermal	68.39	63.08	66.12	66.84
% Δ	15.06	12.69	12.27	11.69
% ρ	10.94	14.33	13.53	13.58
% other	5.62	9.90	8.08	7.90
K^+/K^-	1.79	2.96	2.09	1.93
π^+/π^-	.565	1.76	.996	.908
K^+/π^+ (%)	22.7	16.7	19.6	20.1
K^-/π^- (%)	7.17	9.89	9.36	9.46

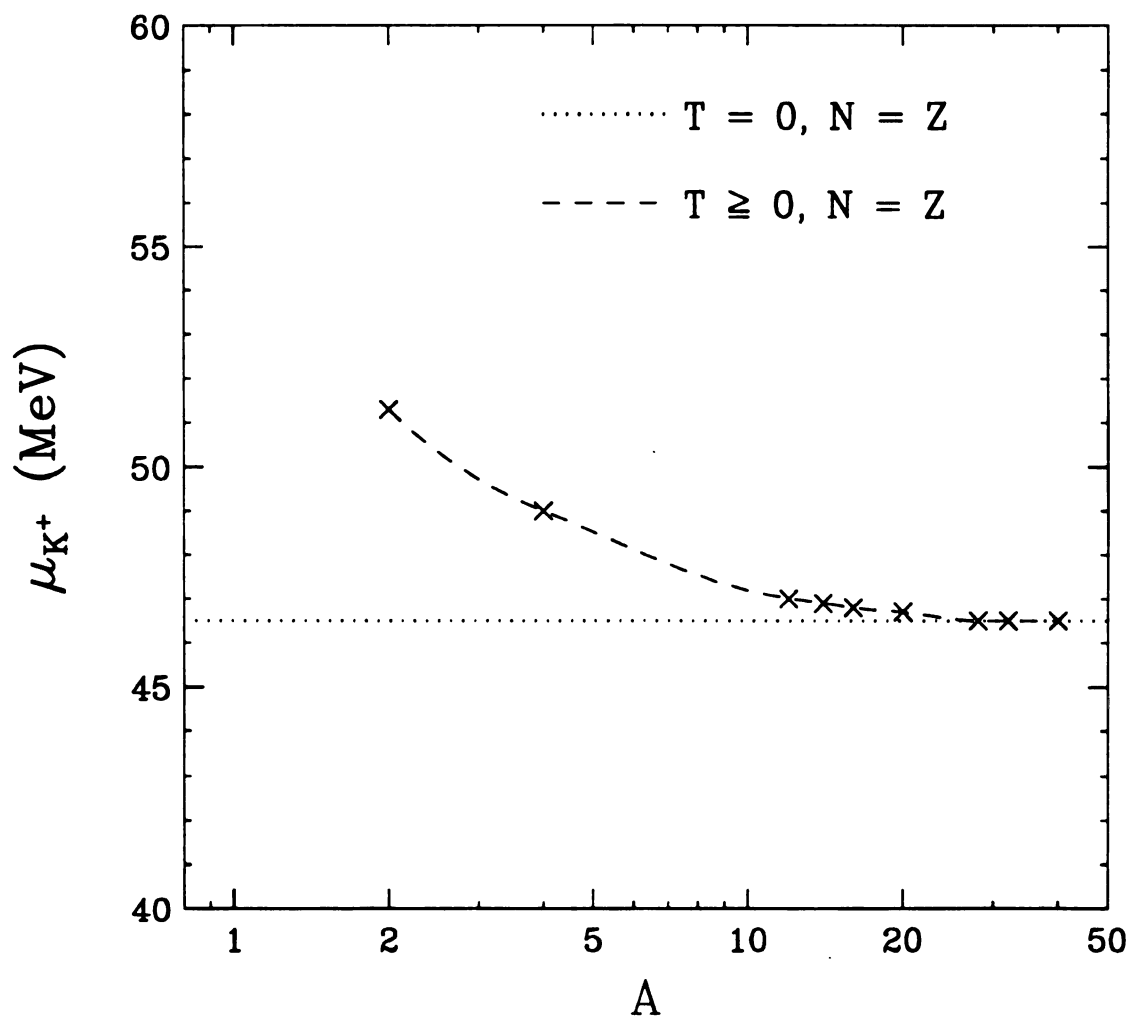


Figure 9.2: Chemical potential for K^+ in MeV for central $A + A$ collisions at 14.6 A GeV/c. The crosses represent the values calculated using the NFS model. The dotted line is the value obtained by the program when complete stopping is assumed.

Chapter 10

Comparison With Experiment

Data from experiments at AGS are available for Si projectiles on Al and Au targets at beam energies of 14.6 A GeV. In these data, central collisions were selected. In the calculations presented here, collisions with impact parameters less than 2 fm are considered central. The data are presented in two forms, the invariant cross section in the lab frame as a function of transverse mass and the rapidity distribution.

In Figure 10.1 and Figure 10.2, the invariant cross sections of p, π and K at mid-rapidity calculated by the firestreak model are compared to those measured by the E-802 collaboration [Mos91, Cos90]. A nucleon-nucleon cross section of 40 mb was used for the transparency calculation. In the Si+Au system, this resulted in complete stopping of the projectile. In the lighter Si+Al system, the projectile was completely stopped for exactly central collisions, but only partially stopped for $b \neq 0$.

The pion spectra agree reasonably well with the data. A slight overprediction is observed in this model (the spectra are renormalized by a global factor of 0.5). A similar effect is also observed in other model calculations [Ko]. A freezeout density equal to that of normal nuclear matter has been used in these calculations. Decreasing the density below this value has the effect of increasing the slope of the spectra slightly. The model predicts the transverse mass distributions of the kaons and pions

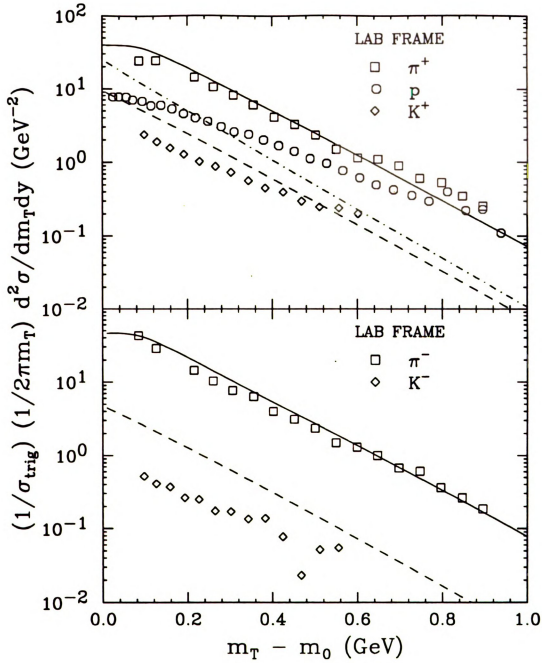


Figure 10.1: Invariant cross sections of p , π^\pm and K^\pm from 14.6 A GeV Si+Au collisions for $1.2 \leq y \leq 1.4$. The data are taken from reference [Mos91]. The lines represent the results of the calculations with the modified firebreak model for p (dashed), π (solid) and K (dot-dashed).

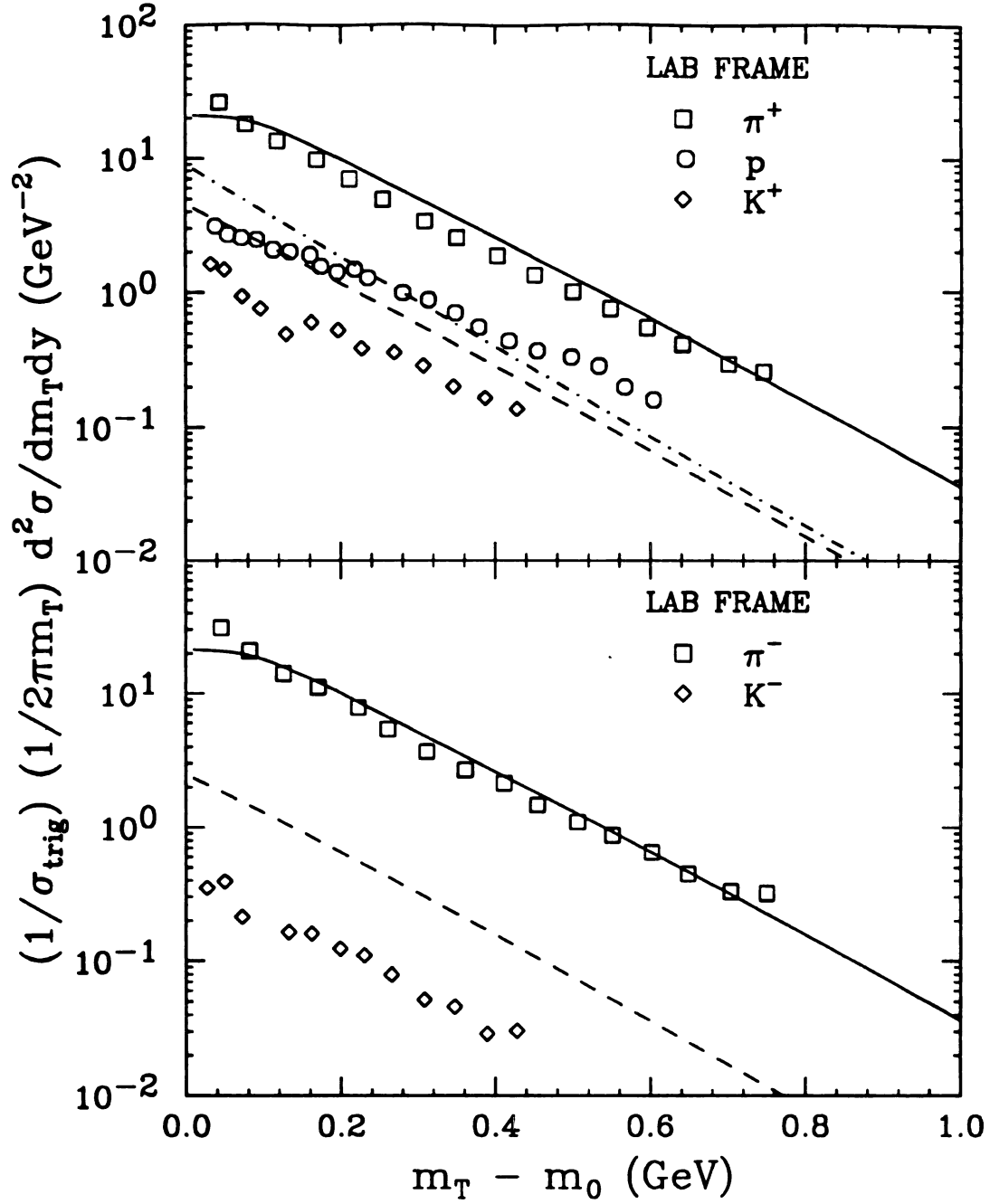


Figure 10.2: Invariant cross section of p , π^\pm and K^\pm from 14.6 A GeV Si+Al collisions for $y = 1.5$. The data are taken from reference [Cos90]. The lines represent the results of the calculations with the modified firestreak model for p (dashed), π (solid) and K (dot-dashed).

to have almost the same slope. This model cannot reproduce the slope of the proton spectra. While increasing the freezeout density would decrease the slope of the various spectra, the slope of the pion spectrum never exceeds that of the proton as it does experimentally. This disagreement could be attributed to the possible occurrence to collective baryon flow, which is not an ingredient of the model.

The kaon yield is also seen to consistently overpredict the data. This overprediction is because the assumption of chemical equilibrium is only partially fulfilled. The amount by which the data is overpredicted is a measure for how far the heavy-ion collisions actually are from chemical equilibrium. One can, of course, obtain much better agreement with the data by introducing a kaon freeze-out density which is independent of the pion freeze-out density. In this way the relative normalization of kaon and pion spectra can be adjusted. This additional fit parameter was not introduced because it is not the main purpose of this work to fit data, but to work out systematic effects in the K/π ratios as a function of the mass of the projectile and target.

By integrating the invariant cross sections over transverse mass, the rapidity distributions

$$\frac{dN}{dy} = \frac{1}{\sigma_0} \frac{d\sigma}{dy} \quad (10.1)$$

are found. In Figure 10.3, these are compared to rapidity distributions extracted from experimental data where an exponential fit to the transverse mass spectra is assumed and then integrated [Abb91]. For the model results,

$$\sigma_0 = A_p \sigma_{trig} = 28 \left(\pi b_{max}^2 \right). \quad (10.2)$$

The K/π ratios at central rapidity are summarized in Table 10.1 for p+A and Si+Au collisions. Both the experimental and model calculations produce K^+/π^+ ratios which

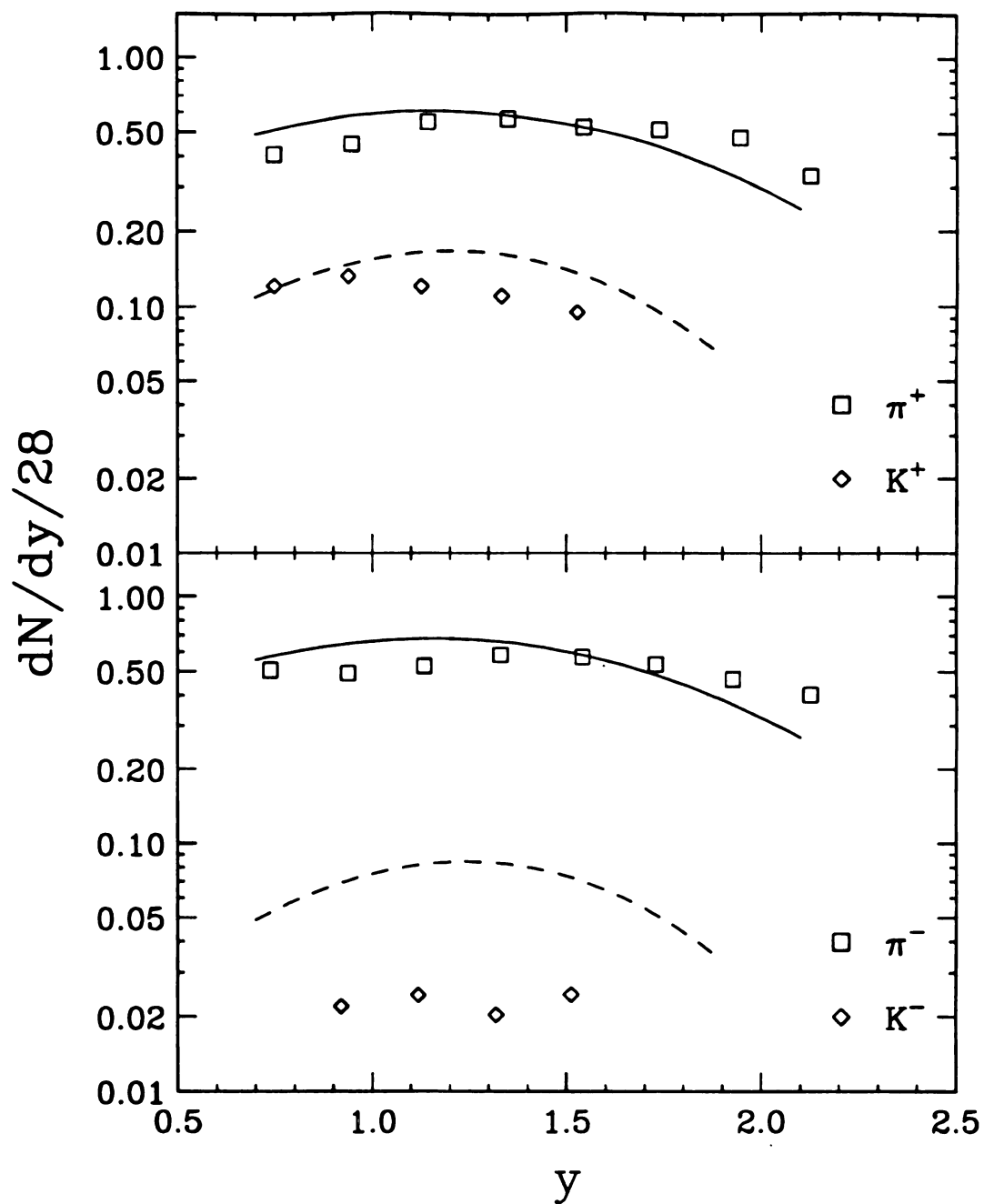


Figure 10.3: Rapidity distributions per projectile nucleon (28) for π^\pm and K^\pm produced in central 14.6 A GeV Si+Au collisions. The data are taken from reference [Mia90]. The lines represent the results of the calculations with the modified firestreak model for π (solid) and K (dashed).

Table 10.1: K/π ratios for central A on B collisions at 14.6 A GeV/c.

		p+Be	p+Au	central Si+Au
K^+/π^+	NFS	14.7	12.5	26.3
	expt	7.8	12.5	18.2
K^-/π^-	NFS	6.7	3.9	12.5
	expt	2.0	2.8	3.2

exceed the K^-/π^- ratios as expected from the isospin considerations mentioned in section 9.4. However, the model predictions exceed the experimental values by as much as a factor of 3.9 at this rapidity for the negative mesons.

Chapter 11

Conclusions

The NFS model has been modified to calculate the production cross section of strange mesons and baryons. This is done by inclusion of all strange and nonstrange mesons and baryons with masses of up to 1.3 GeV into the formalism. A formalism to calculate geometric transparency and partial stopping has also been provided in this framework.

This model can be used to predict available pion spectra at AGS energies ($E \approx 15$ A GeV). Complete stopping is predicted for Si projectiles and heavy targets, such as Au, but for light targets, such as Al, complete stopping occurs only for very central collisions.

Since this model is purely thermal, it predicts the same temperature for all emitted particles, and is of course not able to reproduce the experimental observation that the apparent temperatures of emitted pions, kaons and protons are different.

In this model, more than half (60 – 80%) of the produced pions and kaons are of thermal origin, and only a small contribution is due to resonance decays.

The kaon yields are systematically overpredicted for all reactions considered. This is a good indication that kaons are not in chemical equilibrium in the experiments performed at AGS, as also suggested in reference [Ber89]. This can be attributed to

the relatively small interaction cross sections of strange mesons in hadronic matter which cause long mean free paths for kaons and make approaches based on chemical equilibrium somewhat questionable.

However, this model is able to reproduce the experimental findings that the K/π ratio is systematically higher (up to a factor of 5 in the experimental data) for the positively charged mesons than for the negatively charged ones. The systematic increase of the K/π ratios from $p+A$ to $A+A$ systems, which is found in experiment is also reproduced. In this model, however, this dependence of the K/π ratio on the mass (baryon number) of the system is basically due to the fact that more energy per nucleon is available in the fireball generated in the collision of a symmetric (or almost symmetric) heavy-ion system than in a proton-induced reaction at the same beam energy per nucleon. In addition, a small isospin effect is found: $n+n$ collisions have a higher K^+/π^+ ratio than $p+p$ collisions, and in heavier systems $n+n$ collisions become increasingly more probable.

It is therefore possible to conclude that an increase in the K^+/π^+ ratio with the total mass of the heavy-ion system can be caused by purely hadronic effects. An interpretation of the high K^+/π^+ ratio as a possible signal for the creation of a quark-gluon plasma then appears to be questionable.

Bibliography

- [Aic85] J. Aichelin and G. Bertsch, Phys. Rev. **C31**, 1730 (1985).
- [Abb87] T. Abbott, Y. Akiba, D. Alburger, D. Beavis, R. R. Betts, M. A. Bloomer, P. D. Bond, C. Chasman, Y. Y. Chu, B. A. Cole, J. B. Costales, H. Crawford, J. B. Cumming, R. Debbe, E. Duek, H. A. Enge, J. Engelage, S. Y. Fung, D. Greiner, L. Grodzins, S. Gushue, H. Hamagaki, O. Hansen, P. Haustein, S. Hayashi, S. Homma, H. N. Huang, Y. Ikeda, S. Katcoff, S. Kaufman, R. J. Ledoux, M. J. Le Vine, P. Lindstrom, M. A. J. Mariscotti, Y. Miake, R. Morse, S. Nagamiya, J. Olness, C. Parsons, L. P. Remsberg, M. Sarabura, A. Shor, S. G. Steadman, G. S. F. Stephens, T. Sugitate, A. W. Sunyar, M. Tanaka, M. J. Tannenbaum, M. Torikoshi, J. H. Van Dijk, F. Videbaek, P. Vincent, E. Vulgaris, V. Vutsadakis, W. A. Watson III, H. E. Wegner, D. S. Woodruff, and W. Zajc, Phys. Lett. **B197**, 285 (1987).
- [Abb91] T. Abbott, Y. Akiba, D. Beavis, M. A. Bloomer, P. D. Bond, C. Chasman, Z. Chen, Y. Y. Chu, B. A. Cole, J. B. Costales, H. J. Crawford, J. B. Cumming, R. Debbe, J. Engelage, S. Y. Fung, L. Grodzins, S. Gushue, H. Hamagaki, O. Hansen, R. S. Hayano, S. Hayashi, S. Homma, H. Z. Huang, Y. Ikeda, I. Juricic, J. Kang, S. Katcoff, S. Kaufman, K. Kimura, K. Kitamura, K. Kurita, R. J. Ledoux, M. J. Levine, Y. Miake, R. J. Morse, B. Moskowitz, S. Nagamiya, J. Olness, C. G. Parsons, L. P. Remsberg, H. Sakurai, M. Sarabura, A. Shor, P. Stankus, S. G. Steadman, G. S. F. Stephens, T. Sugitate, M. Tanaka, M. J. Tannenbaum, M. Torikoshi, J. H. Van Dijk, F. Videbaek, M. Vient, P. Vincent, V. Vutsadakis, H. E. Wegner, D. S. Woodruff, Y. D. Wu, and W. Zajc, (E802 collaboration), Phys. Rev. Lett. **66**, 1567 (1991).
- [Ame91] N.S. Amelin, E. F. Staubo, L. P. Csernai, V. D. Toneev, and K. K. Gudima, Phys. Rev. **C44**, 1541 (1991).
- [Bar88] H.W. Barz, B.L. Friman, J. Knoll, and H. Schulz, Nucl. Phys. **A484**, 661 (1988).
- [Bau86] W. Bauer, G. F. Bertsch, W. Cassing, and U. Mosel, Phys. Rev. **C34**, 2127 (1986).
- [Bau87] W. Bauer, Nucl. Phys. A **471**, 604 (1986).

- [Bau88] W. Bauer, Phys. Rev. Lett. **61**, 2543 (1988).
- [Bau92] W. Bauer, C. K. Gelbke, and S. Pratt, Annu. Rev. Nucl. Part. Sci. **42**, 77 (1992), and references therein.
- [Bau92a] W. Bauer, Nucl. Phys. **A545**, 369c (1992).
- [Bau93] W. Bauer, Prog. Part. Nucl. Phys. **30**, 45 (1993).
- [Ber87] V. Bernard, U. G. Meissner and I. Zahed, Phys. Rev. Lett. **59**, 966 (1987).
- [Ber84] G.F. Bertsch, H. Kruse and S. Das Gupta, Phys. Rev. **C29**, 673 (1984).
- [Ber88] G.F. Bertsch, S. Das Gupta, Phys. Rep. **160**, 189 (1988).
- [Ber89] G.F. Bertsch, Comments Nucl. Part. Phys. **19**, 91 (1991).
- [Boh36] N. Bohr, Nature **137**, 344 (1936).
- [Bon82] J. P. Bondorf, Nucl. Phys. **A387**, 25c (1982).
- [Bon85] J. P. Bondorf, R. Donangelo, I. N. Mishustin, C. J. Pethick, H. Schulz, and K. Sneppen, Nucl. Phys. **A443**, 321 (1985).
- [Bow91] D. R. Bowman, G. F. Peaslee, R. T. de Souza, N. Carlin, C. K. Gelbke, W. G. Gong, Y. D. Kim, M. A. Lisa, W. G. Lynch, L. Phair, M. B. Tsang, C. Williams, N. Colonna, K. Hanold, M. A. McMahan, G. J. Wozniak, L. G. Moretto and W. A. Friedman, Phys. Rev. Lett. **67** 1527 (1991).
- [Bow92] D. R. Bowman, C. M. Mader, G. F. Peaslee, W. Bauer, N. Carlin, R. T. de Souza, C. K. Gelbke, W. G. Gong, Y. D. Kim, M. A. Lisa, W. G. Lynch, L. Phair, M. B. Tsang, C. Williams, N. Colonna, K. Hanold, M. A. McMahan, G. J. Wozniak, L. G. Moretto and W. A. Friedman, Phys. Rev. **C46**, 1834 (1992).
- [Bro91] G. E. Brown, C. M. Ko, Z. G. Wu, and L. H. Xia, Phys. Rev. **C43**, 1881 (1991).
- [Bra88] P. Braun-Munzinger, B. Basselleck, W. Cleland, G. David, A. Farooq, M. Fatyga, A. Gavron, V. Greene, J. Hall, R. Heifetz, M. Herman, H. Kent, D. Kraus, D. Lissauer, W. Llope, T. Ludlum, Z. Moroz, E. O'Brian, L. Olsen, D. Sarantites, T. Semkow, B. Shivakumar, J. E. Simon, J. Stachel, H. takai, T. Throwe, L. Waters, J. Wojtkowska, K. Wolf, and D. Wolfe, Z. Phys. C **38**, 45 (1988).
- [Bre60] G. Breit, M. H. Hull, K. E. Lassila and K. D. Pyatt, Rev. Mod. Phys. **34**, 776 (1960).
- [Cha91] G. Chanfray, Z. Aouissat, P. Schuck, and W. Norenberg, Phys. Lett. **B256**, 325 (1991).
- [Cha90] W.Q. Chao, C.S. Gao, and Y.L. Zhu, Nucl. Phys. **A514**, 734 (1990).

- [Cha91] S. Chapman and M. Gyulassy, LBL-30644 (1991) preprint.
- [Cha88] R. J. Charity, M. A. McMahan, G. J. Wozniak, R. J. McDonald, L. G. Moretto, D. G. Sarantites, L. G. Sobotka, G. Guarino, A. Pantaleo, L. Fiore, A. Gobbi, and K. Hildebrand, Nucl. Phys. **A483**, 371 (1988).
- [Cle90] J. Cleymans, H. Satz, E. Suhonen and D. W. von Oertzen, Phys. Lett. **B242**, 111 (1990).
- [Cos90] J. B. Costales, for the E802 Collaboration, Proceedings of the Workshop on Heavy Ion Physics at the AGS, edited by O. Hanson (Brookhaven National Laboratory, Upton, New York, 1990) p. 249.
- [Czi59] P. Cziffra, M. H. MacGregor, M. J. Moravcsik and H. P. Stapp, Phys. Rev. **114**, 880 (1959).
- [Dan81] P. Danielewicz, and J. M. Namyslowski, Acta. Phys. Polon. **B12** 695 (1981).
- [Dan91] P. Danielewicz and G.F. Bertsch, Nucl. Phys. **A533**, 712 (1991).
- [Dau68] J. M. D'Auria, M. J. Fluss, G. Herzog, L. Kowalski, J. M. Miller, and R. C. Reedy, Phys. Rev. **174**, 1409 (1968).
- [Egg91] H.C. Eggers and J. Rafelski, Int. J. Mod. Phys. **A6**, 1067 (1991).
- [Fai82] G. Fai and J. Randrup, Nucl. Phys. **A381**, 557 (1982).
- [Fai83] G. Fai and J. Randrup, Nucl. Phys. **A404**, 551 (1983).
- [Flu69] M. J. Fluss, J. M. Miller, J. M. D'Auria, N. Dudey, B. M. Foreman, jr, L. Kowalski, and R. C. Reedy, Phys. Rev. **187**, 1449 (1969).
- [Fri83] W. A. Friedman and W. G. Lynch, Phys. Rev. **C28**, 16 (1983).
- [Fri83a] W. A. Friedman and W. G. Lynch, Phys. Rev. **C28**, 950 (1983).
- [Fri90] W. A. Friedman, Phys. Rev. **C42**, 667 (1990).
- [Fri89] B. L. Friman, Nucl. Phys. **A498**, 161c (1989).
- [Gel60] M. Gell-Mann, and M. Lévy, Nuovo Cimento **16**, 705 (1960).
- [Gle62] N. K. Glendenning and G. Kramer, Phys. Rev. **126**, 2159 (1962).
- [Gol59] G. Goldhaber, W. B. Fowler, S. Goldhaber, T. F. Hoang, T. E. Kalogeropoulos, and W. M. Powell, Phys. Rev. Lett. **3**, 181 (1959).
- [Gol60] G. Goldhaber, S. Goldhaber, W. Lee, and A. Pais, Phys. Rev. **120**, 300 (1960).
- [Gon91] W.G. Gong, W. Bauer, C. K. Gelbke, and S. Pratt, Phys. Rev. **C43**, 781 (1991)

- [Gon91] W.G. Gong, C. K. Gelbke, W. Bauer, N. Carlin, R. T. de Souza, Y. D. Kim, W. G. Lynch, T. Murakami, G. Poggi, D. P. Sanderson, M. B. Tsang, H. M. Xu, D. E. Fields, K. Kwiatkowski, R. Planeta, V. E. Viola, jr., S. J. Yennello, and S. Pratt, Phys. Rev. **C43**, 1804 (1991).
- [Gos77] J. Gosset, H. H. Gutbrod, W. G. Meyer, A. M. Poskanzer, A. Sandoval, R. Stock and G.D. Westfall, Phys. Rev. **C16**, 629 (1977).
- [Gos78] J. Gosset, J. I. Kapusta, and G.D. Westfall, Phys. Rev. **C18**, 844 (1978).
- [Gre67] A. E. Green and R. Sawada, Nucl. Phys. **B2**, 267 (1967).
- [Gud85] K. K. Gudima and V. D. Toneev, Sov. J. Nucl. Phys. **42**, 409 (1985).
- [Gyu79] M. Gyulassy, S. K. Kauffmann, and L. W. Wilson, Phys. Rev. **C20**, 2267 (1979).
- [Gyu90] M. Gyulassy, Proceedings of the Workshop on Heavy Ion Physics at the AGS, edited by O. Hanson (Brookhaven National Laboratory, Upton, New York, 1990) p. 503.
- [Han54] R. Hanbury Brown and R. Q. Twiss, Phil. Mag. **45**, 663 (1954).
- [Han56a] R. Hanbury Brown and R. Q. Twiss, Nature **177**, 27 (1956).
- [Han56b] R. Hanbury Brown and R. Q. Twiss, Nature **178**, 1046 (1956).
- [Han91] O. Hansen, Comments Nucl. Part. Phys. **20**, 1 (1991).
- [Her92] M. Herrmann, B. L. Friman and W. Norenberg, Z. Phys. **A343**, 119 (1992).
- [Hos61] N. Hoshizaki, I. Lin and S. Machida, Prog. Theor. Phys. **26**, 680 (1961).
- [Iwa56] J. Iwadare, S. Otsuki, R. Tamagaki, and W. Watari, Prog. Theor. Phys. (Kyoto) **15**, 86 (1956).
- [Iwa56a] J. Iwadare, S. Otsuki, R. Tamagaki, and W. Watari, Prog. Theor. Phys. (Kyoto) **16**, 455 (1956).
- [Jaq83] H. Jaqaman, A. Z. Mekjian, and L. Zamick, Phys. Rev. **C27**, 2782 (1983).
- [Kam92] K. H. Kampert, R. Albrecht, T. C. Awes, P. Beckmann, F. Berger, M. Bloomer, C. Blume, D. Bock, R. Bock, G. Claesson, G. Clewing, L. Dragon, A. Eklund, R. L. Ferguson, A. Franz, S. Garpman, R. Glasow, H. Å. Gustafsson, H. H. Gutbrod, G. Hölker, J. Idh, P. Jacobs, B. W. Kolb, H. Löhner, I. Lund, F. E. Obershain, A. Oskarsson, I. Otterlund, T. Peitzmann, F. Plasil, A. M. Poskanzer, M. Purschke, H. G. Ritter, B. Roters, S. Saini, R. Santo, H.R. Schmidt, S. P. Sørensen, K. Steffens, P. Steinhäuser, E. Stenlund, D. Stüken, and G. R. Young (WA-80 collaboration), Institut Für Kernphysik - Universität Münster **IKP-MS-92/1101** (1992).

- [Kap77] J. I. Kapusta, Phys. Rev. **C16**, 1493 (1977).
- [Ko] C. M. Ko, private communication.
- [Ko88] C. M. Ko, and L. H. Xia, Phys. Rev. **C38**, 179 (1988).
- [Ko89] C. M. Ko, and L. H. Xia, Nucl. Phys. **A498**, 561c (1989).
- [Ko90] C. M. Ko, Z. G. Wu, L. H. Xia, and G. E. Brown, Proceedings of the Workshop on Heavy Ion Physics at the AGS, edited by O. Hanson (Brookhaven National Laboratory, Upton, New York, 1990) p. 361.
- [Ko91] C. M. Ko, Z. G. Wu, L. H. Xia, and G. E. Brown, Phys. Rev. Lett. **66**, 2577 (1991).
- [Koc86] P. Koch, B. Müller, and J. Rafelski, Phys. Rep. **142**, 169 (1986).
- [Koo77] S.E. Koonin, Phys. Lett. **B70**, 43 (1977).
- [Kru85] H. Kruse, B. V. Jacak, J. J. Molitoris, G. D. Westfall, and H. Stöcker, Phys. Rev. **C31**, 1770 (1985).
- [Lee88] K. S. Lee, M. J. Rhoades-Brown, and U. Heinz, Phys. Rev. **C37**, 1452 (1988).
- [Li91a] B.A. Li and W. Bauer, Phys. Lett. **B254**, 335 (1991).
- [Li91b] B.A. Li and W. Bauer, Phys. Rev. **C44**, 450 (1991).
- [Li91c] B.A. Li, W. Bauer, and G.F. Bertsch, Phys. Rev. **C44**, 2095 (1991).
- [Li93] B.A. Li, Nucl. Phys. **A552**, 605 (1993).
- [Lis] M. A. Lisa, private communication.
- [Lis93] M.A. Lisa, C. K. Gelbke, W. Bauer, P. Decowski, W. G. Gong, E. Gualtieri, S. Hannuschke, R. Lacey, T. Li, W. G. Lynch, C. M. Mader, G. F. Peaslee, T. Reposeur, A. M. Vander Molen, G. D. Westfall, J. Yee, and S. J. Yennello, Phys. Rev. Lett. **70**, 3709 (1993).
- [Lop84] J. A. Lopez and P. J. Siemens, Nucl. Phys. **A431**, 728 (1984).
- [Mac86] R. Machleidt, Proceedings of Los Alamos Workshop on Relativistic Dynamics and Quark Nuclear Physics (1985 : Los Alamos National Laboratory), John Wiley & Sons., New York (1986) p71.
- [Mat89] R. Mathiello, H. Sorge, H. Stöcker, and W. Greiner, Phys. Rev. Lett. **63**, 1459 (1989).
- [Mat86a] T. Matsui *et al.*, Phys. Rev. **D34**, 783 (1986).
- [Mat86b] T. Matsui, B. Svetitsky, and L. D. McLerran, Phys. Rev. **D34**, 2047 (1986).
- [Mek77] A. Mekjian, Phys. Rev. Lett. **12**, 640 (1977).

- [Mek78] A. Mekjian, Phys. Rev. **C17**, 1051 (1978).
- [Mia90] Y. Miake for the E802 Collaboration, Proceedings of the Workshop on Heavy Ion Physics at the AGS, edited by O. Hanson (Brookhaven National Laboratory, Upton, New York, 1990) p. 240.
- [Mic27] A. A. Michelson, "Studies in Optics," Chap. 11, Univ. Chicago Press, Chicago (1927).
- [Mor75] L. G. Moretto, Nucl. Phys. **A247**, 211 (1975).
- [Mos91] B. Moskowitz, T. Abbott, Y. Akiba, D. Beavis, M. A. Bloomer, P. D. Bond, C. Chasman, Z. Chen, Y. Y. Chu, B. A. Cole, J. B. Costales, H. J. Crawford, J. B. Cumming, R. Debbe, J. Engelage, S. Y. Fung, L. Grodzins, S. Gushue, H. Hamagaki, O. Hansen, R. S. Hayano, S. Hayashi, S. Homma, H. Z. Huang, Y. Ikeda, I. Juricic, J. Kang, S. Kato, S. Kaufman, K. Kimura, K. Kitamura, K. Kurita, R. J. Ledoux, M. J. Levine, Y. Miake, R. J. Morse, S. Nagamiya, J. Olness, C. G. Parsons, L. P. Remsberg, H. Sakurai, M. Sarabura, A. Shor, P. Stankus, S. G. Steadman, G. S. F. Stephens, T. Sugitate, M. Tanaka, M. J. Tannenbaum, M. Torikoshi, J. H. Van Dijk, F. Videbaek, M. Vient, P. Vincent, V. Vutsadakis, H. E. Wegner, D. S. Woodruff, Y. D. Wu, and W. Zajc, (E802 Collaboration), in: Advances in Nuclear Dynamics, edited by W. Bauer and J. Kapusta (World Scientific, Singapore, 1991), p. 295.
- [Mye78] W. D. Myers, Nucl. Phys. **A296**, 177 (1978).
- [Nor28] L. W. Nordheim, Proc. Roy. Soc. (London) **A119**, 689 (1928).
- [PDG74] Particle Data Group, Phys. Lett. **50B**, 74 (1974).
- [PDG76] Particle Data Group, Rev. Mod. Phys. **48**, 514 (1976).
- [Plu92] J. Pluta, *et al.* (DIOGENE collaboration), *submitted* Nucl. Phys. (1992).
- [Pol58] J. C. Polkinghorne, Nuovo Cimento, **8**, 179 (1958).
- [Pol58] J. C. Polkinghorne, Nuovo Cimento, **8**, 781 (1958).
- [Raf82] J. Rafelski and B. Müller, Phys. Rev. Lett. **48**, 1066 (1982).
- [Ran81] J. Randrup and S. E. Koonin, Nucl. Phys. **A356**, 223 (1981).
- [Ree69] R. C. Reedy, M. J. Fluss, G. F. Herzog, L. Kowalski, and J. M. Miller, Phys. Rev. **188**, 1771 (1969).
- [Rop82a] G. Röpke, L. Münchow and H. Schulz, Nucl. Phys. **A379**, 536 (1982).
- [Rop82b] G. Röpke, L. Münchow and H. Schulz, Phys. Lett. **110B**, 21 (1982).

- [Sch92] H.R. Schmidt, R. Albrecht, T. C. Awes, C. Baktash, P. Beckmann, F. Berger, R. Bock, G. Claesson, G. Clewing, L. Dragon, A. Eklund, R. L. Ferguson, A. Franz, S. Garpman, R. Glasow, H. Å. Gustafsson, H. H. Gutbrod, J. Idh, P. Jacobs, K. H. Kampert, B. W. Kolb, P. Kristiansson, I. Y. Lee, H. Löhner, I. Lund, F. E. Obershain, A. Oskarsson, I. Otterlund, T. Peitzmann, S. Persson, F. Plasil, A. M. Poskanzer, M. Purschke, H. G. Ritter, S. Saini, R. Santo, T. Siemiarczuk, S. P. Sorenson, E. Stenlund, M. Tincknell, and G. R. Young (WA-80 collaboration), Nucl. Phys. **A544** 449c (1992).
- [Sch88] P. Schuck, W. Norenberg and G. Chanfray, Z. Phys. **A330**, 119 (1988).
- [Sch57] J. Schwinger, Ann. Phys. **2**, 407 (1957).
- [Sky59] T. H. R. Skyrme, Nucl. Phys. **9**, 615 (1959).
- [Sor89] H. Sorge, H. Stöcker, and W. Greiner, Nucl. Phys. **A498**, 567c (1989).
- [Sta89] J. Stachel, and P. Braun-Munzinger, Nucl. Phys. **A495**, 393c (1989).
- [Sta90] J. Stachel, Proceedings of the Workshop on Heavy Ion Physics at the AGS, edited by O. Hanson (Brookhaven National Laboratory, Upton, New York, 1990) p. 144.
- [Tak51] M. Taketani, S. Nakamura, and M. Sasaki, Prog. Theor. Phys. (Kyoto) **6**, 581 (1951).
- [Tan88] M.S. Tannenbaum, Nucl. Phys. **A488**, 555c (1988).
- [Ueh33] E. A. Uehling and G. E. Uhlenbeck, Phys. Rev. **43**, 552 (1933).
- [Vla38] A. Vlasov, J. Exptl. Theo. Phys. (USSR) **8**, 25 (1938).
- [Vla45] A. Vlasov, J. Phys. (USSR) **9**, 25 (1945).
- [Wan91] S. J. Wang, B. A. Li, W. Bauer, J. Randrup, Ann. Phys. **209**, 251 (1991).
- [Wei37] V. Weisskopf, Phys. Rev. **52**, 295 (1937).
- [Wer89a] K. Werner, Phys. Lett. **B219**, 111 (1989).
- [Wer89b] K. Werner, Z. Phys. **C42**, 567c (1989).
- [Wes76] G.D. Westfall, J. Gosset, P. J. Johansen, A. M. Poskanzer, W. G. Meyer, H. H. Gutbrod, A. Sandoval, and R. Stock, Phys. Rev. Lett. **18**, 1202 (1976).
- [Wol90] Gy. Wolf, G. Batko, W. Cassing, U. Mosel, K. Niita, and M. Schäfer, Nucl. Phys. **A517**, 615 (1990).
- [Won59] D. Y. Wong, Phys. Rev. Lett. **2**, 406 (1959).
- [Won82] C. Y. Wong, Phys. Rev. **C25**, 1460 (1982).

- [Xia89] L. H. Xia, and C. M. Ko, Phys. Lett. **B222**, 343 (1989).
[Zam73] L. Zamick, Phys. Lett. **45B**, 313 (1973).

MICHIGAN STATE UNIV. LIBRARIES



31293008850947